Stony Brook University

Three-Dimensional Macroporous All-Carbon Scaffolds For Tissue Engineering Applications

A Dissertation Presented

by

Gaurav Lalwani

to

The Graduate School

in Partial Fulfillment of the

Requirements

for the Degree of

Doctor of Philosophy

in

Biomedical Engineering

Stony Brook University

May 2015

Stony Brook University

The Graduate School

Gaurav Lalwani

We, the dissertation committee for the above candidate for the

Doctor of Philosophy degree, hereby recommend

acceptance of this dissertation.

Dr. Balaji Sitharaman – Dissertation Advisor
Associate Professor, Department of Biomedical Engineering

Dr. Stefan Judex - Chairperson of Defense
Professor, Department of Biomedical Engineering

Dr. Yi-Xian Qin
Professor, Department of Biomedical Engineering

Dr. Yizhi Meng
Assistant Professor, Chemical and Molecular Engineering Program
Department of Materials Science and Engineering

This dissertation is accepted by the Graduate School

Charles Taber
Dean of the Graduate School

Abstract of the Dissertation

Three-Dimensional Macroporous All-Carbon Scaffolds for Tissue Engineering Applications

by

Gaurav Lalwani

Doctor of Philosophy

in

Biomedical Engineering

Stony Brook University

2015

Assembly of carbon nanomaterials into three-dimensional (3D) architectures is necessary to harness their unique physiochemical properties for tissue engineering and regenerative medicine applications. In this dissertation, fabrication and characterization of 3D chemically crosslinked macro-sized (5-8 mm height and 4-6 mm diameter) porous carbon nanotube (CNT) scaffolds, their *in vitro* cytocompatibility and interactions with human mesenchymal stem cells (hMSCs) are reported. Single- or multi-walled carbon nanotubes (SWCNTs or MWCNTs) scaffolds were fabricated using a novel radical initiated thermal crosslinking and annealing method using SWCNTs or MWCNTs as nanoscale building blocks. The scaffolds possess macroscale interconnected pores, robust structural integrity, stability, and electrical conductivity. Varying the amount of radical initiator can control the porosity of the 3D structure; thereby allowing the design of porous scaffolds tailored towards specific biomedical applications. MC3T3 pre-osteoblast cells and human adipose-derived stem cells (ADSCs) on MWCNT and SWCNT scaffolds (>80% porosity) showed good cell viability comparable to poly(lactic-co-glycolic) acid (PLGA) scaffolds. Confocal live cell and immunofluorescence imaging showed that MC3T3 pre-osteoblasts and ADSCs were metabolically active and could attach, proliferate and infiltrate MWCNT and SWCNT scaffolds. SEM imaging corroborated cell attachment and spreading and suggested that cell morphology is governed by scaffold surface roughness. MC3T3 cells were elongated on scaffolds with high surface roughness (MWCNTs) and rounded on scaffolds with low surface roughness (SWCNTs). The surface roughness of scaffolds may be exploited to control cellular morphology, and in turn govern cell fate. The plasticity of ADSCs was assessed according to International Society for Cellular Therapy guidelines after long term culture (30

days) on CNT scaffolds. The plasticity of ADSCs is maintained after 15 days of culture on 3D SWCNT and MWCNT scaffolds (ADSCs were positive for CD105, CD73 and CD90, and negative for CD45, CD34, CD14 and CD19). ADSCs harvested from 3D MWCNT and SWCNT scaffolds after 30 days show *in-vitro* expansion and tri-lineage differentiation towards osteoblasts, adipocytes and chondrocytes indicating that the scaffolds do not affect differentiation capabilities of the ADSCs. These results show that 3D, macroscopic, porous MWCNT and SWCNT scaffolds with tunable porosities are cytocompatible can be used for the expansion and maintenance of human ADSC and as multifunctional scaffolds for tissue engineering applications.

To my parents, Mr. Pradeep Lalwani and Mrs. Rajkumari Lalwani, for their sacrifices that made this possible.

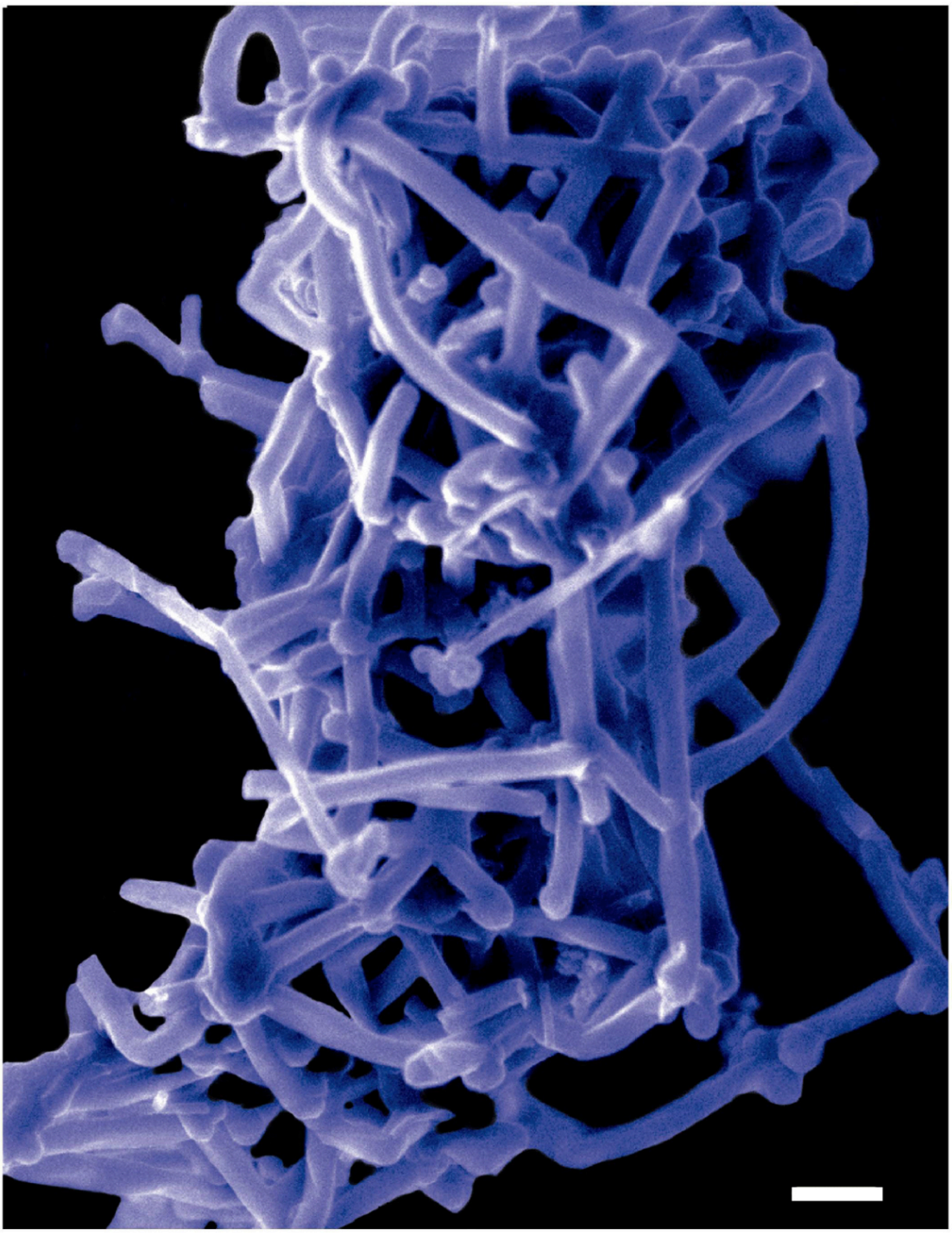

Frontispiece: False colored high-resolution scanning electron microscopy image depicting the formation of nanoscale covalent crosslinks between carbon nanotubes. Scale bar is 500 nm.

Table of Contents

List of Figures

List of Tables

Acknowledgments

The work presented in this dissertation is the culmination of hard work, patience, dedication, and persistence demonstrated over the last few years by brilliant minds that I have had the fortune of being associated with. Likewise, it is an outcome of sacrifices and prayers of my loved ones. I would like to take this opportunity to thank them all.

My foremost debt of gratitude is to Dr. Balaji Sitharaman, my thesis advisor and mentor. Thank you for making me a part of your research group and sharing your passion for carbon nanomaterials. Thank you for the motivation, guidance and positive criticism throughout the years. Your constant support and advice has been invaluable towards shaping my professional and personal development. You inspired independence and taught me that in addition to conceptual scientific clarity, intuition and imagination are important for worthwhile scientific research. I feel privileged to be associated with a mind like yours, the cherry on that rich chocolate cake!

I thank Drs Yi-Xian Qin and Stefan Judex for being a part of my dissertation committee and collaborators on several phases of this project, especially on microCT and nanoindentation studies. Their expert criticism and support during the initial phases of this project has been invaluable. I would also like to thank Dr. Yizhi Meng for being a part of my dissertation committee and her expert feedback on cell-scaffold interactions.

A Part of this research on nanoparticle characterization was conducted at the Center for Functional Nanomaterials (CFN), Brookhaven National Laboratory (BNL), New York. I sincerely thank Drs. Kim Kisslinger and Fernando Camino for spending several hours training and helping me with image acquisition on the high-resolution scanning electron microscopy and Dr. Lihua Zhang for teaching me nuances of the craft of high-resolution transmission electron microscopy.

I acknowledge the support of Central Microscopy, Stony Brook University, especially Drs. Susan Van Horn and Guowei Tian for providing training and access to the TEM and confocal microscope, respectively. Thank you Dr. Timothy Glotch (Department of Geosciences, Stony Brook University) for providing access to the confocal Raman spectroscope.

I appreciate the support of Dr. Antonios G. Mikos for collaborating and inviting me to his laboratory at Rice University to learn polymer synthesis and Dr. Kurt Kasper, Dr. Patrick Spicer and Dr. Allan Henslee for being accommodating hosts and making my time at Rice memorable.

The studies reported in this work wouldn’t have been possible without the support of all past and current lab members of the Sitharaman Lab. I thank Dr. Sayan Mullick Chowdhury for being a support during the late-night experiments, Behzad Farshid for helping me out with the nanocomposite project, Sunny Patel for support with the all-carbon scaffolds project and

carrying forward the legacy of nanotube crosslinking with the all-carbon thin films project, Yahfi Talukdar and Jason Rashkow for all the good times during animal surgeries and stimulations in DLAR, Stephen Lee for help with purchases and setting up of the nanoparticle synthesis apparatus. I would also like to thank Shawn Xie and Cassandra Surhland for their helpful feedback during Lab meetings. Shruti Kanakia- you sportingly tolerating our light-hearted antics! Thank you for not losing patience.

Manisha Rao and Jessica Schneller helped with the synthesis of nanoparticles. Undergrads Anu Gopalan and Priyanka Parmar were great help with nanoparticle synthesis and AFM sample preparation and image acquisition. Michael D'Agati, a motivated high school student (Simons Research Fellow) was hands-on with nanoparticle synthesis and scaffold fabrication. Thank you.

My interactions with friends outside the department have been refreshing. Kalyani Kalwit: You have been my family away from home, a constant support, and a companion throughout my stay here at Stony Brook. Your genuine kindness, generosity, patience, affection and positive reinforcement have provided me strength in difficult times. Thank you. Swati Arora: Thank you for all the unconditional encouragement, love and support throughout the years. You have believed in me more than I did in myself. Subham Dasgupta: Thank you for being a friend whom I could count on. Daphne Meza, Ananya Mishra, Shriya Sahu, Sohit Raina, Jugal Raheja, Sagar Anantwar and Vardhaman Lakhani: Thank you for all the good times.

I am forever indebted to my parents, Mr. Pradeep Lalwani and Mrs. Rajkumari Lalwani for all their sacrifices and perennial support that made this work possible. No words can match up to their love and encouragement. Thank you Aayushi for motivating me to strive for more in your own uncanny ways.

I acknowledge the support of Stony Brook University and the Department of Biomedical Engineering for providing an atmosphere conducive to scientific curiosity.

This work was financially supported by the National Institutes of Health (Grant No.: 1DP2OD007394-01). Part of the research work was performed at CFN, BNL, which is supported by the U.S. Department of Energy, Office of Basic Energy Sciences, under Contract No. DE-AC02-98CH10886.

List of Publications

Google Scholar Profile:

http://scholar.google.com/citations?user=Ol8mVPoAAAAJ&hl=en&oi=ao

1. **Gaurav Lalwani**, Andrea Trinward Kwaczala, Shruti Kanakia, Sunny C. Patel, Stefan Judex and Balaji Sitharaman, "Fabrication and Characterization of Three-Dimensional Macroscopic All-Carbon Scaffolds", *Carbon* 53 (0), 90–100, 2013.

2. **Gaurav Lalwani**, Allan M. Henslee, Behzad Farshid, Liangjun Lin, F. Kurtis Kasper, Yi-Xian Qin, Antonios G. Mikos and Balaji Sitharaman, "Two-Dimensional Nanostructure- Reinforced Biodegradable Polymeric Nanocomposites for Bone Tissue Engineering", *Biomacromolecules* 14 (3), 900-909, 2013.

3. **Gaurav Lalwani**, Allan M. Henslee, Behzad Farshid, Priyanka Parmar, Liangjun Lin, Yi-Xian Qin, F. Kurtis Kasper, Antonios G. Mikos and Balaji Sitharaman, "Tungsten Disulfide Nanotubes Reinforced Biodegradable Polymers for Bone Tissue Engineering", *Acta Biomaterialia* 9 (9), 8365-8373, 2013.

4. **Gaurav Lalwani** and Balaji Sitharaman, "Multifunctional Fullerene and Metallofullerene Based Carbon Nanobiomaterials", *NanoLife* 3 (3), 1342003-1-22, 2013.

5. **Gaurav Lalwani**, Joe Livingston Sundararaj, Kenneth Schafer, Terry Button, and Balaji Sitharaman, "Synthesis, Characterization and *In Vitro* Phantom Imaging of a Novel Graphene-Based Multimodal Magnetic Resonance Imaging and X-Ray Computed Tomography Contrast Agent", *Journal of Materials Chemistry B* 2(22), 3519-3530, 2014.

6. **Gaurav Lalwani**, Xin Cai, Liming Nie, Lihong V. Wang and Balaji Sitharaman, "Graphene Nanoparticles as Multimodal Photoacoustic and Thermoacoustic Contrast Agents", *Photoacoustics* 1 (3-4), 62-67, 2013.

7. **Gaurav Lalwani**, WeiLiang Xing and Balaji Sitharaman, “Enzymatic degradation of oxidized and reduced graphene nanoribbons by lignin peroxidase”, *Journal of Materials Chemistry B* 2(37), 6354-6362, 2014.

8. **Gaurav Lalwani**, Sai Pavan GT, Ojas Mahapatra, C. Gopalakrishnan and Kantha D. Arunachalam, “Study of Effects of Tetrodotoxin (TTX) on Mammalian Brain Tissue Using Iron Nanoparticle-TTX Conjugate”, *International Journal of Materials Science* 4 (5), 529-540, 2009.

9. Sayan Mullick Chowdhury, **Gaurav Lalwani**, Kevin Zhang, Jeong Y. Yang, Kayla Neville and Balaji Sitharaman, "Cell Specific Cytotoxicity and Uptake of Graphene Nanoribbons", *Biomaterials* 34(1): 283-293, 2013.

10. Behzad Farshid, **Gaurav Lalwani**, and Balaji Sitharaman, “*In Vitro* Cytocompatibility of One- and Two-Dimensional Nanostructure-Reinforced Biodegradable Polymeric Nanocomposites”, *Journal of Biomedical Materials Research A*, Early View Online, 2014.

11. WeiLiang Xing, **Gaurav Lalwani**, Irene Rusakova, and Balaji Sitharaman, “Degradation of graphene by hydrogen peroxide”, *Particle & Particle Systems Characterization* 31(7), 745-750, 2014.

12. Yahfi Talukdar, Jason Rashkow, **Gaurav Lalwani**, Balaji Sitharaman, “The effects of One and Two Dimensional Carbon Nanostructures on Mesenchymal Stem Cells”, *Biomaterials* 35(18), 4863–4877, 2014.

13. Sai Pavan GT, **Gaurav Lalwani** and Kantha D. Arunachalam, “Synthesis and comparative effect of iron nanoparticles on the antibacterial activity of antibiotics on pathogenic strains of microorganisms”, *International Journal of Materials Science* 4 (5), 541-548, 2009.

14. Shruti Kanakia, Jimmy Toussaint, Sayan Mullick Chowdhury, **Gaurav Lalwani**, Tanuf Tembulkar, Terry Button, Kenneth Shroyer, William Moore, Balaji Sitharaman, “Physicochemical Characterization of A Novel Graphene-Based Magnetic Resonance Imaging Contrast Agent”, *International Journal of Nanomedicine* 8, 2821-2833, 2013.

Book chapters:

1. **Gaurav Lalwani** and Balaji Sitharaman, "Carbon Nanotechnology in Regenerative Medicine", Handbook of Carbon Nanomaterials, Volume 3 - Medicinal and Bio-related Applications, World Scientific Press, 2012, 107-150.

2. **Gaurav Lalwani**, Yahfi Talukdar, Jason Rashkow and Balaji Sitharaman, "Micro and Nano-Technologies to Engineer Bone Regeneration", Handbook of Micro and Nanotechnologies in Engineering Stem cells and Tissues, John Wiley & Sons, Inc., Hoboken, New Jersey., 2012, doi: 10.1002/9781118574775.ch10.

Chapter 1

INTRODUCTION

Preface

Portions of this chapter have been reproduced from:

1. **Gaurav Lalwani** and Balaji Sitharaman, "Carbon Nanotechnology in Regenerative Medicine", Handbook of Carbon Nanomaterials, Volume 3 - Medicinal and Bio-related Applications, World Scientific Press, **2012**, 107-150.

2. **Gaurav Lalwani** and Balaji Sitharaman, "Multifunctional Fullerene and Metallofullerene Based Carbon Nanobiomaterials", ***NanoLife*** 3 (3), 1342003-1-22, **2013**.

1.1 Regenerative Medicine and Tissue Engineering

According to National Institutes of Health - "*Regenerative Medicine is the process of creating living, functional tissues to repair or replace tissue or organ functionality lost due to age, disease, or congenital defects. It holds the promise of regenerating damaged tissues and organs in the body by stimulating previously irreparable organs to heal themselves using various tissue engineering strategies, smart biomaterials and growing tissues and organs outside the body for surgical implantation"* [1]. Regenerative Medicine involves regeneration, and repair of tissues and organs to restore normal physiological function [2]. Significant advances in the area of regenerative medicine have the potential to address shortage of organs, and save lives through artificial organ transplantation. Although 500,000 Americans benefit from an allogeneic organ transplant every year, there is a significant gap between the number of patients waiting for an organ transplant, and the number of donor organs. According to UNOS (United Network for Organ Sharing), as of September 2011, 112,262 patients are on waitlist for donor organs in the United States [3]. Donor shortages worsen every year and increasing number of patients die on waitlist for required organs. This acute shortage of organs can be addressed by a variety of tissue engineering strategies focusing on the repair and replacement of the non-functional organ.

Tissue Engineering, considered as a sub discipline of regenerative medicine, has been defined as the branch of science which follows the principles of biology and engineering to develop functional substitutes for damaged tissues [4]. It involves the use of various

cell types, engineering methods, and biochemical and physio-chemical factors to promote cell growth in the damaged tissue to restore normal function or replace the biological tissue. The term "tissue engineering" appeared in a 1984 article by Wolter and Meyer in the *Transactions of the American Ophthalmological Society* [5]. It was officially coined in 1988 at a meeting of the US National Science Foundation as *"the application of the principles and methods of engineering and the life sciences towards the fundamental understanding of structure/function relationships in normal and pathological mammalian tissues and the development of biological substitutes to restore, maintain or improve functions"* [6]. With a better understanding of the process of tissue development and wound healing in the past decade, tissue engineering has grown in scope and importance and tissue-engineered products are becoming a reality. The first human tissue engineered product was an artificial skin called Integra™ approved by FDA on March 1, 1996 [7].

1.2 Nanotechnology in Tissue Engineering

With the advances in the field of tissue engineering, improved strategies for the formulation, assessment and monitoring of engineered tissue and biomaterials have been devised. Development of nanotechnology-based tissue engineering approaches have played a significant role in the progress of tissue engineering, and regenerative medicine in the last decade; especially in the design of superior scaffolds, delivery of drugs and transfecting agents, improvements in cellular adhesion, proliferation and differentiation along with imaging and tracking of cells for tissue regeneration [8-18]. Nanotechnology is the study of materials generally in the size range of 1-100 nm with distinctive

nanoscale properties. Nanomaterials are used in various fields of regenerative medicine such as tissue engineering, cell therapy, diagnosis and drug and gene delivery. They can be fabricated from metals, polymers, ceramics, and organic materials and composites using various top-down and bottom-up approaches such as chemical vapor deposition, electrospinning, chemical etching, phase separation, nano-imprinting, self assembly processes, photolithography, thin film deposition and electron beam lithography [19-24]. Nanomaterials can be synthesized in varied morphologies such as tubes, particles, clusters, fibers, rods, wires, films, horns, ribbons, platelets etc. that can simulate the dimensions of various proteins and fibers such as collagen [25-27]. Owing to their small size, large surface area, increased surface roughness and a large surface area to volume ratio; several strategies of surface modifications and functionalization have been formulated which dramatically improve the physicochemical properties of nanomaterials [28-30]. Therefore, nanomaterials have been extensively investigated in a wide range of biomedical applications particularly in regenerative medicine. Branched PA/PGA nanocomposites produced by electrospinning promote the growth of smooth muscle and urothelial cells. These nanocomposites possess increased surface energy, selective protein absorption capabilities and nanotopography similar to the native tissue promoting their use in bladder tissue engineering [31]. Nanostructured titanium (Ti) has been reported to increase vascular cell adhesion and proliferation. Increased elastin and collagen synthesis and competitive endothelial cell adhesion in smooth muscle cells were observed after 5 days in culture [32]. In another study, stem cells grown on vertically aligned titanium di-oxide (TiO_2) nanotubes, in the absence of osteogenic inducing media, differentiated into osteoblasts solely by the virtue of nanotopography [18].

1.3 Carbon Nanomaterials in Tissue Engineering

Carbon nanomaterials are the most widely researched class of materials for applications in materials and biological sciences [33]. They show remarkable physicochemical properties, and functionalization capabilities that can be harnessed for the next-generation biomedical applications [10, 17, 34]. For example, carbon nanotubes possess a Young's modulus of ~ 1 TPa (~ 5 time greater than steel), and are highly conductive with current densities ~ 6×10^7 A cm^{-2} (~ 100 times greater than metallic conductors such as copper) [35-37]. Carbon nanomaterials are of various types such as fullerenes, carbon nanotubes and graphene. Fullerenes are hollow spheres (zero-dimensional), carbon nanotubes are tubular (one-dimensional), and graphene is planar (two-dimensional) sheets of sp^2-bonded carbon atoms arranged in a honeycomb lattice formation (Figure 1A).

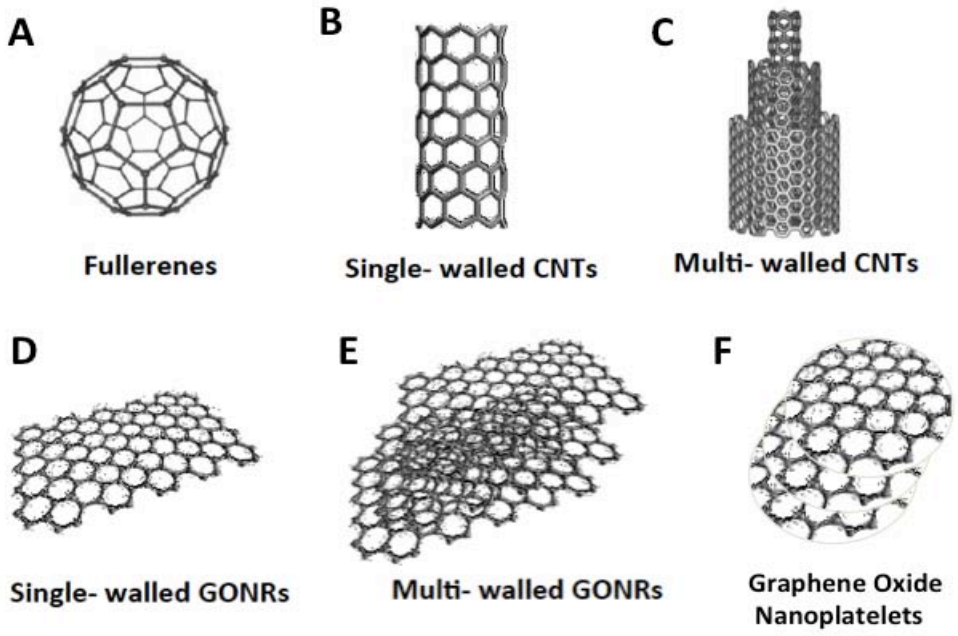

Figure 1: Schematic depiction of carbon nanomaterials (A) Fullerenes, (B) Single-walled carbon nanotubes, (C) Multi-walled carbon nanotubes, (D) Single-walled graphene oxide nanoribbons, (E) Multi-walled graphene oxide nanoribbons and (F) graphene oxide nanoplatelets.

Metallofullerenes are molecules containing one or more trapped metal atoms inside the fullerene cage. Carbon nanotubes are further classified depending upon the number of concentric cylindrical walls, most important of which explored for biomedical applications are single-walled carbon nanotubes (SWCNTs, Figure 1B) and multi-walled carbon nanotubes (MWCNTs, Figure 1C). Recently, Kosynkin, Tour, and co-workers have pioneered an oxidative method that allows the synthesis of graphene nanoparticles in macroscopic amounts by the longitudinal unzipping of carbon nanotubes [25]. These nanoparticles referred to as graphene oxide nanoribbons (GONRs) can be synthesized as single- or multi-walled graphene oxide nanoribbons (SWGONRs and MWGONRs (Figure 1D & E) by unzipping single- and multi-walled carbon nanotubes respectively. Small stacks of graphene sheets referred to as graphene oxide nanoplatelets (GONPs, Figure 1F) can also be synthesized from micrographite particles by Hummer's method of oxidation.

Carbon nanomaterials have been investigated for several biomedical applications such as reinforcing agents to improve the mechanical properties of polymeric nanocomposites and scaffolds [38], contrast agents for magnetic resonance imaging [39, 40], X-ray computed tomography [41-43], photoacoustic imaging [44], drug and gene delivery agents [30, 45, 46], and photodynamic therapy agents for tumor ablation [47-49]. Materials like carbon nanotubes (CNTs) have been extensively used as cell tracking and labeling agents for bioimaging [50], free radical scavenging neuroprotective agents [51], and as reinforcing agents towards the fabrication of biodegradable polymer nanocomposites for bone tissue engineering [14, 38]. Recently, carbon nanotube

substrates have shown enhancement of neuronal cell growth and have been used to guide axonal regeneration and improve neuronal activity at injury site [52]. Carbon nanofibers (CNFs) have similar properties as CNTs and have been extensively used in bone and neuronal tissue engineering. Vertically aligned carbon nanofibers (VACNFs) coated with polypyrrole films are being used as electrodes for deep brain stimulation to treat patients with Parkinson's disease, epilepsy and mental illness [53]. Nanofibers woven by electrospinning are permeable to oxygen and water and have applications in wound healing and skin tissue regeneration [54]. Functionalized CNTs and CNFs have been extensively studied for optical labeling of cells, as drug and gene delivery agents, MRI contrast agents and for a variety of other biomedical applications [29, 30, 55, 56]. There are now multiple reviews that document advances in the functionalization of carbon nanomaterials such as fullerenes, metallofullerenes, carbon nanotubes and graphene for biomedical applications [33, 50, 57-59].

1. 4 Carbon nanotubes (CNTs)

1.4.1 Background

Endo synthesized CNTs in 1976 using a vapor growth technique [60], however, in 1991, it was Iijima's report that brought awareness in the scientific community about the existence of CNTs [61]. Iijima reported the synthesis of needle-like carbon nanotubules during evaporation of carbon using arc discharge and schematically described them as concentric rolled-up graphene sheets. However, in 1992, Ajayan and Ebbesen optimized

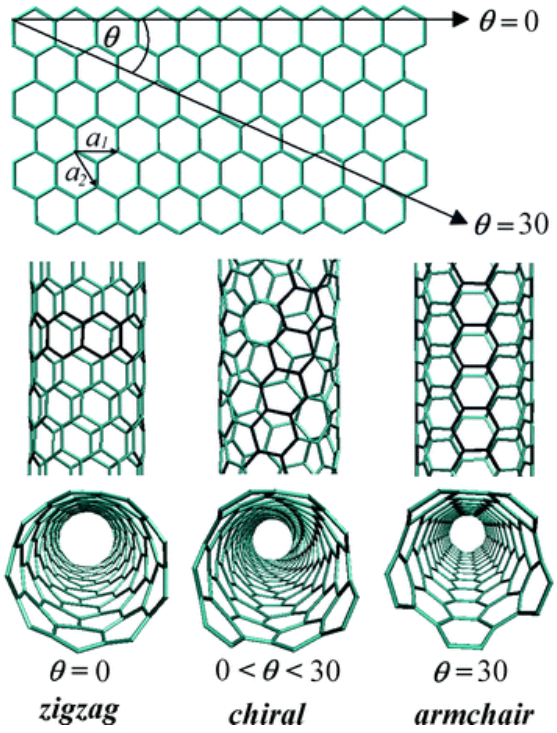

Figure 2: Definition of the chiral vector and various configurations of carbon nanotubes. Zigzag: Θ=0 (*n*, *0*), armchair: Θ=30 (*n*, *n*), and chiral: 0<Θ<30 (*n*, *m*). Adapted from Reference 52 with permission. Copyright © Royal Society of Chemistry, 2010.

and scaled-up the synthesis of CNTs to obtain a yield of 1 gram using a plasma arc-discharge reactor [62].

Based on the orientation of hexagonal lattice with respect to the nanotube axis (Figure 2), the structure of CNT can be denoted by the chiral vector $\vec{C}_h$, given by:

$$\vec{C}_h = n\vec{a}_1 + m\vec{a}_2$$

Where $\vec{a}_1$ and $\vec{a}_2$ are the unit vectors and the integers (n, m) are the number of steps along the bonds of hexagonal lattice. Based on the vector configuration and chirality, CNTs exist in two forms, armchair (n=m) and zigzag (m=0), both possessing mirror symmetry. CNTs that do not exhibit mirror symmetry are chiral. Based on chirality, CNTs can be either metallic or semiconducting.

CNTs can be classified into two main types: (1) single-walled carbon nanotubes (SWCNTs) that consist of a single layer of rolled up graphene sheet and (2) multi-walled carbon nanotubes (MWCNTs) that consist of several layers of graphene sheet rolled up

into concentric cylinders. SWCNTs have diameters between 0.5-3 nm and lengths between 10-5000 nm whereas MWCNTs have diameters between 2-350 nm and lengths between 1-100 μm. The interlayer distance between adjacent walls of MWCNTs is 0.34 nm. The C=C bonds in CNTs have sp^2 hybridization, similar to the bonding in graphite. However, due to the circular curvature in CNTs, a quantum confinement in induced resulting in s-p rehybridization. This leads to the out-of-plane localization of the 's' bonds; hence, the p orbital is delocalized outside the tube architecture [63]. This rehybridization along with the delocalization of p electron confinement results in the unique physiochemical properties of CNTs such as high mechanical properties, electrical and thermal conductivity and chemical and biological activity.

CNTs are not pristine structures; they contain several structural defects formed during their synthesis. One of the most frequently encountered defect is called 'Stone-Wales defect' (Figure 3) wherein the presence of two pairs of five and seven membered carbon rings lead a local deformation in the CNT curvature. Dresselhaus et. al. report that cycloaddition reactions (one of the most commonly used approach for CNT functionalization for biomedical applications) are favored at the C=C in these defect sites [64].

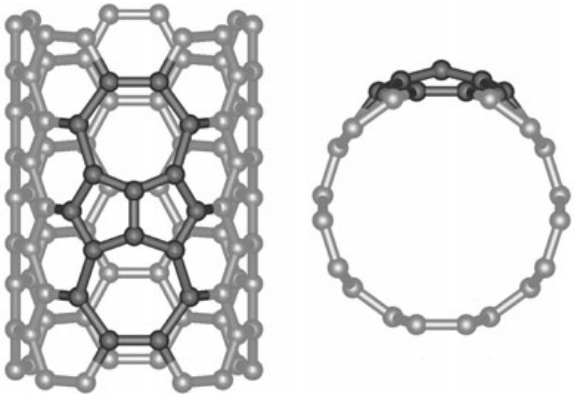

Figure 3: Stone-Wales defect in carbon nanotubes. Adapted from Reference 61 with permission. Copyright © John Wiley and Sons, 2005

1.4.2 Synthesis of Carbon Nanotubes

There exist several established methods for the large-scale industrial production of CNTs. A brief description of commonly used techniques is given below:

1.4.2.1 Arc Discharge

Arc discharge (Figure 4a) was one of the first methods used for the synthesis of CNTs. Iijima used it for the first-ever controlled synthesis of CNTs in 1991 [61]. An arc discharge is generated between two graphite electrodes placed in an airtight chamber with inert atmosphere under the application of DC current [65]. A partial pressure of helium or argon (~ 600 mbar) is applied under voltage (~20V). This results in an electrical discharge elevating the temperature to ~2000-6000°C. At such high temperatures, the carbon atoms of the graphite electrode (anode) undergo sublimation (transformation of solids to gases without conversion into liquids). The high energies involved during sublimation lead to the ejection of a single carbon atom resulting in the formation of plasma. These high-energy atoms move towards the colder graphite electrode (cathode) resulting in the deposition of CNTs on the electrode surface. This method typically results in the formation of MWCNTs, however, if catalysts such as Ni, Co, and Fe are added, SWCNTs can also be produced [66]. The arc discharge method produces high quality MWCNTs. Due to the use of catalysts in the production of SWCNTs; a subsequent filteration step is necessary to remove the metallic impurities along with other

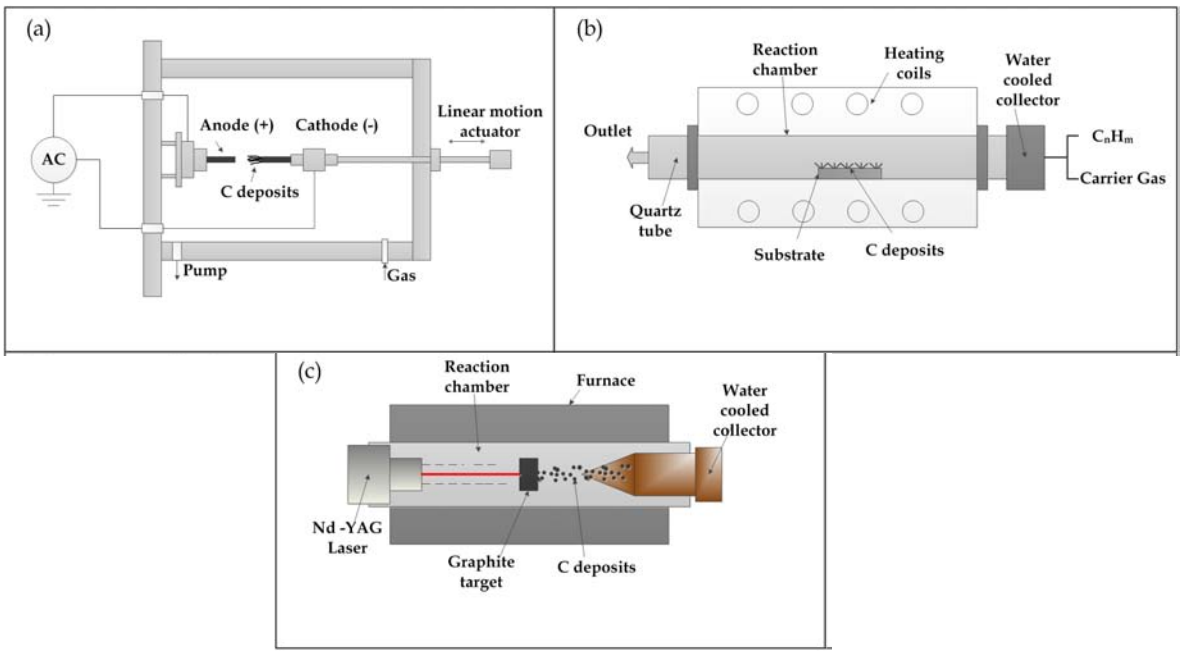

Figure 4: Synthesis of carbon nanotubes using (a) Arc-discharge method, (b) Chemical vapor deposition and (c) Laser ablation. Adapted from Reference 67 with permission. Copyright © Jose-Yacaman et. al., 2011.

contaminants such as soot, amorphous carbon, fullerenes and graphite particles. This method results in the production of highly crystalline CNTs with diameters between 2-30 nm and lengths ~100 μm for MWCNTs and diameters of 1-2 nm and lengths upto ~ 30 μm for SWCNTs [62, 63].

1.4.2.2 Chemical Vapor Deposition (CVD)

CVD (Figure 4b) is the most popular method for the synthesis of CNTs introduced by in 1992 [67]. In this method, the catalytic growth of CNTs is achieved by the decomposition of hydrocarbons. CVD requires substrates that are capable to withstanding high temperatures such as SiO_2, zeolites, alumina and $CoSi_2$ patterned with metal catalysts such as Fe, Ni, Co, Gd or Eu using acetylene, methane, propylene, ethylene, and benzene as carbon precursors [68-72]. The hydrocarbons undergo decomposition inside a furnace

at high temperatures between 500-800°C. Depending on the control of the feed rate of hydrocarbons, reaction time, diameter of catalyst particles, gaseous atmosphere and temperature, MWCNT with diameters between 10-400 nm and 0.1-50 μm can be synthesized. The yield of CNTs using CVD is typically higher than arc-discharge method [73]. Recently, organometallic precursors such as ferrocene or nickelocene have been used as CVD feedstock since they provide carbon source and catalyst in the same compound. They are generally pyrolysed at high temperatures (~1000-1100°C) resulting in the production of either MWCNTs or SWCNTs depending on the reaction conditions. Other sources of carbon such as ferrocene/benzene or ferrocene/xylene have also been used for CNT synthesis [74, 75]. A variation of the CVD process is called the high-pressure carbon monoxide (HiPCO) process wherein iron pentacarbonyl is used as a precursor for iron nanoparticles (catalysts) that provide a nucleation site for the decomposition of carbon monoxide and the subsequent growth of CNTs [76].

1.4.2.3 Laser Ablation

Laser ablation (Figure 4c) was one of the early methods for the production of SWCNTs [67]. In this process, a high-energy beam of pulsed or continuous laser is focused on a graphite rod containing catalysts (for example Ni or Co) in an inert atmosphere. The vaporized carbon atoms of the graphite rod are collected onto a cooled copper collector resulting in the formation of CNTs. MWCNTs produced using this method have inner diameters between 2-3 nm and lengths between 200-800 μm whereas SWCNTs have diameters between 0.4-1 nm and lengths between 5-20 μm.

1.4.3. Properties of carbon nanotubes

1.4.3.1 Mechanical properties

CNTs exhibit extraordinary mechanical properties due to the presence of σ bonds between the carbon atoms. The Young's modulus of individual SWCNTs is ~ 1.5 x 10^4 Pa, ~ 5 times greater than stainless steel [77]. For comparative purposes, the Young's modulus of carbon fibers is ~800 GPa. The ultimate strength of CNTs is between 10-150 GPa, ~ 10 times greater than steel and other synthetic fibers such as poly(lactic acid), poly(glycolic acid) and titanium [78, 79]. The Young's modulus of CNTs is dependent on nanotube chirality, aggregation state and nanotube diameter. The Young's modulus of MWCNTs is independent on nanotube diameter; however, it depends on the presence of defects on the MWCNT architecture. Hernández et. al. reported that SWCNTs with (10, 0) and (6, 6) chirality exhibit modulus values between ~1.22 TPa, whereas large (20,0) SWNTs show a modulus of ~ 1.26 TPa [80]. Forro et. al. showed that individual CNTs exhibit higher values of Young's modulus (in terapascal range) compared to their bundled counterparts that show values in gigapascal range [81]. CNTs are very flexible and can sustain ~ 15-20% of tensile strain before fracture. Iijima et. al. show that MWCNTs and SWCNTs exhibit reversible bending angles of 110° and 120°, respectively [82]. Due to the extraordinary mechanical properties of CNTs, they have been investigated as reinforcing agents to improve the mechanical properties of polymeric scaffolds and nanocomposites for tissue engineering applications [13, 14, 38].

1.4.3.2 Electrical properties

CNTs are one-dimensional nanostructures that exhibit remarkable electrical properties, governed by their chiral vector wherein CNTs are conductive if integers are $n=m$ (armchair) and $n-m = 3i$ (i= integer). In all other cases, CNTs are semiconducting. The resistivity of SWCNTs (~1.4 nm diameter) was $\sim 10^{-4}$ S/cm (similar to metals such as copper = 59×10^4 S/cm) and the current densities were 10^7 A/cm^2 (for comparison, the current densities of superconductors is $\sim 10^5$ A/cm^2) [83]. Due to the presence of structural defects, CNTs have been reported to behave as transistors. A junction of metallic and semiconducting CNTs behaves as a diode with a signal routing speed of ~10 GHz when used as an interconnect material in semiconducting devices [84].

1.4.3.3 Chemical properties

Due to large surface area and sp^2 bonded C=C hybridization, CNTs are attractive candidates for chemical functionalization to improve dispersibility in biological solvents. Several methods of functionalization have been reported such as defect group functionalization, covalent or sidewall functionalization, non-covalent functionalization wherein the chemical groups may further be exploited as anchors for the attachment of biological species such as proteins or nucleic acids, and endohedral functionalization wherein molecules such as fullerenes can be encapsulated inside CNTs [85-87]. CNTs treated with strong acids such as H_2SO_4 or HNO_3 are functionalized with oxidative functional groups such as –OH, =O or –COOH on the sidewalls or tube ends. The

functional groups can further be exploited as sites for the covalent attachment of chemical species such as fluorine, nitrogen, amines, and small molecules such as rhodamine, proteins and antibodies [85]. Biomedical polymers such as poly(lactic-co-glycolic) (PLGA) acid can also be conjugated with CNTs. Cheng et. al. report the use of PLGA functionalized CNTs for the intracellular delivery of caspase-3 into osteocarcinoma cells [88]. Functionalization of CNTs with antibodies can impart tumor-targeting capabilities wherein the nanotubes can act as tumor specific delivery agents of chemotherapeutic drugs [89-91]. Several reports now show that oxidative functionalization reduces aggregation and mitigates toxicological effects of CNTs [92-94].

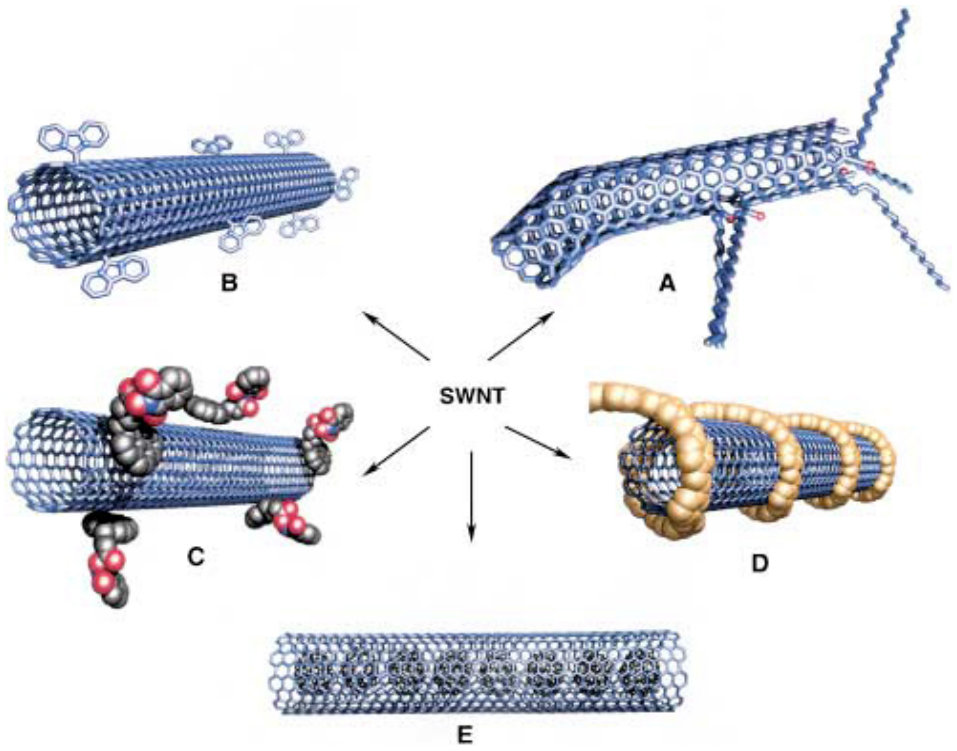

Figure 5: Functionalization of carbon nanotubes. (A) Defect group functionalization, (B) Covalent sidewall functionalization, (C) Non-covalent functionalization with surfactants, (D) Functionalization with polymers, and (E) Endohedral functionalization with fullerenes (C60). Adapted from Reference 89 with permission. Copyright © John Wiley and Sons, 2002.

1.5 Carbon nanotubes as substrates for tissue engineering

In addition to their use as reinforcing agents for polymeric scaffolds and nanocomposites, as probes for bioimaging, and as vectors/carriers for drug and gene delivery, CNTs have been extensively investigated as substrates for tissue-engineering applications. Over the last decade, there has been increasing evidence that CNTs matrices can influence cell growth and proliferation. MacDonald et al. reported that CNT-collagen nanocomposites are cytocompatible and support proliferation of smooth muscle cells and Correa-Duarte et. al. demonstrated the successful growth of L929 mouse fibroblasts [95, 96]. Tutak et. al. showed that SWCNT thin films support the attachment and proliferation of osteoblasts, which is dependent on the film surface energy and roughness [97]. Zhao et. al and Akanska et. al. in independent studies show that functionalized CNTs can provide nucleation sites for the crystallization of hydroxyapatite (Figure 6) and support bone mineralization [98, 99].

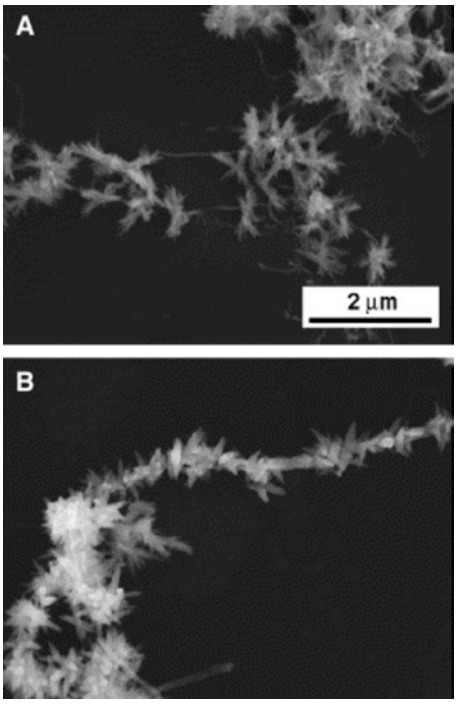

Figure 6: Scanning electron microscopy images of hydroxyapatite crystallization on multiwalled carbon nanotubes. Adapted from Reference 101 with permission. Copyright © Elsevier, 2006.

The functionalization state of CNTs plays an important role in governing cellular proliferation. Zanello et. al. investigated the effect of nanotube functionalization on osteoblast proliferation and bone formation [100]. ROS 17/2.8 osteosarcoma cells were seeded onto 5 differently functionalized

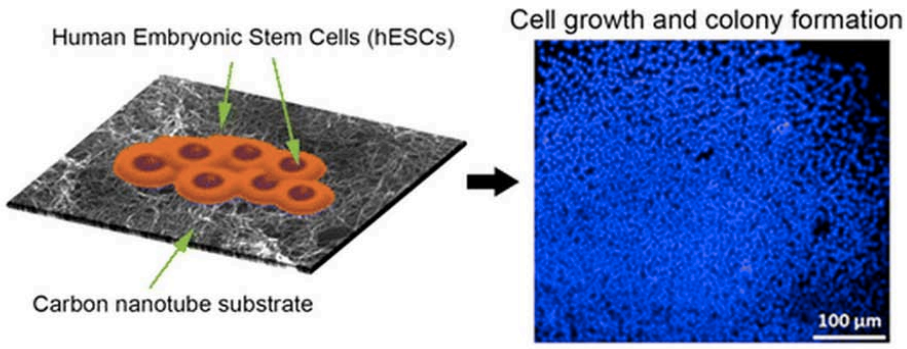

Figure 7: Schematic depiction of human embryonic stem cell culture on carbon nanotube substrate. (B) Fluorescence image showing cell growth and colony formation. Blue fluorescence corresponds to cell nuclei. Adapted from Reference 105 with permission. Copyright © American Chemical Society, 2014.

CNTs. The osteoblast cells show good cell viability and bone extracellular matrix (ECM) deposition on electrically neutral CNTs, which is diminished in the presence of a net charge due to CNT functionalization. Nayak et. al. reported the enhanced proliferation and an accelerated osteogenic differentiation of human mesenchymal stem cells (hMSCs) on PEG-functionalized MWCNTs compared to carboxylated MWCNTs. Bone matrix deposition was observed in the absence of osteogenic inducing media suggesting that functionalization of CNTs can be exploited as a biophysical cue to guide stem cell differentiation into osteoblasts [101]. Nanotopography plays an important role in guiding cellular processes [102]. Recently, Brunner et. al. demonstrated that growth and proliferation of human embryonic stem cells (hESCs) is dependent on surface properties of CNT thin films (Figure 7) [103]. Rough MWCNT films (surface roughness = 467 ± 56 nm) exhibit increased attachment and proliferation of hESCs compared to smooth MWCNT films (surface roughness = 75 ± 15 nm). Coating CNTs with ECM components increases cell viability and reduced CNT toxicity. Pryzhkova et. al. reported successful attachment, proliferation, and maintenance of human pluripotent stem cells (hPSCs) onto ECM coated and hydrophylized CNT arrays [104].

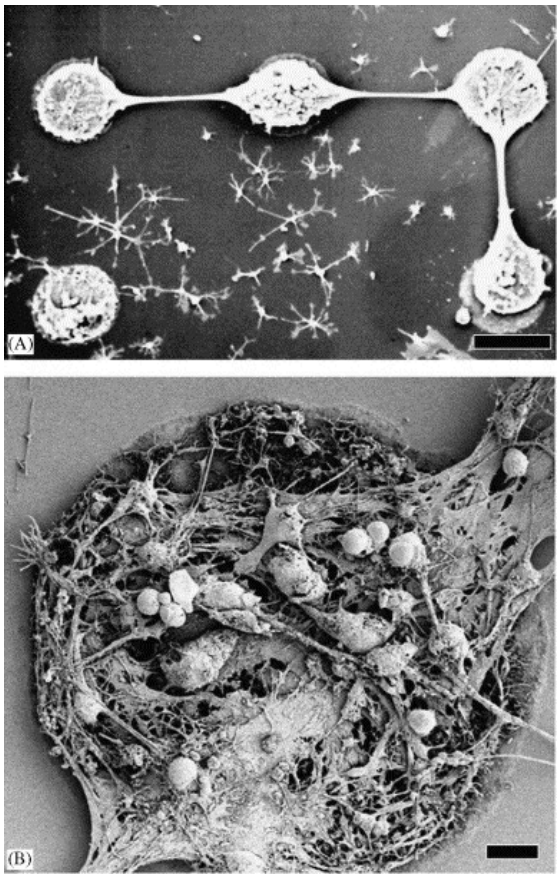

Figure 8: Scanning electron microscopy images of (A) neurons bridging the gap between carbon nanotube islands and forming neural networks. Scale bar represents 100 µm. (B) High magnification image of an individual nanotube island showing neuronal cell attachment and confinement to nanotube island. Scale bar represents 10 µm. Picture courtesy of Y. Hanein—Tel Aviv University, Israel. Adapted from Reference 17 with permission. Copyright © Elsevier, 2007.

CNTs are electrically conductive materials that can be used as interface materials towards the fabrication of neuroprosthetic devices for neuronal tissue engineering applications. Gheith et. al. reported successful electrical stimulation (opening of voltage gated cation channels) and maturation (formation of extended neurites) of neural NG108-15 cells cultured on layer-by-layer (LBL) assembled SWCNT-poly(acrylic acid) thin films [105]. Jan et. al. reported the successful differentiation of mouse embryonic neural stem cells (NSCs) into neurons, astrocytes, and oligodendrocytes on LBL assembled SWCNT-Poly(ethyleneimine) films [106]. Arrays of patterned CNT islands can be used towards the development of neural networks. Gabay et. al. demonstrated the self organization of neuronal cells isolated from rat cortical tissue into compact, ordered wired networks [107]. SEM images (Figure 8) show preferential adhesion of neurons and glia cells onto CNT islands and the formation of neural interfaces between CNT islands by neuronal bridging [17, 107].

Studies till date have focused on the use two-dimensional (2D) CNT substrates (fabricated using vacuum filtration, spray coating or CVD methods) for applications in bone, neuron and cardiac tissue engineering [17, 20, 50, 97, 103, 106]. These methods have several limitations. CVD method requires very specific substrates capable of withstanding high temperatures and pressure. Vacuum filtration and spray coating methods can produce 2D substrates that may not be suitable for tissue engineering of larger organs that demand 3D scaffolds. Recently, 3D porous carbon nanotube and graphene architectures fabricated using CVD and sacrificial template transfer methods have been investigated for tissue engineering applications [96, 108-112]. However, a general limitation of these methods is that in the absence of strong chemical bonds between the individual nanomaterials, the structural integrity of architectures assembled relies mainly on weak Van der Waal forces or on physical entanglement of the nanoparticles, leaving them prone to dissociation under physiological shear forces experienced by in vivo biomedical devices and implants. Furthermore, methods such as sacrificial template transfer do not allow control over the porosity of the assembled 3D scaffold, which depends on the template architecture. Therefore, the assembly of carbon nanomaterials into 3D (especially with >1 mm in all three dimensions) macroporous tissue engineering scaffolds with tunable porosity across various length scales (macro, micro and nanoscopic) would constitute a significant advancement.

1.6 References:

1. (NIH), N.I.o.H., *Fact Sheet - Regenerative Medicine* October 2010.

2. Mason, C. and P. Dunnill, *A brief definition of regenerative medicine.* Regen Med, 2008. **3**(1): p. 1-5.

3. UNOS. *United Network for Organ Sharing*. 2011; Available from: http://www.unos.org.

4. Langer, R. and J.P. Vacanti, *Tissue engineering.* Science, 1993. **260**(5110): p. 920-6.

5. Wolter, J.R. and R.F. Meyer, *Sessile macrophages forming clear endothelium-like membrane on inside of successful keratoprosthesis.* Trans Am Ophthalmol Soc, 1984. **82**: p. 187-202.

6. Chapekar, M.S., *Tissue engineering: Challenges and opportunities.* Journal of Biomedical Materials Research, 2000. **53**(6): p. 617-620.

7. Brockbank, K.G.M., *Tissue Engineering Constructs and Commercialization*, in *Biomaterials in the Design and Reliability of Medical Devices*, B.S.C. Michael N. Helmus, Editor. December 1, 2002, Kluwer Academic Premium Publishers: Austin, TX. p. 226.

8. Zhang, L. and T.J. Webster, *Nanotechnology and nanomaterials: Promises for improved tissue regeneration.* Nano Today, 2009. **4**(1): p. 66-80.

9. Wan, A.C.A. and J.Y. Ying, *Nanomaterials for in situ cell delivery and tissue regeneration.* Advanced Drug Delivery Reviews, 2010. **62**(7-8): p. 731-740.

10. Liao, H., et al., *Applications of carbon nanotubes in biomedical studies.* Methods Mol Biol, 2011. **726**: p. 223-41.

11. Sitharaman, B., et al., *Gadofullerenes as nanoscale magnetic labels for cellular MRI.* Contrast Media Mol Imaging, 2007. **2**(3): p. 139-46.

12. Sitharaman, B. and L.J. Wilson, *Gadonanotubes as new high-performance MRI contrast agents.* Int J Nanomedicine, 2006. **1**(3): p. 291-5.

13. Shi, X., et al., *In vitro cytotoxicity of single-walled carbon nanotube/biodegradable polymer nanocomposites.* J Biomed Mater Res A, 2008. **86**(3): p. 813-23.

14. Sitharaman, B., et al., *In vivo biocompatibility of ultra-short single-walled carbon nanotube/biodegradable polymer nanocomposites for bone tissue engineering.* Bone, 2008. **43**(2): p. 362-70.

15. Sitharaman, B., et al., *A novel nanoparticle-enhanced photoacoustic stimulus for bone tissue engineering.* Tissue Eng Part A, 2011. **17**(13-14): p. 1851-8.

16. Sitharaman, B., et al., *Water-soluble fullerene (C60) derivatives as nonviral gene-delivery vectors.* Mol Pharm, 2008. **5**(4): p. 567-78.

17. Harrison, B.S. and A. Atala, *Carbon nanotube applications for tissue engineering.* Biomaterials, 2007. **28**(2): p. 344-53.

18. Oh, S., et al., *Stem cell fate dictated solely by altered nanotube dimension.* Proc Natl Acad Sci U S A, 2009. **106**(7): p. 2130-5.

19. Vajtai, R., B.Q. Wei, and P.M. Ajayan, *Controlled growth of carbon nanotubes.* Philos Transact A Math Phys Eng Sci, 2004. **362**(1823): p. 2143-60.

20. Dai, H., *Carbon nanotubes: synthesis, integration, and properties.* Acc Chem Res, 2002. **35**(12): p. 1035-44.

21. Heunis, T.D. and L.M. Dicks, *Nanofibers offer alternative ways to the treatment of skin infections.* J Biomed Biotechnol, 2010. **2010**.

22. Yan, C., et al., *Tube Formation in Nanoscale Materials.* Nanoscale Res Lett, 2008. **3**(12): p. 473-480.

23. Thomas, J., et al., *Nanoimprinting by Melt Processing: An Easy Technique to Fabricate Versatile Nanostructures.* Adv Mater, 2011.

24. Adam M. DeRosa, K.G., Saathyaki Rajamani, Balaji Sitharaman *Recent Patents on Single-Walled Carbon Nanotubes for Biomedical Imaging, Drug Delivery and Tissue Regeneration.* Recent Patents on Biomedical Engineering 2010. **3**(4): p. 86-94.

25. Kosynkin, D.V., et al., *Longitudinal unzipping of carbon nanotubes to form graphene nanoribbons.* Nature, 2009. **458**(7240): p. 872-6.

26. Hong, J., et al., *Carbon-based layer-by-layer nanostructures: from films to hollow capsules.* Nanoscale, 2011.

27. Singh, R. and H.S. Nalwa, *Medical applications of nanoparticles in biological imaging, cell labeling, antimicrobial agents, and anticancer nanodrugs.* J Biomed Nanotechnol, 2011. **7**(4): p. 489-503.

28. Subbiah, R., M. Veerapandian, and K.S. Yun, *Nanoparticles: functionalization and multifunctional applications in biomedical sciences.* Curr Med Chem, 2010. **17**(36): p. 4559-77.

29. Liang, F. and B. Chen, *A review on biomedical applications of single-walled carbon nanotubes.* Curr Med Chem, 2010. **17**(1): p. 10-24.

30. Ciofani, G. and V. Raffa, *Chemically functionalized carbon nanotubes: emerging vectors for cell therapy.* Mini Rev Med Chem, 2009. **9**(11): p. 1251-61.

31. Harrington, D.A., et al., *Branched peptide-amphiphiles as self-assembling coatings for tissue engineering scaffolds.* J Biomed Mater Res A, 2006. **78**(1): p. 157-67.

32. Choudhary, S., K.M. Haberstroh, and T.J. Webster, *Enhanced functions of vascular cells on nanostructured Ti for improved stent applications.* Tissue Eng, 2007. **13**(7): p. 1421-30.

33. Lalwani, G. and B. Sitharaman, *Multifunctional Fullerene-and Metallofullerene-Based Nanobiomaterials.* Nano LIFE, 2013. **3**(3): p. 1342003-1-22.

34. Mao, H.Y., et al., *Graphene: promises, facts, opportunities, and challenges in nanomedicine.* Chem Rev, 2013. **113**(5): p. 3407-24.

35. Coleman, J.N., et al., *Small but strong: a review of the mechanical properties of carbon nanotube–polymer composites.* Carbon, 2006. **44**(9): p. 1624-1652.

36. Ebbesen, T., et al., *Electrical conductivity of individual carbon nanotubes.* 1996.

37. Sharakhovsky, L., A. Marotta, and V. Borisyuk, *A theoretical and experimental investigation of copper electrode erosion in electric arc heaters: II. The experimental determination of arc spot parameters.* Journal of Physics D: Applied Physics, 1999. **30**(14): p. 2018.

38. Lalwani, G., et al., *Two-dimensional nanostructure-reinforced biodegradable polymeric nanocomposites for bone tissue engineering.* Biomacromolecules, 2013. **14**(3): p. 900-9.

39. Paratala, B.S., et al., *Physicochemical characterization, and relaxometry studies of micro-graphite oxide, graphene nanoplatelets, and nanoribbons.* PLoS One, 2012. **7**(6): p. e38185.

40. Kanakia, S., et al., *Physicochemical characterization of a novel graphene-based magnetic resonance imaging contrast agent.* International Journal of Nanomedicine, 2013. **8**: p. 2821-2833.

41. Miyamoto, A., et al., *Development of water-soluble metallofullerenes as X-ray contrast media.* Eur Radiol, 2006. **16**(5): p. 1050-3.

42. Wharton, T. and L.J. Wilson, *Highly-iodinated fullerene as a contrast agent for X-ray imaging.* Bioorg Med Chem, 2002. **10**(11): p. 3545-54.

43. Lalwani, G., et al., *Synthesis, Characterization, Phantom Imaging, and Cytotoxicity of A Novel Graphene-Based Multimodal Magnetic Resonance Imaging - X-Ray Computed Tomography Contrast Agent.* J Mater Chem B Mater Biol Med, 2014. **2**(22): p. 3519-3530.

44. de la Zerda, A., et al., *Advanced contrast nanoagents for photoacoustic molecular imaging, cytometry, blood test and photothermal theranostics.* Contrast Media & Molecular Imaging, 2011. **6**(5): p. 346-369.

45. Isobe, H., et al., *Nonviral gene delivery by tetraamino fullerene.* Mol Pharm, 2006. **3**(2): p. 124-34.

46. Bao, H., et al., *Chitosan–Functionalized Graphene Oxide as a Nanocarrier for Drug and Gene Delivery.* Small, 2011. **7**(11): p. 1569-1578.

47. Liu, J., et al., *Preparation of PEG-conjugated fullerene containing Gd3+ ions for photodynamic therapy.* J Control Release, 2007. **117**(1): p. 104-10.

48. Huang, P., et al., *Photosensitizer-loaded dendrimer-modified multi-walled carbon nanotubes for photodynamic therapy.* J Control Release, 2011. **152 Suppl 1**: p. e33-4.

49. Tian, B., et al., *Photothermally enhanced photodynamic therapy delivered by nano-graphene oxide.* ACS Nano, 2011. **5**(9): p. 7000-9.

50. Vardharajula, S., et al., *Functionalized carbon nanotubes: biomedical applications.* Int J Nanomedicine, 2012. **7**: p. 5361-74.

51. Galano, A., *Carbon nanotubes: promising agents against free radicals.* Nanoscale, 2010. **2**(3): p. 373-80.

52. Zhang, X., et al., *Guided neurite growth on patterned carbon nanotubes.* Sensors and Actuators B: Chemical, 2005. **106**(2): p. 843-850.

53. Nguyen-Vu, T.D., et al., *Vertically aligned carbon nanofiber arrays: an advance toward electrical-neural interfaces.* Small, 2006. **2**(1): p. 89-94.

54. Vasita, R. and D.S. Katti, *Nanofibers and their applications in tissue engineering.* Int J Nanomedicine, 2006. **1**(1): p. 15-30.

55. Polizu, S., et al., *Applications of carbon nanotubes-based biomaterials in biomedical nanotechnology.* J Nanosci Nanotechnol, 2006. **6**(7): p. 1883-904.

56. Matson, M.L. and L.J. Wilson, *Nanotechnology and MRI contrast enhancement.* Future Med Chem, 2010. **2**(3): p. 491-502.

57. Sinha, N. and J.T. Yeow, *Carbon nanotubes for biomedical applications.* IEEE Trans Nanobioscience, 2005. **4**(2): p. 180-95.

58. Shen, H., et al., *Biomedical applications of graphene.* Theranostics, 2012. **2**(3): p. 283-94.

59. Balasubramanian, K. and M. Burghard, *Chemically functionalized carbon nanotubes.* Small, 2005. **1**(2): p. 180-92.

60. Koyama, T., M. Endo, and S. Murayama, *Carbon fibers obtained by thermal decomposition of vaporized hydrocarbon.* The 14th Japan Congress on Materials Research, 1971: p. 96-98.

61. Iijima, S., *Helical microtubules of graphitic carbon.* nature, 1991. **354**(6348): p. 56-58.

62. Ebbesen, T. and P. Ajayan, *Large-scale synthesis of carbon nanotubes.* Nature, 1992. **358**(6383): p. 220-222.

63. Meyyappan, M., *Carbon nanotubes: science and applications*. 2004: CRC press.

64. Dresselhaus, M.S., et al., *Defect characterization in graphene and carbon nanotubes using Raman spectroscopy.* Philos Trans A Math Phys Eng Sci, 2010. **368**(1932): p. 5355-77.

65. Gore, J.P. and A. Sane, *Flame Synthesis of Carbon Nanotubes*. Carbon Nanotubes - Synthesis, Characterization, Applications. 2011.

66. Shi, Z., et al., *Large scale synthesis of single-wall carbon nanotubes by arc-discharge method.* Journal of physics and chemistry of solids, 2000. **61**(7): p. 1031-1036.

67. Jose-Yacaman, M., et al., *Catalytic growth of carbon microtubules with fullerene structure.* Applied physics letters, 1993. **62**(2): p. 202-204.

68. Kong, J., et al., *Synthesis of individual single-walled carbon nanotubes on patterned silicon wafers.* Nature, 1998. **395**(6705): p. 878-881.

69. Fonseca, A., et al., *Optimization of catalytic production and purification of buckytubes.* Journal of Molecular Catalysis A: Chemical, 1996. **107**(1): p. 159-168.

70. Qin, L., et al., *Growing carbon nanotubes by microwave plasma-enhanced chemical vapor deposition.* Applied physics letters, 1998. **72**(26): p. 3437-3439.

71. Mao, J., et al., *Growth of carbon nanotubes on cobalt disilicide precipitates by chemical vapor deposition.* Applied physics letters, 1998. **72**(25): p. 3297-3299.

72. Swierczewska, M., I. Rusakova, and B. Sitharaman, *Gadolinium and europium catalyzed growth of single-walled carbon nanotubes.* Carbon, 2009. **47**(13): p. 3139-3142.

73. Cheng, H., et al., *Large-scale and low-cost synthesis of single-walled carbon nanotubes by the catalytic pyrolysis of hydrocarbons.* Applied Physics Letters, 1998. **72**(25): p. 3282-3284.

74. Nxumalo, E.N., V.O. Nyamori, and N.J. Coville, *CVD synthesis of nitrogen doped carbon nanotubes using ferrocene/aniline mixtures.* Journal of Organometallic Chemistry, 2008. **693**(17): p. 2942-2948.

75. Kumar, M. and Y. Ando, *Chemical vapor deposition of carbon nanotubes: a review on growth mechanism and mass production.* Journal of nanoscience and nanotechnology, 2010. **10**(6): p. 3739-3758.

76. Chiang, I., et al., *Purification and characterization of single-wall carbon nanotubes (SWNTs) obtained from the gas-phase decomposition of CO (HiPco process).* The Journal of Physical Chemistry B, 2001. **105**(35): p. 8297-8301.

77. Treacy, M., T. Ebbesen, and J. Gibson, *Exceptionally high Young's modulus observed for individual carbon nanotubes.* 1996.

78. Yu, M.-F., et al., *Tensile loading of ropes of single wall carbon nanotubes and their mechanical properties.* Physical review letters, 2000. **84**(24): p. 5552.

79. Pan, Z., et al., *Tensile tests of ropes of very long aligned multiwall carbon nanotubes.* Applied Physics Letters, 1999. **74**(21): p. 3152-3154.

80. Hernández, E. and A. Rubio, *Nanotubes: Mechanical and Spectroscopic Properties.* Scientific Highlight of the Month, 1999: p. 48-67.

81. Forro, L., et al., *Electronic and Mechanical Properties of Carbon Nanotubes*, in *Science and Application of Nanotubes*, M.F. Thorpe, D. Tománek, and R.J. Enbody, Editors. 2002, Springer US. p. 297-320.

82. Iijima, S., et al., *Structural flexibility of carbon nanotubes.* The Journal of chemical physics, 1996. **104**(5): p. 2089-2092.

83. Thess, A., et al., *Crystalline Ropes of Metallic Carbon Nanotubes.* Science, 1996. **273**(5274): p. 483-7.

84. Javey, A., et al., *Ballistic carbon nanotube field-effect transistors.* Nature, 2003. **424**(6949): p. 654-7.

85. Tasis, D., et al., *Chemistry of carbon nanotubes.* Chemical reviews, 2006. **106**(3): p. 1105-1136.

86. Banerjee, S., T. Hemraj-Benny, and S.S. Wong, *Covalent surface chemistry of single-walled carbon nanotubes.* Advanced Materials, 2005. **17**(1): p. 17-29.

87. Hirsch, A., *Functionalization of single-walled carbon nanotubes.* Angew Chem Int Ed Engl, 2002. **41**(11): p. 1853-9.

88. Cheng, Q., et al., *PLGA-carbon nanotube conjugates for intercellular delivery of caspase-3 into osteosarcoma cells.* PLoS One, 2013. **8**(12): p. e81947.

89. McDevitt, M.R., et al., *Tumor targeting with antibody-functionalized, radiolabeled carbon nanotubes.* J Nucl Med, 2007. **48**(7): p. 1180-9.

90. Wu, W., et al., *Targeted delivery of amphotericin B to cells by using functionalized carbon nanotubes.* Angew Chem Int Ed Engl, 2005. **44**(39): p. 6358-62.

91. Liu, Z., et al., *In vivo biodistribution and highly efficient tumour targeting of carbon nanotubes in mice.* Nat Nanotechnol, 2007. **2**(1): p. 47-52.

92. Firme III, C.P. and P.R. Bandaru, *Toxicity issues in the application of carbon nanotubes to biological systems.* Nanomedicine: Nanotechnology, Biology and Medicine, 2010. **6**(2): p. 245-256.

93. Smart, S., et al., *The biocompatibility of carbon nanotubes.* Carbon, 2006. **44**(6): p. 1034-1047.

94. Dumortier, H., et al., *Functionalized carbon nanotubes are non-cytotoxic and preserve the functionality of primary immune cells.* Nano letters, 2006. **6**(7): p. 1522-1528.

95. MacDonald, R.A., et al., *Collagen-carbon nanotube composite materials as scaffolds in tissue engineering.* J Biomed Mater Res A, 2005. **74**(3): p. 489-96.

96. Correa-Duarte, M.A., et al., *Fabrication and biocompatibility of carbon nanotube-based 3D networks as scaffolds for cell seeding and growth.* Nano Letters, 2004. **4**(11): p. 2233-2236.

97. Tutak, W., M. Chhowalla, and F. Sesti, *The chemical and physical characteristics of single-walled carbon nanotube film impact on osteoblastic cell response.* Nanotechnology, 2010. **21**(31): p. 315102.

98. Zhao, B., et al., *A bone mimic based on the self-assembly of hydroxyapatite on chemically functionalized single-walled carbon nanotubes.* Chemistry of Materials, 2005. **17**(12): p. 3235-3241.

99. Akasaka, T., et al., *Apatite formation on carbon nanotubes.* Materials Science and Engineering: C, 2006. **26**(4): p. 675-678.

100. Zanello, L.P., et al., *Bone cell proliferation on carbon nanotubes.* Nano Lett, 2006. **6**(3): p. 562-7.

101. Nayak, T.R., et al., *Thin films of functionalized multiwalled carbon nanotubes as suitable scaffold materials for stem cells proliferation and bone formation.* ACS Nano, 2010. **4**(12): p. 7717-25.

102. Dalby, M.J., N. Gadegaard, and R.O. Oreffo, *Harnessing nanotopography and integrin-matrix interactions to influence stem cell fate.* Nat Mater, 2014. **13**(6): p. 558-69.

103. Brunner, E.W., et al., *Growth and proliferation of human embryonic stem cells on fully synthetic scaffolds based on carbon nanotubes.* ACS Appl Mater Interfaces, 2014. **6**(4): p. 2598-603.

104. Pryzhkova, M.V., et al., *Carbon nanotube-based substrates for modulation of human pluripotent stem cell fate.* Biomaterials, 2014. **35**(19): p. 5098-109.

105. Gheith, M.K., et al., *Stimulation of Neural Cells by Lateral Currents in Conductive Layer‐by‐Layer Films of Single‐Walled Carbon Nanotubes.* Advanced Materials, 2006. **18**(22): p. 2975-2979.

106. Jan, E. and N.A. Kotov, *Successful differentiation of mouse neural stem cells on layer-by-layer assembled single-walled carbon nanotube composite.* Nano Lett, 2007. **7**(5): p. 1123-8.

107. Gabay, T., et al., *Engineered self-organization of neural networks using carbon nanotube clusters.* Physica A: Statistical Mechanics and its Applications, 2005. **350**(2): p. 611-621.

108. Crowder, S.W., et al., *Three-dimensional graphene foams promote osteogenic differentiation of human mesenchymal stem cells.* Nanoscale, 2013. **5**(10): p. 4171-6.

109. Li, N., et al., *Three-dimensional graphene foam as a biocompatible and conductive scaffold for neural stem cells.* Sci Rep, 2013. **3**: p. 1604.

110. Nardecchia, S., et al., *Modulating the cytocompatibility of tridimensional carbon nanotube-based scaffolds.* Journal of Materials Chemistry B, 2013. **1**(24): p. 3064-3072.

111. Abarrategi, A., et al., *Multiwall carbon nanotube scaffolds for tissue engineering purposes.* Biomaterials, 2008. **29**(1): p. 94-102.

112. Aoki, N., et al., *Carbon nanotubes as scaffolds for cell culture and effect on cellular functions.* Dent Mater J, 2007. **26**(2): p. 178-85.

Chapter 2

FABRICATION AND CHARACTERIZATION OF THREE-DIMENSIONAL MACROACOPIC ALL-CARBON SCAFFOLDS

Preface

Portions of this chapter have been reproduced from:

Gaurav Lalwani, Andrea Trinward Kwaczala, Shruti Kanakia, Sunny C. Patel, Stefan Judex and Balaji Sitharaman, "Fabrication and Characterization of Three-Dimensional Macroscopic All-Carbon Scaffolds", *Carbon* 53 (0), 90–100, 2013.

The authors listed in the above manuscript have contributions towards the data reported in this chapter.

2.1 Introduction

The development of three-dimensional (3-D) all carbon scaffolds (porous structures) could lead to significant advancements in the field of energy storage, electronic devices, high performance catalysts, super capacitors, photovoltaic cells, field emission devices, smart sensors, and biomedical devices and implants [1-6]. 3-D microscopic scaffolds using carbon nanotubes have been successfully assembled by “bottom-up” (e.g. chemical vapor deposition) or “top-down” (e.g. capillary-induced self-assembly) approaches [7-12]. Using these strategies, microscopic 3-D random or patterned structures comprised of either aligned or entangled carbon nanotubes have been synthesized. Macroscopic scale (> 1mm in two or all three dimensions) structures of vertically aligned or entangled networks of pristine CNTs and graphene have also been fabricated [13-22]. However, the suitability of these approaches to control the porosity of the 3-D CNT structures or to form covalent bonds between CNTs, an important feature for many applications[23] still has to be demonstrated. Furthermore, the potential of these techniques to synthesize 3-D macroscale structures using other carbon nanomaterials such as fullerenes and graphene still needs to be investigated. Additionally, these approaches may present a practical challenge to develop macroscopic-scale (> 1mm in all 3 dimensions) carbon devices; either due to scalability issues, or high operational cost.

Towards the goal of fabricating 3-D all-carbon devices with macroscopic dimensions, we report the synthesis, and characterization of macroscopic, structurally-stable 3-D, all-carbon scaffold using MWCNTs. We also demonstrate that this facile method can in

general be applied to fabricate 3-D, all-carbon scaffolds with different architectures (such as cylinders, disk etc.) using other carbon nanomaterials such as fullerenes, single-walled carbon nanotubes, and graphene.

2.2 Materials and methods

2.2.1 Fabrication of 3-D crosslinked carbon scaffolds

Multiwalled carbon nanotubes (Sigma Aldrich, Cat No. 659258), single walled carbon nanotubes (Sigma Aldrich, Cat No. 519308), Fullerenes (Sigma Aldrich, Cat No. 483036), benzoyl peroxide (BP, Luperox®, Sigma Aldrich, Cat No. 179981) and chloroform ($CHCl_3$, Fisher Scientific, Cat No. BPC297) were used as purchased. Graphene nanoplatelets were synthesized and characterized by a literature method, and have been reported elsewhere [24]. The MWCNT scaffolds were fabricated by mixing MWCNT and BP at different mass ratios (BP: MWCNT = 1:0.5, 1:1, 1:2, 1:3 and 1:4). 1 ml $CHCl_3$ was added to the mixture to dissolve, and ensure uniform dispersion of BP (see supplementary information Figure S2 for the dispersion state of MWCNTs). The fullerenes, SWCNT and graphene nanoplatelet scaffolds were prepared by mixing BP with these carbon nanomaterials in the ratio 1:1. The BP-carbon nanomaterial mixture was subjected to bath sonication (30 minutes, Ultrasonicator FS30H, Fischer Scientific, Pittsburgh, PA), poured in custom machined Teflon molds (length = 1.2 mm, diameter = 0.5 mm), and incubated at 60°C for 24 hours. Post incubation, the molds were disassembled to obtain the cross-linked three-dimensional carbon scaffolds. 5 scaffolds

were prepared for each experimental group. As a purification step after crosslinking, scaffolds were placed at 150°C for 20 minutes to remove the excess BP.

2.2.2 Raman Spectroscopy

Raman analysis was performed using a WITec alpha300R Micro-Imaging Raman Spectrometer using a 532 nm Nd-YAG excitation laser. Point spectra were recorded between 50 -3750 cm^{-1} at room temperature.

2.2.3 Thermogravimetric Analysis (TGA)

TGA was performed using a Pyris Perkin Elmer diamond TGA instrument at the Center for Functional Nanomaterials (CFN), Brookhaven National Laboratory, New York. Measurements were conducted on samples in alumina pan from 50 to 800 °C with a heating rate of 10 °C/min under an air flow of 100 ml/min.

2.2.4 Nanoindentation

Mechanical properties of purified MWCNT scaffolds were determined using nanoindentation (Triboindenter; Hysitron, Minneapolis, MN) with a Berkovich indenter tip. MWCNT scaffolds were attached to metal disks using cyanocryolate and mounted into the indenter. The points of indentation were selected at a distance no less than 100 μm away from each other. Samples were indented 7 times to determine elastic modulus (Er) and material hardness (H). The tip area function was calibrated from indentation

analysis on fused quartz, and drift rates in the system were measured prior to each indentation using standard indentation testing procedures [25]. First, a preload of 3μN was applied to the system followed by a constant loading rate (10μN/second). Then a hold segment at a fixed system load was applied, followed by a constant unloading rate to retract the tip (-10μN/second), then another hold segment was imposed (3 μN). The sample was indented with peak loads ranging from ≈15 μN to 100 μN [26]. The elastic response was calculated from the 20-90% portion of the unloading curve using methods previously described [27].

2.2.5 Micro-Computed Tomography

Micro-CT analysis was performed to quantify the 3D porosity of MWCNT scaffolds. A Scanco Medical microCT-40 (Scanco Medical AG, Bassersdorf, Switzerland) was used at 45 kV, 177 μA current and 900 ms integration time. A 3D Gaussian filter was applied to the images and a global threshold separated carbon nanotubes from noise [28]. The threshold value was determined by visual comparison between the thresholded and the raw gray-scale image and was optimized to accurately represent the raw images of scaffolds. For a 150 x 150 x 150 voxel cube, total volume (TV), carbon nanotube volume (CNV) and scaffold volume fraction (CNV/TV) were determined. Three voxel cubes per scaffold were analyzed and the average of the three regions and its standard deviation is reported. The regions of analysis were selected in the center of the scaffold to eliminate the edge artifacts. The porosity of the scaffolds was calculated as:

$$Porosity\ (\%) = (1 - scaffold\ volume\ fraction\ [\frac{CNV}{TV}]) * 100$$

2.2.6 Electron Microscopy

Scanning electron microscopy (SEM) was performed using JOEL 7600F Analytical high resolution SEM at the Center for Functional Nanomaterials (CFN), Brookhaven National Laboratory, New York. Crosslinked carbon nanotube specimens were placed on a conductive, double sided, carbon adhesive tab (PELCO, Ted Pella), and imaged at 1 and 5 kV accelerating voltages using a secondary electron imaging (SEI) detector. Transmission electron microscopy (TEM) was performed using FEI BioTwinG^2 TEM at Stony Brook University. The samples were imaged at 80kV using 300 mesh size, holey lacey carbon grids (Ted Pella, Inc.).

2.2.7 Image Processing

Image processing toolbox in MATLAB was used to quantify the porosity values of the crosslinked specimens. SEM images at various magnifications were cropped to remove the legends, and the scale bar, and were subjected to image processing steps such as edge detection, thresholding, median filtration, erosion and dilation followed by quantification of region properties. Porosity was calculated using n=5 images as the ratio of the total area of voids to the total area of the image.

$$Porosity\ (\%) = \left(\sum Area\ of\ voids/area\ of\ the\ image\right) * 100$$

2.2.8 Liquid Extrusion Porosimetry

Liquid extrusion porosimetry (LEP) was performed on purified MWCNT scaffolds using the PMI liquid extrusion porosimeter at Porous Materials Inc., Ithaca, NY. The CNT scaffolds were placed on a membrane and the sample chamber was filled with Galwick® (wetting liquid, surface tension ≈ 0, propene, 1,1,2,3,3,3-hexafluoro, oxidized, polymerized) which penetrates into the pores of the sample. An inert gas under pressure was applied to extrude the liquid from the pores of the MWCNT scaffold. The volume and weight of the extruded liquid was measured, and porosity and median pore diameter were calculated as described previously [29, 30].

2.2.9 Four Point Resistivity Measurements

Bulk resistivity was assessed by a four-probe resistance measurement technique (Signatone S302-4, SP-4 probe) at Center for Functional Nanomaterials (CFN), Brookhaven National Laboratory, New York. Four point resistance measurements assess planar resistances for a theoretically infinitesimal thickness of sample. Thus, bulk material resistance can be derived from sheet resistance with a correction factor (F) to account for the thickness of the sample. The four, spring-loaded probes were equally spaced at 1.25 mm distances, with the two outer probes providing current and inner probes measuring voltage. Sheet resistance values for each MWCNT scaffold was measured at three different regions. Resistivity of the MWCNT scaffold was calculated by:

$$\rho = \mathrm{R}_{\mathrm{sheet}} * w * \frac{\pi}{\ln(2)} F$$

Where ρ is the bulk resistivity, R_{sheet} is the sheet resistance, *w* is the thickness of the sample (0.5 cm), and F is the correction factor. The conductivity was then obtained by calculating the 1/ρ value.

2.2.10 Statistical Analysis

Statistical analysis was performed using a student's "t" test and one-way anova followed by Tukey Kramer post hoc analysis. A 95% confidence interval ($p<0.05$) was used for all statistical analysis.

2.3 Results and discussion

MWCNTs were thermally crosslinked via radical-initiated reaction using benzoyl peroxide. Briefly, a few drops of chloroform were added to the MWCNT-BP mixture (see method section for details), and the slurry was poured into prefabricated PTFE (Teflon®) molds (disk or cylinder molds), and incubated at 60°C for 24 hours. Benzoyl peroxide is a

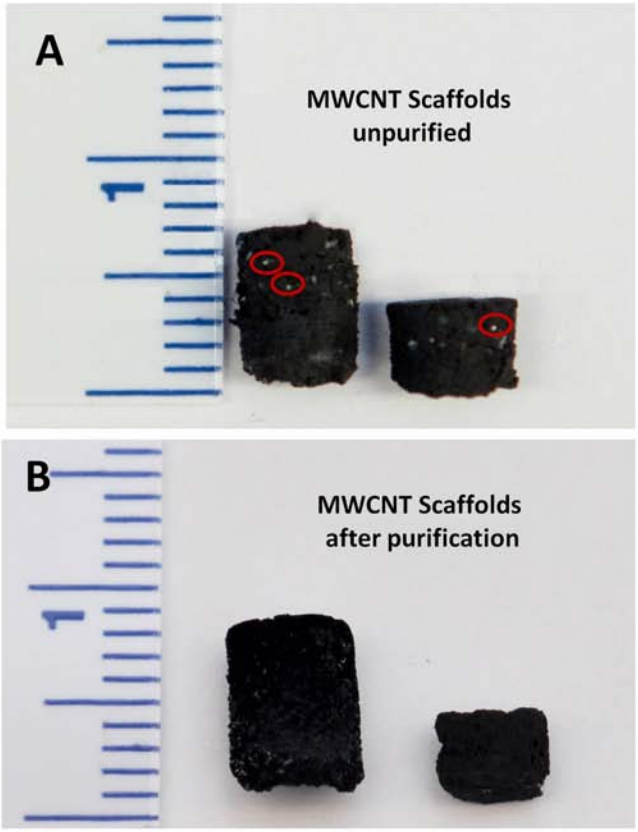

Figure 9: Optical images of representative thermally-crosslinked 3-D, macroscopic (A) unpurified and (B) purified MWCNT scaffolds; prepared as cylinders (5 mm diameter, 7 mm length), and disks (5 mm diameter, 4 mm thickness).

widely used initiator in free radical polymerization reactions [31]. It thermally decomposes to yield phenyl or benzoyloxyl free radicals, and CO_2 gas, and has been used for covalent functionalization of carbon nanotubes [32, 33]. Polymerization of formulations with reactive double bonds initiated by temperature-, or radiation-induced radicals is a widely-used method [34]. In the above reaction, the radicals react with the double bond network on the MWCNT structure; thereby forming active centers, which serve as inter-nanotube cross-linking sites. This results in the nanoscale crosslinking of carbon nanotubes, yielding macroscopic 3-D carbon scaffolds. The un-reacted BP and other volatiles (generated during the termination of radical crosslinking reaction) were removed by annealing the 3-D carbon scaffolds at 150 °C for 20 minutes. Figure 9 displays the digital images of representative unpurified and purified 3-D MWCNT scaffolds prepared by mixing MWCNTs and BP in the mass ratio 1:4. The unpurified scaffolds have a grayish-black tint, due to some residual BP (red circles), and purified scaffolds do not have this tint. The scaffolds are robust free-standing structures, and structurally stable; similar to polymeric scaffolds (see supplementary information S7 movie) [35].

2.3.1 Raman Spectroscopy

The Raman spectra of the pristine MWCNT, the unpurified, and purified MWCNT scaffolds (MWCNT: BP mass ratio = 1:4) are presented in Figure 10A. The pristine MWCNT used as the starting material shows the characteristic D, G, and G' bands at 1355 cm^{-1}, 1580 cm^{-1}, and 2694 cm^{-1} respectively (Figure 10A, blue line). The I_D/I_G ratio for pristine MWCNTs is 0.07, The G band in the Raman spectra has been attribute to the

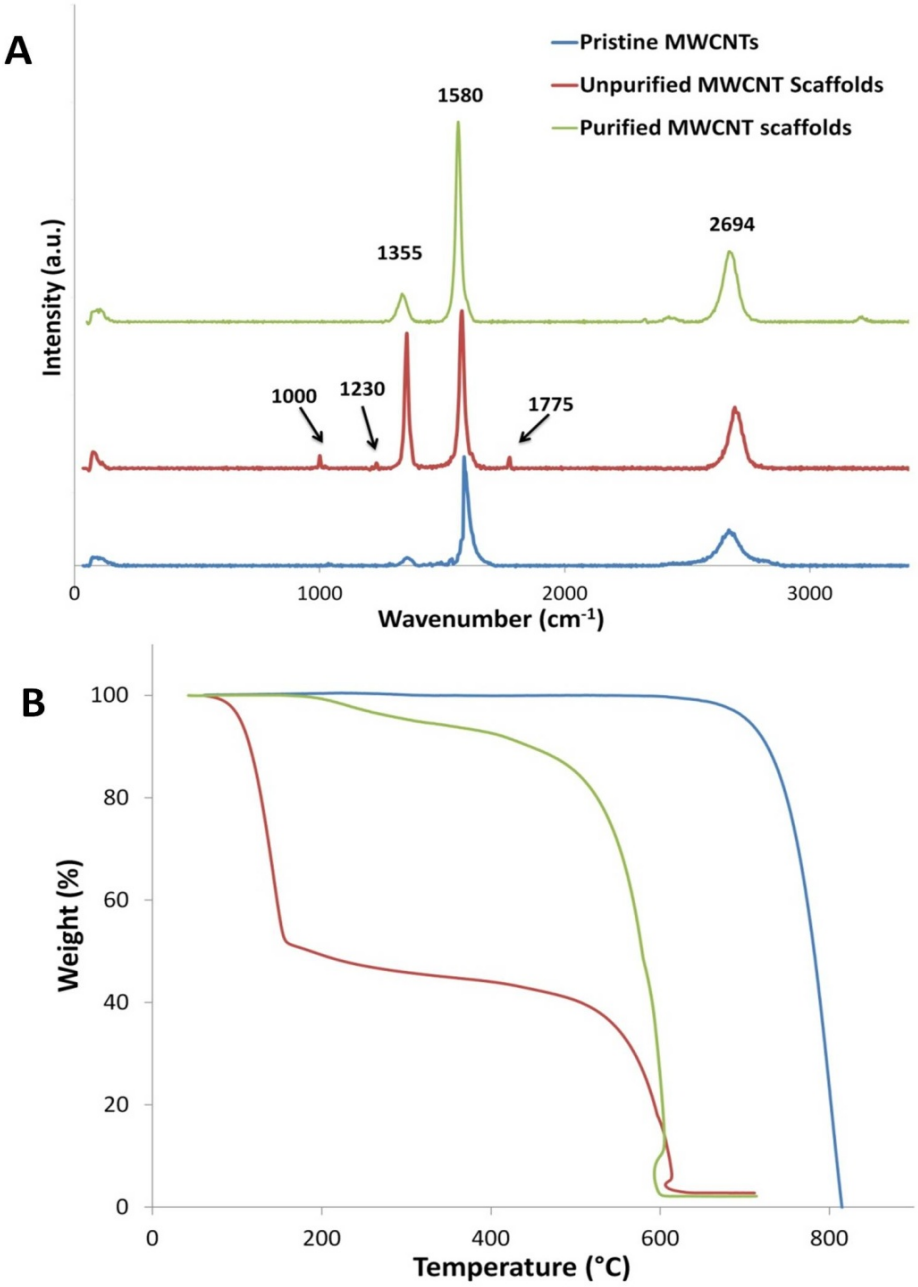

Figure 10: (A) Representative Raman spectra of pristine multiwalled carbon nanotubes (blue trace) and the 3-D crosslinked MWCNT scaffolds (MWCNT: BP mass ratio = 1: 4) before (red trace) and after (green trace) purification. (B) TGA curves of pristine MWCNTs, MWCNT scaffolds before- and after- purification.

intrinsic vibration of sp^2 bonded graphitic carbon atoms, whereas the D band corresponds to the defects induced in the nanotube structure due to disruption of the sp^2 C=C bonds

[36]. The Raman spectrum of the unpurified (Red line), and purified (green line) MWCNT scaffolds (MWCNT: BP mass ratio = 1:4) shows a substantial increase in the intensity of the D band. The I_D/I_G ratio for the unpurified and purified MWCNT scaffolds is 0.85, and 0.14, respectively. The Raman spectrum of the unpurified MWCNT scaffolds also shows additional minor peaks at 1000 cm^{-1}, 1230 cm^{-1} and 1775 cm^{-1}, which can be attributed to the breathing mode (C-C stretching) of benzene ring, C-O bond stretching (vibration of the peroxide chain) and C=O bond stretching (aryl carbonate functional group), respectively [37, 38]. These peaks are routinely observed in the Raman spectra of most radical functionalization reactions with BP [39]. The intensities of these peaks were relatively minor compared to the D and G bands, and were repeatedly observed only in the Raman spectra of unpurified MWCNT scaffolds. The decrease in the I_D/I_G ratio, and the absence of the minor peaks in the Raman spectrum of the purified MWCNTs scaffolds compared to the purified MWCNTs scaffolds suggests that the disruption of the sp^2 (C=C) bonds for the purified MWCNTs scaffolds is due to crosslinked C-C bonds, covalent carbonyl, benzoyloxyl and phenyl functional groups formed during crosslinking reaction [33], and non-covalent π- π interactions between the MWCNTs and the aromatic groups of unreacted BP [40], and benzoyloxyl /phenyl radical by-products. The annealing of the unpurified MWCNT scaffolds removes the unreacted BP, and the reaction by-products which decompose between 100-150 °C. The heating procedure de-adsorbs the unreacted BP and by-products, and partially restores sp^2 (C=C) bonds decreasing the I_D/I_G ratio. However, the I_D/I_G ratio of the purified MWCNT scaffolds is still more than two orders greater than pristine MWCNTs indicating the presence of C-C, C-O and C=O bonds. The above assessment is further corroborated by TGA analysis.

2.3.2 Thermogravimetric Analysis

Thermogravimetric analysis (TGA) has been widely used for the characterization of carbon-based nanomaterials [41-44]. The TGA spectra of the pristine MWCNT, the unpurified and the purified MWCNT scaffolds (MWCNT: BP mass ratio = 1:4) is presented in Figure 10B. The TGA spectra of pristine MWCNTs is similar to previous reports [43], and exhibit negligible weight loss (0.05%) up to 700°C confirming its high thermal stability, and purity. Thermal decomposition of unpurified and purified MWCNT scaffolds can be divided into three temperature zones, 0-150°C, 150-500°C and > 500°C. In first temperature zone between 0-150°C, the %weight loss of unpurified and purified MWCNT scaffolds was 43.06%, and 0.03% respectively. The high %weight loss observed for the unpurified MWCNT scaffolds can be attributed to the removal of residual water vapor, unreacted BP, and other volatiles (possible benzoyloxyl, and phenyl adducts formed during termination of the crosslinking reaction). The purified MWCNT scaffolds show negligible %weight loss indicating the high temperature annealing completely removes the unreacted BP, and other volatile by-products adsorbed on the unpurified MWCNT scaffold. In the second temperature zone between 150-500°C, the %weight loss is similar for the unpurified (16.51%), and the purified MWCNT (15.06%) scaffolds, and corresponds to the removal of functional groups attached to MWCNTs [43]. Finally, above 500°C, the observed %weight loss for the unpurified and purified MWCNT scaffolds corresponds to the thermal degradation of the MWCNT with sp^2 and sp^3 carbon atoms [41-43].

2.3.3 Nanoindentation

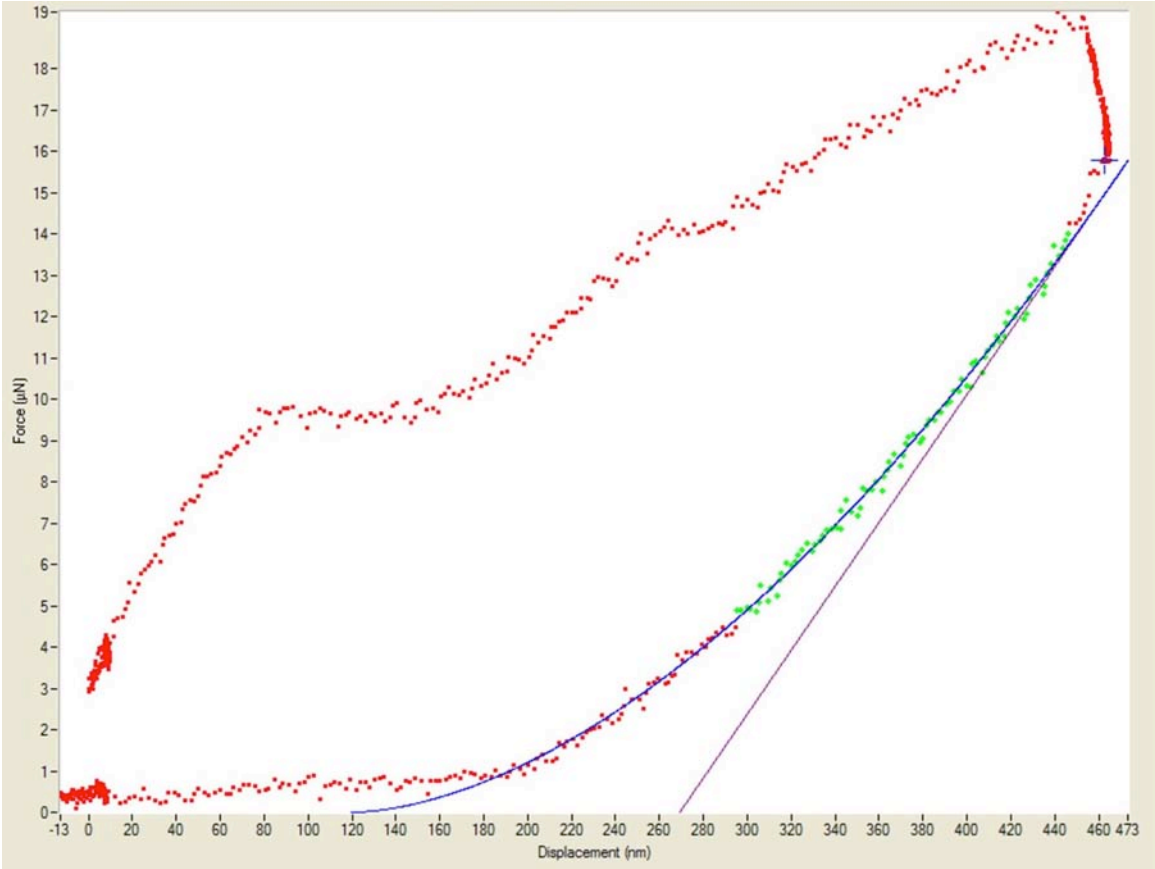

Figure 11: Representative loading-unloading curve during nanoindentation of MWCNT scaffold (MWCNT: BP mass ratio = 1:2). The red dots are raw data and green dots are analyzed data. The slope of the best-fit line (blue) was used to calculate elastic modulus.

Nanoindentation was performed on purified MWCNT scaffolds (MWCNT:BP mass ratio = 1:1 and 1:2). Table 1 summarizes values of elastic modulus (Er) and hardness (H) measured by 7 indents (at least 100μm distance between each indent). Representative force-displacement curve is presented in Figure 11 (MWCNT:BP mass ratio = 1:2). Er and H values of MWCNT scaffold (1:1) were 38.45 ± 14.42 MPa and 1.82 ± 0.54 MPa, respectively. MWCNT scaffold (1:2) exhibited Er of 45.72 ± 18.78 MPa and H of 3.47 ±

1.73 MPa, higher than 1:1 MWCNT:BP scaffold. These elastic modulus values for MWCNT scaffolds are much higher than the values measured for various polymeric, graphene and CNT based foams [15, 21, 45]. For example, the CNT assembly reported by Xu et al. possessed storage modulus of 1 MPa and loss modulus of 0.3 MPa [15]. Young's modulus of 3D graphene assemblies as reported by Zhang et al. was 1.2-6.6 MPa[21], Shi et al. was ≈ 290 kPa[46] and Wang et al. was ≈ 260 kPa [47]. The relatively high values of elastic modulus and hardness of MWCNT scaffolds further corroborates the formation of nanoscale, covalent crosslinks between MWCNTs necessary to achieve the measured mechanical strengths at a macroscopic scale.

2.3.4 X-ray Photoelectron Spectroscopy and Electrical Conductivity

XPS analysis was performed on purified MWCNT scaffold over an elliptical area (major

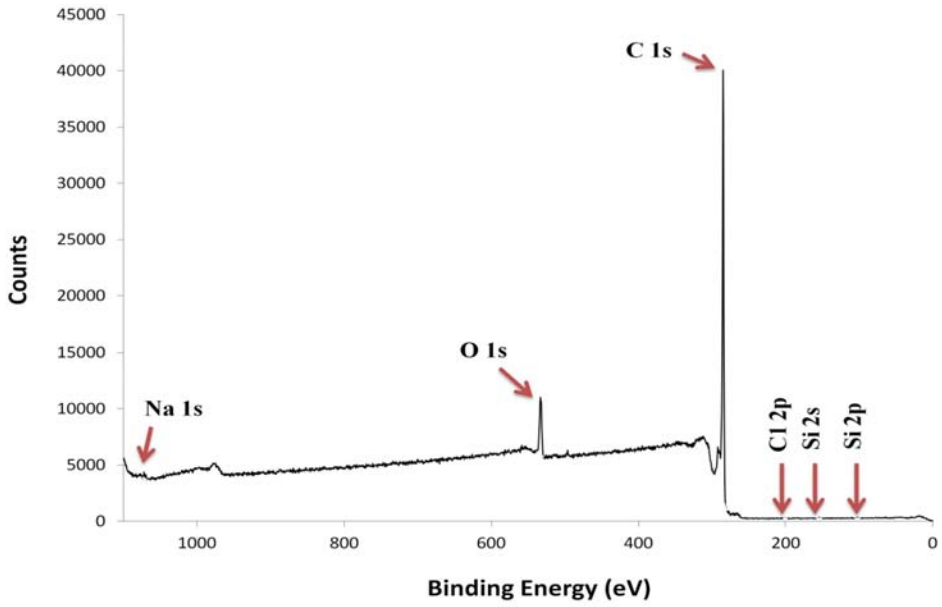

Figure 12: XPS Survey spectrum with the identified photoelectron peaks.

axis = 1.2mm, minor axis = 0.6mm, area = 0.6mm^2, depth = 8nm) using 1487eV monochromatic aluminum Kα x-ray beam. The elemental survey spectrum was over the binding energy range from 0 to 1100 eV, with a step size of 0.5eV. The results of the quantitative XPS spectra are presented in Table 2. Figure 12 shows the high-resolution XPS survey spectra. The primary elements present in the MWCNT scaffolds are carbon (94.1%) and oxygen (5.54). Additional elements include trace amounts of silicon (0.20%), sodium (0.13), and chlorine (0.03). Silicon (present as a silicone/polysiloxane, a common form silicone found in greases and sealant), sodium, and chlorine (a common trace impurity) are not likely to affect the high-resolution spectra of carbon. For, example if the silicon is present as polydimethyl siloxane, an increase of 0.44% in the carbon peak at 284.3eV would be recorded (0.47% of the total carbon peak intensity).

The carbon 1s peak was analyzed in two ways: (1) fit with an asymmetric line shape and a minimal number of component peaks (Table 3, Figure 13) [48], and (2) fits using the Voigt function as reported previously (Table 4, Figure 14) [49]. The primary difference between the two methods was the allowance of the C-C main peak at 285 eV to become asymmetric (in method 1). The asymmetry is predicted for the carbon nanotubes because of their tightly packed graphene structure. The asymmetry is further evidenced by a lack of clearly defined features in the tailing end of carbon peak prior to the features at 289.49 eV and 291.62 eV. Allowing this asymmetry resulted in a high quality of fit and self-consistent stoichiometry. Taking into account the stoichiometry of the –C(=O)O- peak (2.68% of the carbon resulting in 2.52% of the total atoms as carbon in –C(=O)O-) results in 5.05% of the atoms as oxygen in this bonding environment. By subtracting the

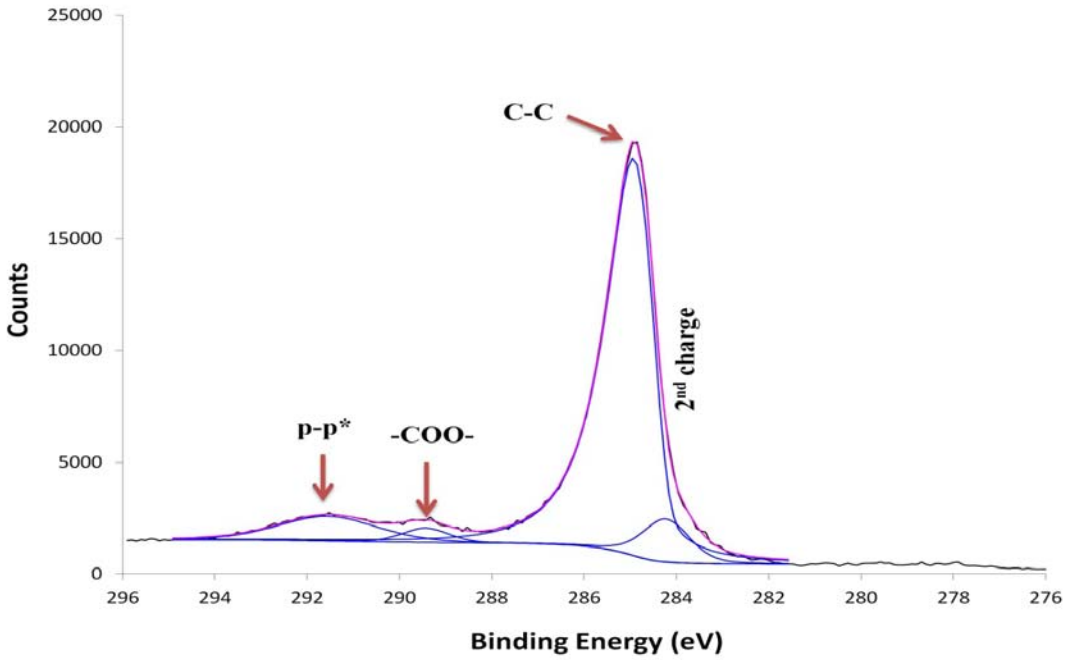

Figure 14: XPS high resolution scan of the carbon 1s photoelectron peak. Synthetic peaks fit using "Method 1", asymmetric peaks, features are identified as marked.

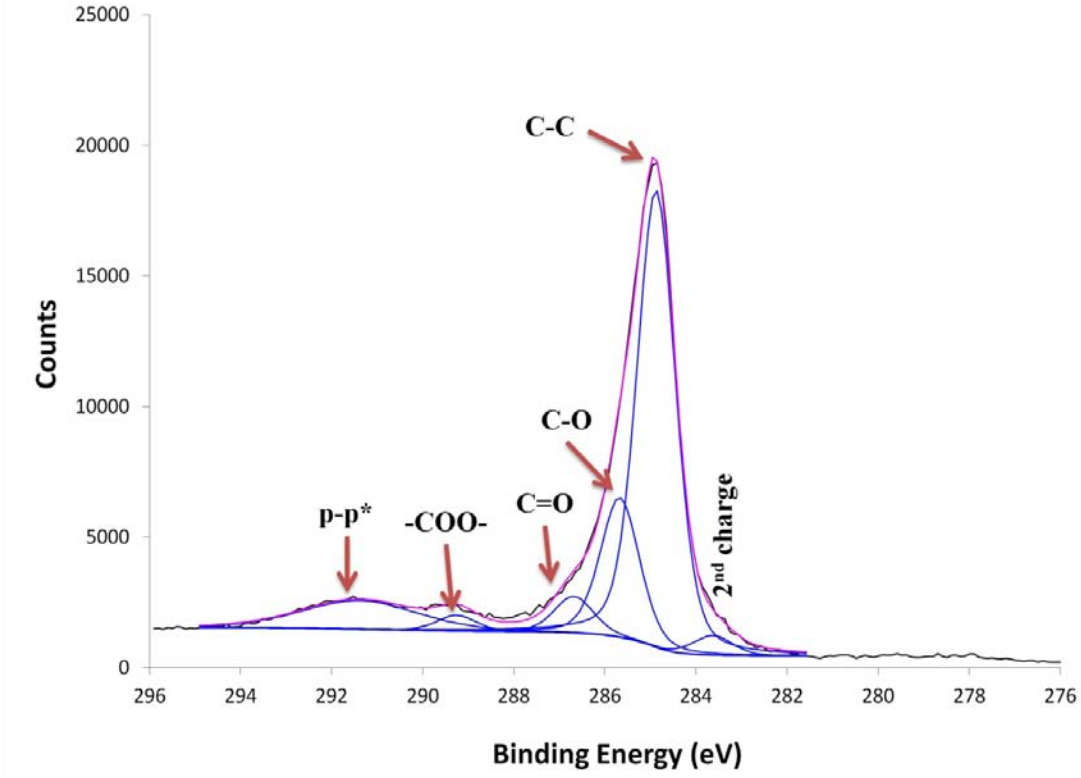

Figure 13: XPS high resolution scan of the carbon 1s photoelectron peak. Synthetic peaks fit using "Method 2", Okpalugo et al. peaks, features are identified as marked.

polysiloxane contribution in the oxygen 1s peak (0.54%), the total oxygen remaining is

5.00%, which corresponds to the –C(=O)O as measured in the carbon 1s peak.

The results from method 2 with the incorporation of the two additional oxygen functional groups and the forced symmetry of the Voigt function results in a 17.46% oxygen contribution in C-O groups and 4.63% in C=O groups. Taken together with the -COO- group, this corresponds to a total oxygen content of 26.08%, 5 times more than the total oxygen measured. Thus, this fitting protocol does not provide reasonable results. Each fitting protocol also resulted in a p -p* shakeup feature equal to ~10% of the total carbon

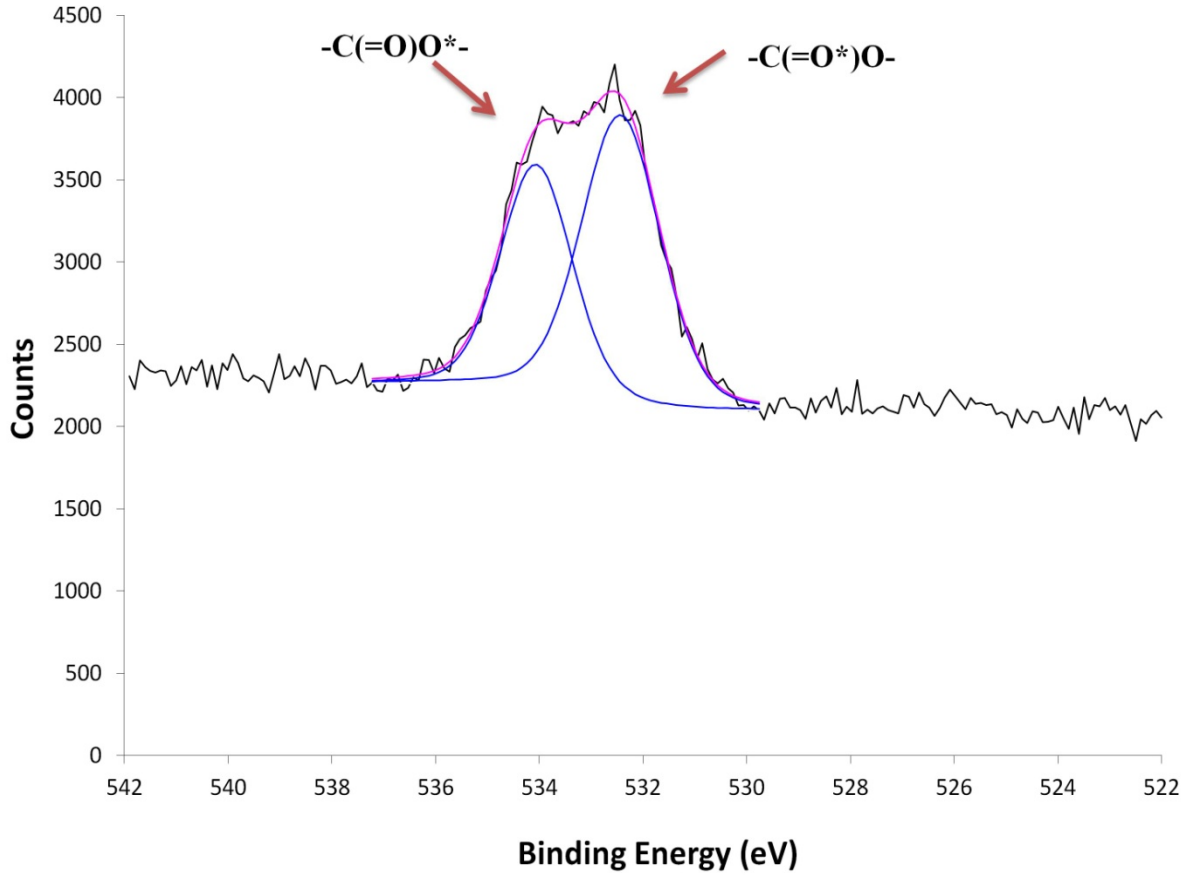

Figure 15: XPS high resolution scan of the oxygen 1s photoelectron peak. Features are identified as marked.

1s peak. This is the typical peak ratio for shakeup features from aromatic graphene surfaces such as MWCNTs or graphite. The oxygen 1s high resolution analysis (Table 5, Figure 15) resulted in two peaks, (1) the higher binding energy peak (534.12 eV) attributed to the single bonded oxygen in the –C(=O)O- group and (2) the lower energy peak corresponding to doubly bound oxygen in the –C(=O)O- group.

The bulk electrical conductivity of purified MWCNT scaffolds (cylinders, 6 mm length, 5 mm diameter, MWCNT: BP mass ratio = 1:4) was calculated to be 2×10^{-1} S cm^{-1} from four point resistivity measurements [50], and satisfy the conductivity requirements for a large number of electrical applications [51]. This electrical conductivity value is similar or higher than a large number of thin films prepared using carbon nanotubes or graphene with large networks of sp^2 carbon atoms, and scattered regions of sp^3 carbon atoms, but lower than thin films of carbon nanotubes or graphene with only sp^2 carbon networks [52-54]. Thus, the Raman, TGA, XPS, and conductivity results taken together implies that the chemical composition of the purified MWCNT scaffolds mainly comprises of sp^2 carbon networks with sp^3 carbon junctions at the crosslinking sites.

2.3.5 Electron Microscopy

SEM was performed on the MWCNT scaffolds to characterize their structure, and confirm the cross-linking of the nanotubes (Figure 16). Figure 16A and B show low-resolution SEM images of a representative unpurified MWCNT scaffold prepared by mixing MWCNT and BP in a ratio of 1:4. The cross-sections clearly show interconnected

MWCNT networks that form the macroscopic 3-D architecture. The high resolution SEM in Figure 16C and D also display the crosslinking between individual MWCNTs, and the formation of junctions (red arrows, Figure 16D). Unlike polymer chains that coil together tightly with no inter-chain space or air pockets, the cross-linked MWCNT network is highly porous. The pores are irregular shaped, and inter-connected. Representative high-magnification TEM images (Figure 17) display the formation of crosslinks between individual MWCNTs, further corroborating SEM results. Figure 18 displays representative low-magnification TEM images of MWCNT dispersions before crosslinking. The MWCNTs before crosslinking are present as individual or bundled nanotubes.

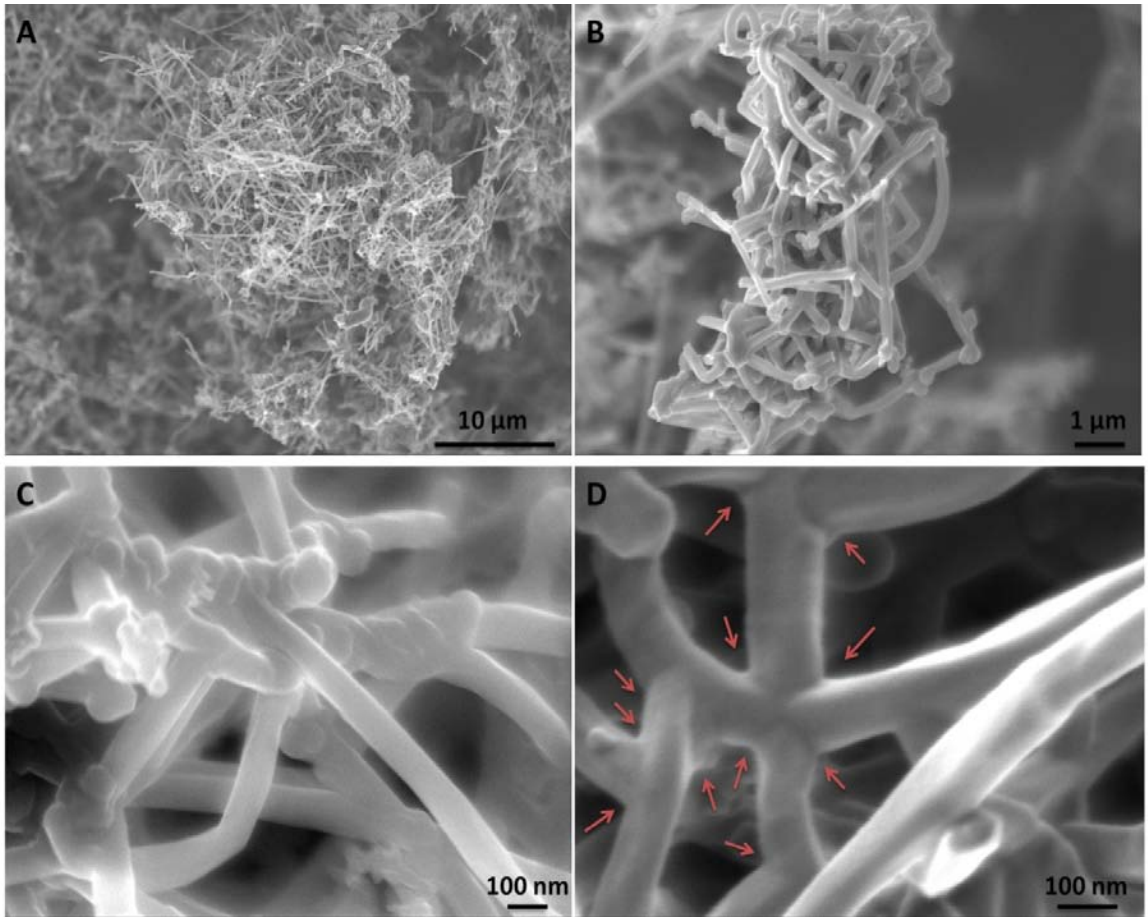

Figure 16: Representative low (A-B), and high (C-D) resolution scanning electron microscopy images of unpurified MWCNT scaffold cross-sections (MWCNT: BP mass ratio = 1: 4).

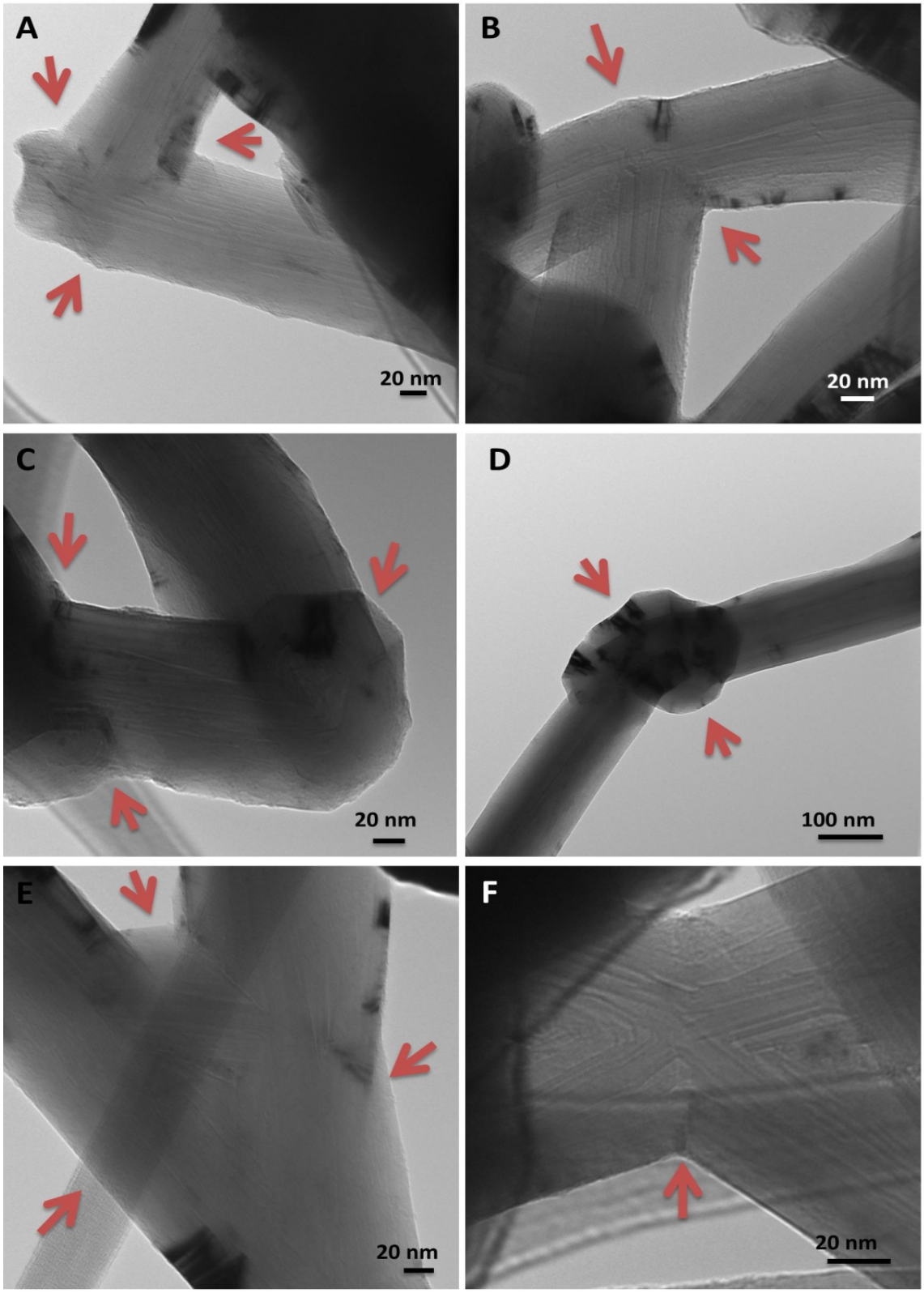

Figure 17: TEM Representative TEM images showing the formation of crosslinks between individual nanotubes (red arrows).

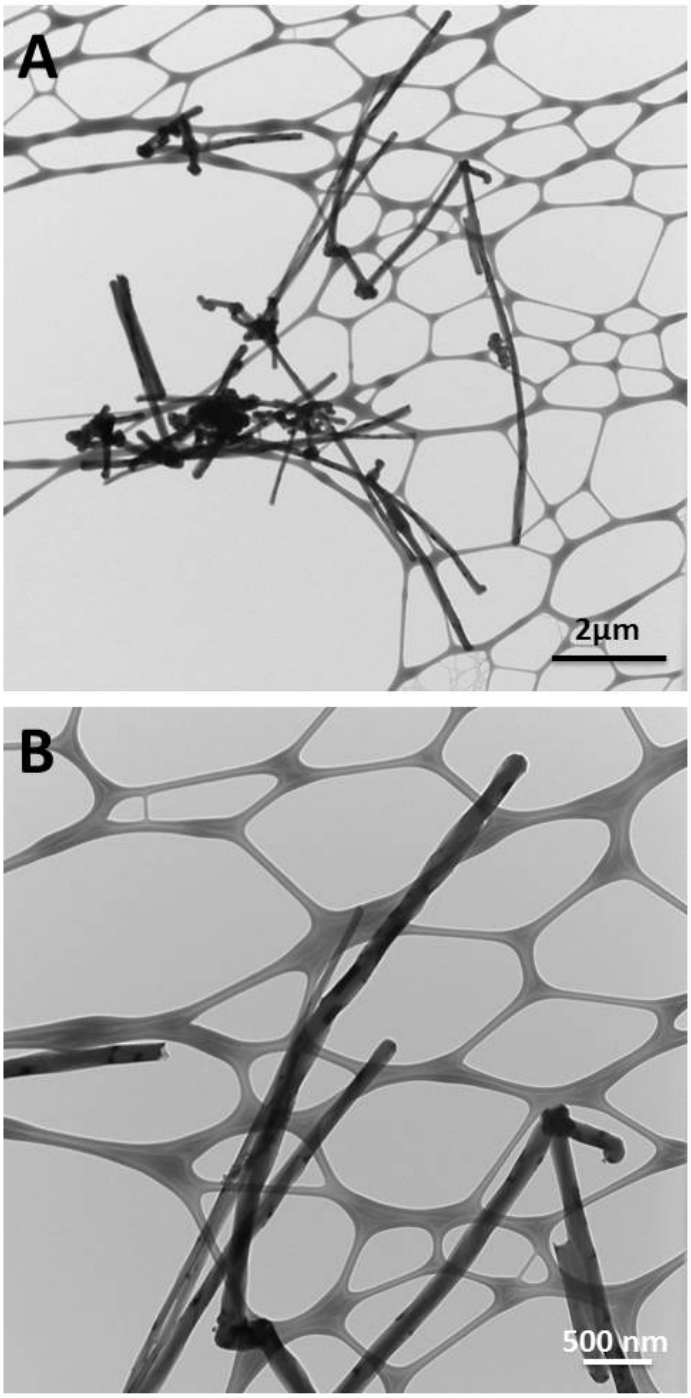

Figure 18: Representative TEM images of MWCNT dispersions before crosslinking. Analysis of this and other TEM images indicate that MWCNTs in the dispersion are present as individual or aggregated bundles. The length and outer diameter of individual MWCNT's were between ~ 2-9 µm and ~110-170 nm, respectively. The length and outer diameter of aggregated MWCNT's bundles were between ~ 5-9 µm ~ 250-400 nm, respectively.

2.3.6 Micro Computed Tomography (micro-CT) and SEM Image Processing

The porosity and pore size of the unpurified and purified MWCNT scaffolds was further evaluated by microCT and SEM image analysis. No statistically significant difference was observed in the porosity and pore size values for unpurified, and purified. Thus, only the analysis of purified MWCNTs is presented. MicroCT is a well-established method used to characterize the macroporosity of 3-D crosslinked scaffolds [55]. Figure 19A displays a 3-D reconstructed microCT image of a 1.23 mm x 1.23 mm x 1.23 mm section of a representative unpurified MWCNT (MWCNT: BP = 1:0.5) scaffold. Figure 19B, C, and D show the top, middle, and bottom section of the 3-D image displayed in Figure

19A, and clearly confirm the presence of pores (blue color represents the voids). These observations were consistent throughout all individual cross-sections of the microCT reconstructed images. The analysis of the microCT slices determined the pore sizes to be between 100-300 µm. The pores were interconnected, and distributed throughout the structure (see Appendix A movie 1 for a representative 360º view of 3-D microCT

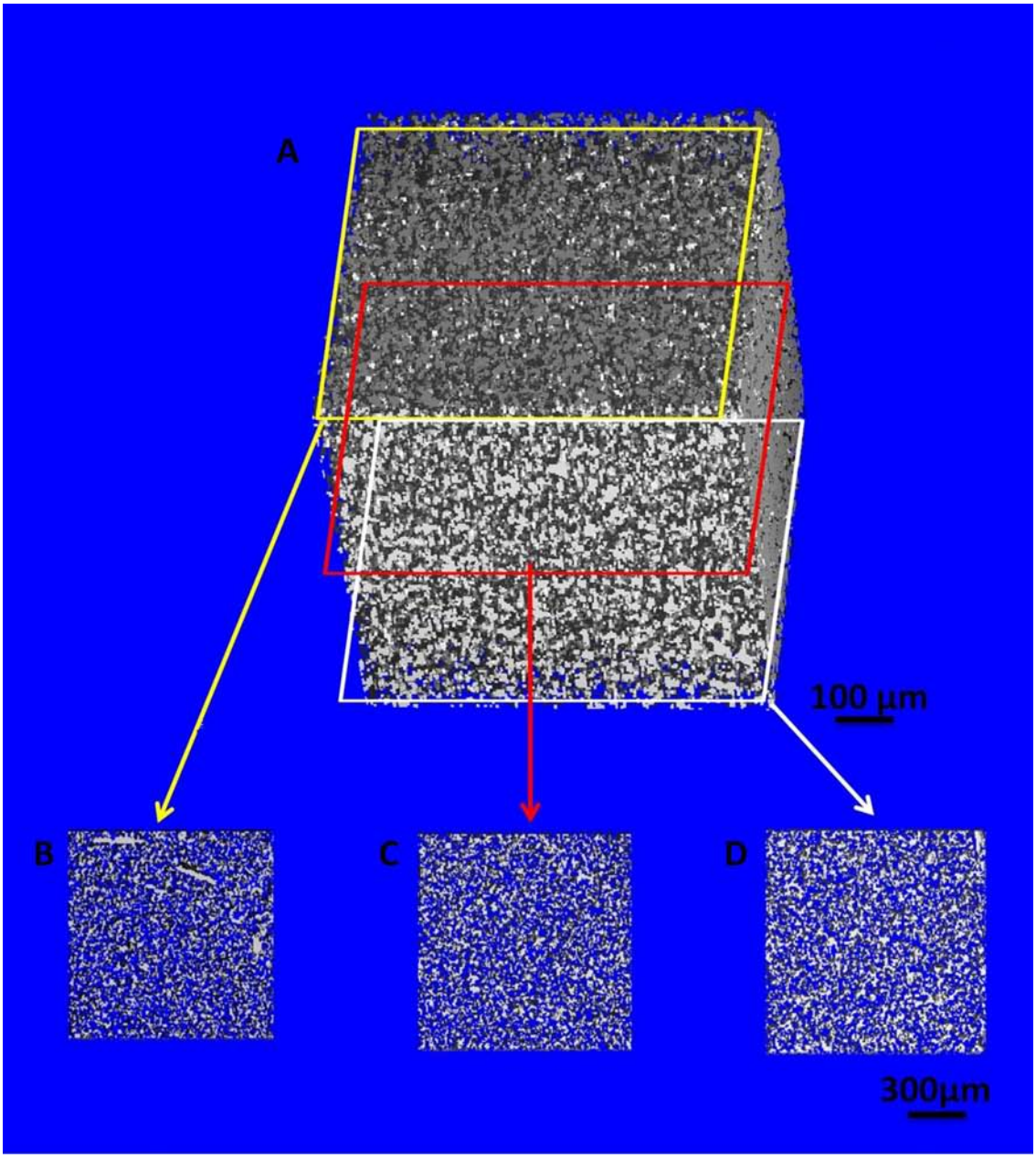

Figure 19: (A) Representative 3D reconstructed microCT image of unpurified MWCNT scaffold, and the (B) top, (C) middle and (D) bottom microCT slice of the reconstructed 3D MWCNT scaffold image. The blue color in the images represents void spaces. Scale bar: (A) 100 µm, (B, C and D) 300 µm (MWCNT: BP mass ratio = 1: 4).

reconstructed MWCNT scaffold. The scaffolds can be examined from any angle of view at up to 6 μm resolution by shifting, rotating, and magnifying them in virtual space, and provide further visual support of the interconnected pores).

The macroporosity of the scaffolds fabricated by mixing MWCNTs with BP at different mass ratios (between 1:0.5 to 1:4) was determined from the microCT data, and is presented in Figure 20 and Table 6. The results show that porosity of MWCNT scaffolds decreased from 85% to 21% with increase in the amount of BP added for crosslinking the MWCNTs. It should be noted that the white and grey solid interconnected structures (Figure 19B, C and D) in the microCT images have nanometer sized pores, which cannot be visualized due to the microCT's resolution limit of 6 μm. The macroporosity within these structures can be clearly visualized in the images by SEM (see Figure 16). To further quantify the macroporosity, a widely-used and accepted literature technique[56-59] was used to perform image processing on a series of SEM images, and calculate the porosity within the white solid structure structures seen in the microCT images (see methods section for details). The porosity calculated by this method corresponds to the surface porosity, and has been used to estimate the porosity values for sandstones, and tissue engineering polymeric scaffolds [56-59]. The pore sizes from this analysis were determined to be between 125-750 nm. The macroporosity of the various MWCNT scaffolds (MWCNT:BP mass ratios between 1:0.5, to 1:4) is presented in Figure 20B and Table 7. The results show a trend similar to the microCT porosity data with a decrease in porosity from 43.42% to 23.62% with increase in MWCNT:BP mass ratio.

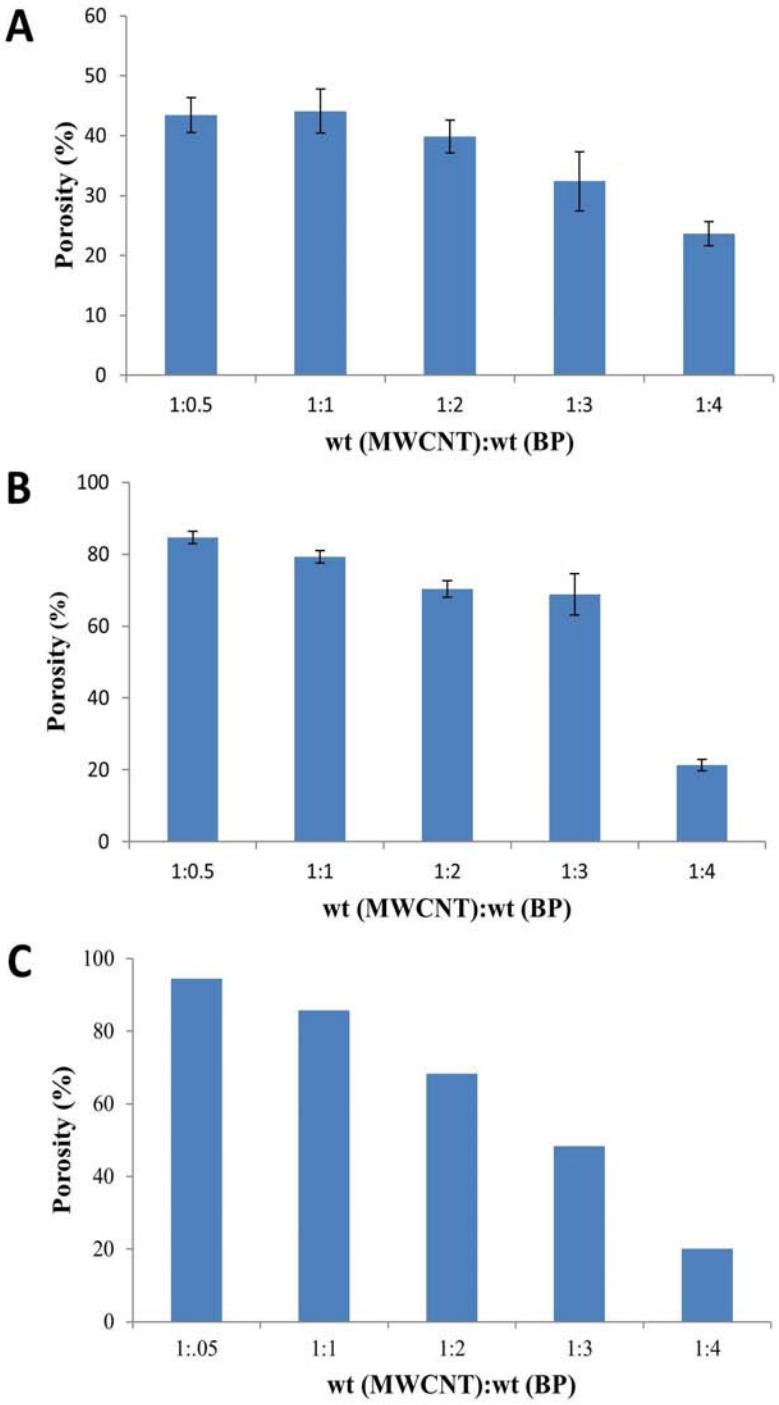

Figure 20: (A) & (B) are porosity of purified MWCNT scaffolds fabricated with different mass ratios of BP (between 1:0.5 to 1:4) as determined by and SEM image processing analysis and microCT, respectively. (C) Porosity of purified MWCNT scaffolds analyzed by liquid extrusion porosimetry.

2.3.7 Liquid Extrusion Porosimetry (LEP)

In addition to microCT and SEM image processing, LEP was performed to assess the porosity of MWCNT scaffolds. LEP is a widely used, IUPAC recommended, non-hazardous (no mercury) method to assess the porosity of ceramics, food products and nonwoven fibrous filter media beds [60-63]. The porosity (%) and median pore diameter for all MWCNT scaffolds (MWCNT:BP mass ratios between 1:0.5, to 1:4) is presented in Figure 20C and Table 8. The results show a trend similar to microCT and SEM image analysis. The macro-porosity and median pore diameter decreased from 94.48% to 20.19% and 324.48μm to 115.87μm, respectively, with increase in MWCNT:BP ratio. The microCT, SEM porosity and LEP results taken together indicate that the porosity of MWCNT scaffolds can be tuned by varying the amount of crosslinking agent – BP. The higher amount of BP leads to the increase in the amount of active sites on the MWCNTs thereby inducing a higher crosslinking, and thereby, alters the porosity [64].

The thermal cross-linking method discussed above to fabricate 3-D MWCNT scaffolds can be easily adapted to fabricate 3-D scaffolds of various geometries (e.g. disks or cylinders) with other carbon nanomaterials such 0-D fullerenes, 1-D single-walled carbon nanotubes or 2-D graphene as starting materials (see Figure 21A). Figure 21B-D show the SEM images of scaffolds fabricated using these nanomaterials. The SEM cross-sections clearly show the macroscopic 3-D architectures due the crosslinking of these carbon nanomaterials. The SWCNT scaffolds show topography similar to the MWCNT scaffolds. The fullerene and graphene scaffolds show topography that is distinctly different from the MWCNT and SWCNT scaffolds. Additional studies are required, and

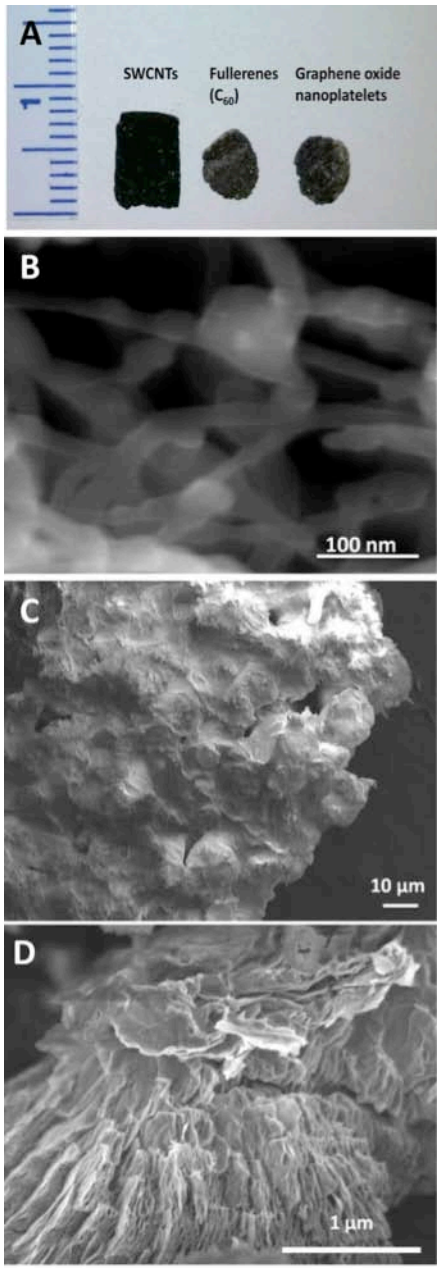

Figure 21: (A) Optical images of thermally-crosslinked 3D, macroscopic unpurified cylinder (5 mm diameter, 8 mm thickness), and discs (5 mm diameter, 3 mm thickness) fabricated using SWCNTs, fullerenes and graphene oxide nanoplatelets as starting material. (B), (C) and (D) are scanning electron microscopy images of unpurified scaffolds fabricated using SWCNTS, fullerenes and graphene oxide nanoplatelets, respectively.

are currently underway to understand how the dimensionality these nanoscale building blocks affects the structure, and porosity of the 3-D scaffolds. Nevertheless, the fabrication of these 3-D all carbon macro-sized scaffolds opens avenues for further experimental and theoretical studies to elucidate the structure- (geometry, porosity) function (thermal, mechanical, electrical, and electromagnetic properties) relationships.

The introduction of carbon nanotechnology into large number of macro-scale applications for energy storage [21, 65, 66], thermal management [67], catalysis [4], electronic devices [2], and biomedical implants [68] would require the assembly of nanoscale building-blocks such as carbon nanotubes, fullerenes, and graphene to be assembled in structurally robust 3D architectures. An important issue affecting this development is the formation of covalent junctions between the building blocks [20, 23]. The results of this work introduce a novel, facile, economical, and scalable method to fabricate 3D carbon nanotubes with

chemically cross-linked junctions between sp^2 carbon atoms, which can be easily adapted to other carbon nanostructures such as fullerenes and graphene. Additionally, while the scaffolds architectures presented in this work are disk-shaped or cylindrical, one can also envision adapting this fabrication method using molds with complex geometries to tailor the shapes of the scaffolds. The insights from further structure-function relationship studies should provide the guiding principles for the large-scale production of macroscopic all-carbon devices with specific requirements for applications in clean energy technology, information technology, and healthcare.

2.4 Conclusions

In this study, we report a simple method to fabricate macroscopic, 3-D, free standing, all-carbon scaffolds using multiwalled MWCNTs as the starting materials. The scaffolds prepared via radical initiated thermal crosslinking, and annealing of MWCNTs possess macroscale interconnected pores, robust structural integrity, stability, and conductivity. Varying the amount of radical initiator can control the porosity of the three-dimensional structure. This method also allows fabrication of 3-D scaffolds using other carbon nanomaterials such as single-walled carbon nanotubes, fullerenes, and graphene indicating that it could be used as a versatile method for 3-D assembly of carbon nanostructures with pi bond networks. Additionally, the fabrication process of the scaffolds is rapid, economical, and scalable, and can be adapted to fabricate scaffolds with various geometries (e.g. cylinders, disks) thereby opening avenues for structure-function studies towards the development of macroscopic all-carbon devices.

2.5 Tables

Table 1: Mechanical properties of MWCNT scaffolds determined by nanoindentation

Indent #	*MWCNT:BP 1:1*		*MWCNT:BP 1:2*	
	Er (MPa)	**H (MPa)**	**Er (MPa)**	**H (MPa)**
1	39.44	1.89	55.62	2.07
2	35.01	1.74	39.87	4.77
3	33.84	1.96	28.72	0.73
4	31.77	1.97	38.94	4.83
5	16.12	1.01	84.08	4.72
6	53.4	2.77	34.59	2.26
7	59.59	1.4	38.25	4.91
Mean ± SD	38.45 ± 14.42	1.82 ± 0.54	45.72 ± 18.78	3.47 ± 1.73

Table 2: Atomic concentrations of elements detected in the MWCNT scaffold

Element	**Atomic Concentration (%)**
Carbon (C)	94.10
Oxygen (O)	5.54
Silicon (Si)	0.20
Sodium (Na)	0.13
Chlorine (Cl)	0.03

Table 3: High-energy resolution XPS results for the carbon (C1s) peak with an asymmetric carbon peak in the MWCNT scaffold

Component	Binding Energy (eV)	FWHM	Asymmetry (%)	Group (%)
Polysiloxane (2nd charge state)	284.29	1.199	0.000	7.88
C-C	285.00	1.231	47.832	80.15
-COO-	289.49	1.195	0.000	2.68
π-π*	291.62	2.508	0.000	9.29

Table 4: High-energy resolution XPS results for the carbon (C1s) peak with symmetric carbon peaks using the Voigt function

Component	Binding Energy	FWHM	Group (%)
Polysiloxane (2nd charge state)	283.75	1.011	2.63
C-C	285.00	1.008	60.76
C-O	285.79	1.008	18.56
C=O	286.81	1.012	4.93
-COO-	289.39	1.010	2.12
π-π*	291.51	3.010	10.99

Table 5: High-energy resolution XPS results for the oxygen (O1s) peak in MWCNT scaffold

Component	Binding Energy	FWHM	Group (%)
-C(=O*)O- /Polysiloxane	532.50	1.797	58.39
-C(=O)O*-	534.12	1.623	41.62

Table 6: Porosity of MWCNT scaffolds calculated from microCT analysis

MWCNT: BP Ratio	Porosity (%) by microCT
1:0.5	84.67 ± 1.70
1:1	79.26 ± 1.77
1:2	70.29 ± 2.34
1:3	68.80 ± 5.72
1:4	21.31 ± 1.52

Table 7: Porosity of MWCNT scaffolds calculated from SEM analysis

MWCNT: BP Ratio	Porosity (%) by SEM image processing
1:0.5	43.424 ± 2.88
1:1	44.121 ± 3.66
1:2	39.895 ± 2.72
1:3	32.389 ± 4.93
1:4	23.623 ± 2.02

Table 8: Porosity and median pore diameter of MWCNT scaffolds determined from liquid extrusion porosimetry

MWCNT: BP Ratio	Porosity (%) by liquid extrusion porosimetry	Median pore diameter (μm)
1:0.5	94.485	324.48
1:1	85.684	312.96
1:2	68.275	288.76
1:3	48.305	141.00
1:4	20.194	115.87

2.6 Acknowledgements

This work was sponsored by National Institutes of Health (grants No. 1DP2OD007394-01). Four point resistivity measurements were performed at CFN, BNL, which is supported by the U.S. Department of Energy, Office of Basic Energy Sciences, under Contract No. DE-AC02-98CH10886.

2.7 References

1. Dai, H., *Carbon nanotubes: synthesis, integration, and properties.* Acc Chem Res, 2002. **35**(12): p. 1035-44.

2. Sun, D.M., et al., *Flexible high-performance carbon nanotube integrated circuits.* Nat Nanotechnol, 2011. **6**(3): p. 156-61.

3. Fan, Z., et al., *A three-dimensional carbon nanotube/graphene sandwich and its application as electrode in supercapacitors.* Adv Mater, 2010. **22**(33): p. 3723-8.

4. Xiong, W., et al., *3-D carbon nanotube structures used as high performance catalyst for oxygen reduction reaction.* J Am Chem Soc, 2010. **132**(45): p. 15839-41.

5. Ma, L. and G. Sines, *Fatigue of isotropic pyrolytic carbon used in mechanical heart valves.* J Heart Valve Dis, 1996. **5 Suppl 1**: p. S59-64.

6. Sitharaman, B., et al., *In vivo biocompatibility of ultra-short single-walled carbon nanotube/biodegradable polymer nanocomposites for bone tissue engineering.* Bone, 2008. **43**(2): p. 362-70.

7. Huang, J.Q., et al., *Patterning of hydrophobic three-dimensional carbon nanotube architectures by a pattern transfer approach.* Nanoscale, 2010. **2**(8): p. 1401-4.

8. Ren, Z.F., et al., *Synthesis of large arrays of well-aligned carbon nanotubes on glass.* Science, 1998. **282**(5391): p. 1105-7.

9. Bennett, R.D., et al., *Creating patterned carbon nanotube catalysts through the microcontact printing of block copolymer micellar thin films.* Langmuir, 2006. **22**(20): p. 8273-6.

10. De Volder, M., et al., *Diverse 3D microarchitectures made by capillary forming of carbon nanotubes.* Adv Mater, 2010. **22**(39): p. 4384-9.

11. Qu, J., et al., *Tailoring of three-dimensional carbon nanotube architectures by coupling capillarity-induced assembly with multiple CVD growth.* Journal of Materials Chemistry, 2011. **21**(16).

12. Chakrapani, N., et al., *Capillarity-driven assembly of two-dimensional cellular carbon nanotube foams.* Proc Natl Acad Sci U S A, 2004. **101**(12): p. 4009-12.

13. Endo, M., et al., *Nanotechnology: 'buckypaper' from coaxial nanotubes.* Nature, 2005. **433**(7025): p. 476.

14. Cao, A., et al., *Super-compressible foamlike carbon nanotube films.* Science, 2005. **310**(5752): p. 1307-10.

15. Xu, M., et al., *Carbon nanotubes with temperature-invariant viscoelasticity from -196 degrees to 1000 degrees C.* Science, 2010. **330**(6009): p. 1364-8.

16. Gui, X., et al., *Carbon Nanotube Sponges.* Advanced Materials, 2010. **22**(5): p. 617-621.

17. Worsley, M.A., et al., *Mechanically robust and electrically conductive carbon nanotube foams.* Applied Physics Letters, 2009. **94**(7): p. 073115-3.

18. Kim, K.H., Y. Oh, and M.F. Islam, *Graphene coating makes carbon nanotube aerogels superelastic and resistant to fatigue.* Nat Nanotechnol, 2012. **7**(9): p. 562-6.

19. Schiffres, S.N., et al., *Gas Diffusion, Energy Transport, and Thermal Accommodation in Single-Walled Carbon Nanotube Aerogels.* Advanced Functional Materials, 2012: p. n/a-n/a.

20. Worsley, M.A., et al., *Synthesis of Graphene Aerogel with High Electrical Conductivity.* Journal of the American Chemical Society, 2010. **132**(40): p. 14067-14069.

21. Zhang, X., et al., *Mechanically strong and highly conductive graphene aerogel and its use as electrodes for electrochemical power sources.* Journal of Materials Chemistry, 2011. **21**(18): p. 6494-6497.

22. Biener, J., et al., *Advanced carbon aerogels for energy applications.* Energy & Environmental Science, 2011. **4**(3): p. 656-667.

23. Hashim, D.P., et al., *Covalently bonded three-dimensional carbon nanotube solids via boron induced nanojunctions.* Sci. Rep., 2012. **2**.

24. Paratala, B.S., et al., *Physicochemical Characterization, and Relaxometry Studies of Micro-Graphite Oxide, Graphene Nanoplatelets, and Nanoribbons.* PLoS ONE, 2012. **7**(6): p. e38185.

25. Oliver, W.C. and G.M. Pharr, *Improved techniques for determining hardness and elastic modulus using load and displacement sensing indentation experiments.* Journal of Materials Research, 1992. **7**(6): p. 1564-1580.

26. Mesarovic, S.D., et al., *Mechanical behavior of a carbon nanotube turf.* Scripta Materialia, 2007. **56**(2): p. 157-160.

27. Ozcivici, E., et al., *Determination of bone's mechanical matrix properties by nanoindentation.* Methods Mol Biol, 2008. **455**: p. 323-34.

28. Judex, S., et al., *Genetically Based Influences on the Site-Specific Regulation of Trabecular and Cortical Bone Morphology.* Journal of Bone and Mineral Research, 2004. **19**(4): p. 600-606.

29. Jena, A. and K. Gupta, *Liquid extrusion techniques for pore structure evaluation of nonwovens.* International Nonwovens Journal, 2003. **12**(3): p. 45-53.

30. Jena, A. and K. Gupta, *Determination of Pore Volume and Pore Distribution by Liquid Extrusion Porosimetry Without Using Mercury*, in *26th Annual Conference on Composites, Advanced Ceramics, Materials, and Structures: B: Ceramic Engineering and Science Proceedings*. 2008, John Wiley & Sons, Inc. p. 277-284.

31. Braun, D., *Origins and Development of Initiation of Free Radical Polymerization Processes.* International Journal of Polymer Science, 2009. **2009**.

32. Ying, Y., et al., *Functionalization of carbon nanotubes by free radicals.* Org Lett, 2003. **5**(9): p. 1471-3.

33. Peng, H., et al., *Sidewall functionalization of single-walled carbon nanotubes with organic peroxides.* Chem Commun (Camb), 2003(3): p. 362-3.

34. Graeme Moad, D.H.S., *The Chemistry of Radical Polymerization*, 2006, Elsevier: Amsterdam ; Boston.

35. Ishigami, N., et al., *Microreactor utilizing a vertically-aligned carbon nanotube array grown inside the channels.* Chem Commun (Camb), 2007(16): p. 1626-8.

36. Dresselhaus, M.S., et al., *Raman spectroscopy of carbon nanotubes.* Physics Reports, 2005. **409**(2): p. 47-99.

37. Zyat'kov, I.P., et al., *Effect of fluorine-containing substituents on spectralstructural characteristics of aroyl peroxides.* Journal of Applied Spectroscopy, 1983. **39**(1): p. 798-802.

38. Vacque, V., et al., *Characterisation of the O瑇O peroxide bond by vibrational spectroscopy.* Spectrochimica Acta Part A: Molecular and Biomolecular Spectroscopy, 1997. **53**(1): p. 55-66.

39. Baibarac, M., et al., *Vibrational and photoluminescence properties of the polystyrene functionalized single-walled carbon nanotubes.* Diamond and Related Materials, 2008. **17**(7–10): p. 1380-1388.

40. Baskaran, D., J.W. Mays, and M.S. Bratcher, *Noncovalent and Nonspecific Molecular Interactions of Polymers with Multiwalled Carbon Nanotubes.* Chemistry of Materials, 2005. **17**(13): p. 3389-3397.

41. Rinzler, A.G., et al., *Large-scale purification of single-wall carbon nanotubes: process, product, and characterization.* Applied Physics A: Materials Science & Processing, 1998. **67**(1): p. 29-37.

42. Hou, P., et al., *Purification of single-walled carbon nanotubes synthesized by the hydrogen arc-discharge method.* Journal of Materials Research, 2001. **16**(09): p. 2526-2529.

43. Chen, I.W.P., et al., *Highly conductive carbon nanotube buckypapers with improved doping stability via conjugational cross-linking.* Nanotechnology, 2011. **22**(48): p. 485708.

44. Kosynkin, D.V., et al., *Longitudinal unzipping of carbon nanotubes to form graphene nanoribbons.* Nature, 2009. **458**(7240): p. 872-876.

45. Gibson, L.J. and M.F. Ashby, *Cellular Solids: Structure and Properties*. 1997: Cambridge University Press.

46. Xu, Y., et al., *Self-Assembled Graphene Hydrogel via a One-Step Hydrothermal Process.* ACS Nano, 2010. **4**(7): p. 4324-4330.

47. Tang, Z., et al., *Noble-Metal-Promoted Three-Dimensional Macroassembly of Single-Layered Graphene Oxide.* Angewandte Chemie International Edition, 2010. **49**(27): p. 4603-4607.

48. Estrade-Szwarckopf, H., *XPS photoemission in carbonaceous materials: A "defect" peak beside the graphitic asymmetric peak.* Carbon, 2004. **42**(8–9): p. 1713-1721.

49. Okpalugo, T.I.T., et al., *High resolution XPS characterization of chemical functionalised MWCNTs and SWCNTs.* Carbon, 2005. **43**(1): p. 153-161.

50. Smits, F., *Measurement of sheet resistivities with the four-point probe.* Bell Syst. Tech. J, 1958. **37**(3): p. 711-18.

51. Chung, D.D.L., *Electrical applications of carbon materials.* Journal of Materials Science, 2004. **39**(8): p. 2645-2661.

52. Lau, C., et al., *The effect of functionalization on structure and electrical conductivity of multi-walled carbon nanotubes.* Journal of Nanoparticle Research, 2008. **10**(0): p. 77-88.

53. Sahoo, N.G., et al., *Polymer nanocomposites based on functionalized carbon nanotubes.* Progress in Polymer Science, 2010. **35**(7): p. 837-867.

54. Stankovich, S., et al., *Graphene-based composite materials.* Nature, 2006. **442**(7100): p. 282-286.

55. Shi, X., et al., *Fabrication of porous ultra-short single-walled carbon nanotube nanocomposite scaffolds for bone tissue engineering.* Biomaterials, 2007. **28**(28): p. 4078-90.

56. Guarino, V., et al., *Image processing and fractal box counting: user-assisted method for multi-scale porous scaffold characterization.* Journal of Materials Science: Materials in Medicine, 2010. **21**(12): p. 3109-3118.

57. McCullen, S.D., et al., *Characterization of electrospun nanocomposite scaffolds and biocompatibility with adipose-derived human mesenchymal stem cells.* Int J Nanomedicine, 2007. **2**(2): p. 253-63.

58. Grove, C. and D.A. Jerram, *jPOR: An ImageJ macro to quantify total optical porosity from blue-stained thin sections.* Computers & Geosciences, 2011. **37**(11): p. 1850-1859.

59. Hunt, R.K.R.K.P., *Mineralogy of fine-grained sediment by energy-dispersive spectrometry (EDS) image analysis – a methodology*. Environmental Geology, 2002. **42**(1): p. 32-40.

60. Jean Rouquerol, et al., *Liquid intrusion and alternative methods for the characterization of macroporous materials (IUPAC Technical Report).* Pure and Applied Chemistry, 2012. **84**(1): p. 107-136.

61. Miller, B. and I. Tyomkin, *Liquid Porosimetry: New Methodology and Applications.* Journal of Colloid and Interface Science, 1994. **162**(1): p. 163-170.

62. Datta, A.K., et al., *Porous media characterization of breads baked using novel heating modes.* Journal of Food Engineering, 2007. **79**(1): p. 106-116.

63. Hutten, I.M.M., *Handbook of Nonwoven Filter Media*. 2007: Elsevier.

64. Manley, T.R. and M.M. Qayyum, *Crosslinked polyethylene at elevated temperatures.* Polymer, 1972. **13**(12): p. 587-592.

65. Kolpak, A.M. and J.C. Grossman, *Azobenzene-Functionalized Carbon Nanotubes As High-Energy Density Solar Thermal Fuels.* Nano Letters, 2011. **11**(8): p. 3156-3162.

66. Lee, S.W., et al., *High-power lithium batteries from functionalized carbon-nanotube electrodes.* Nat Nano, 2010. **5**(7): p. 531-537.

67. Romo-Herrera, J.M., et al., *Covalent 2D and 3D Networks from 1D Nanostructures: Designing New Materials.* Nano Letters, 2006. **7**(3): p. 570-576.

68. Shi, X., et al., *In vitro cytotoxicity of single-walled carbon nanotube/biodegradable polymer nanocomposites.* J Biomed Mater Res A, 2008. **86**(3): p. 813-23.

Chapter 3

IN-VITRO CYTOCOMPATIBILITY OF THREE-DIMENSIONAL MACROSCOPIC ALL-CARBON SCAFFOLDS

Preface

Portions of this chapter have been reproduced from:

Gaurav Lalwani, Anu Gopalan, Michael D' Agati, Jeyantt Srinivas Sankaran, Stefan Judex, Yi-Xian Qin and Balaji Sitharaman, "Porous Three-Dimensional Carbon Nanotube Scaffolds for Tissue Engineering", Under Review, Journal of Biomedical Materials Research Part A, 2015

The authors listed in the above manuscript have contributions towards the data reported in this chapter.

3.1 Introduction

Tissue engineering scaffolds should ideally provide suitable 3D microenvironment with desirable mechanical support for cell proliferation and extracellular matrix (ECM) deposition. The bulk-, micro-, and nano-scale material and biochemical properties (e.g. mechanical stiffness, pore architecture, topography, covalent functionalization with proteins, growth factors, and therapeutic ligands) of scaffolds play an important role in regulating cellular functions such as attachment, proliferation, differentiation, and tissue maturation [1-4]. Scaffolds are routinely fabricated using biodegradable polymers such as poly(lactic-co-glycolic) acid, poly(propylene fumarate), poly(hydroxypropyl methacrylate) etc. using various methods such as rapid prototyping[5], electrospinning[6], freeze drying[7], phase separation[8], solvent casting and particulate leaching[9], gas foaming[10], and sol-gel crosslinking[11] for applications in bone, heart, skin, muscle, and other tissue engineering [12]. However, the intrinsic material properties of current scaffolds lack additional multifunctional attributes such as ability to induce/guide specific cellular processes (such as differentiation, specific protein expression), support non-invasive longitudinal diagnosis/monitoring of tissue regeneration, and permit stimulus based drug and gene delivery [13].

Carbon nanomaterials such as fullerenes, carbon nanotubes and graphene exhibit excellent physiochemical properties such as high mechanical strength, and electrical conductivity as well as unique electromagnetic, opto-acoustic response, and thus, their multifunctional characteristics have been exploited for several biomedical applications

such as bioimaging[14-16], stem cell applications[17, 18], drug and gene delivery[19, 20], and photodynamic therapy [21, 22]. They have also been incorporated into polymeric scaffolds as mechanical reinforcing agents [23, 24] or contrast agents [25] to improve non-invasive imaging of the structural properties and biological response of polymeric scaffolds (e.g. porosity, vascularization) under physiological conditions. Thus, the assembly of these carbon nanostructures into three-dimensional (3-D) architectures would harness their physio-chemical properties towards the development of the next-generation tissue engineering scaffolds.

Indeed, there has been a growing interest in assembling carbon nanomaterials into various two- and three-dimensional architectures for the fabrication of next-generation of biomedical devices and implants [26-35]. For example, carbon nanotubes and graphene have been assembled into two-dimensional films (using vacuum filtration and chemical vapor deposition (CVD) methods) and 3D foams (using CVD and sacrificial template-transfer methods) and their cytocompability has been examined for applications in bone, neuron and cardiac tissue engineering [26-38]. However, these methods exhibit several limitations. CVD method requires very specific substrates capable of withstanding high temperatures and pressure [39]. Vacuum filtration and spray coating methods can produce 2D substrates that may not be suitable for tissue engineering of larger organs that require three-dimensional scaffolds [32, 40]. In general, the above methods do not allow control over tuning the pore size or porosity of substrates. Thus, most of the cytocompatibility studies using above mentioned carbon nanotube or graphene films and foams have mainly been restricted to their surface. The propensity of films and foams

prepared using these methods to allow cellular infiltration; an important characteristic of a scaffold for tissue regeneration still needs to be demonstrated. Additionally, these approaches may present a practical challenge to fabricate macro-scale scaffolds (at least >1mm in all 3 dimensions) either due to scalability issues, or high operational costs. Furthermore, a general limitation of these methods is that, in the absence of strong chemical bonds between the individual nanomaterials, the structural integrity of architectures assembled relies mainly on weak Van der Waal forces or on physical entanglement of the nanoparticles, and is vulnerable to dissociation under *in vivo* physiological shear forces. The assembly of carbon nanomaterials into mechanically robust 3D (especially with sizes >1 mm in all three dimensions) macroporous tissue engineering scaffolds with tunable porosity across various lengths (macro, micro and nanoscopic) would constitute a significant advancement.

Recently, we reported a simple scalable method to fabricate chemically-crosslinked macroscopic, 3-D, free standing, all-carbon architectures using fullerenes, single- and multi-walled carbon nanotubes, and graphene as the starting materials [41]. The architectures, prepared by radical initiated thermal crosslinking of the sp^2 carbon bonds, and annealing of these carbon nanostructures, possess nano-, and micro- scale-interconnected pores, robust structural integrity, and stability. The fullerene, carbon nanotube and graphene structures show topography that is distinctly different. Varying the amount of radical initiator can control the porosity of the three-dimensional architectures. The results demonstrated that this method could be used as a versatile method for 3-D assembly of carbon nanostructures with pi bond networks to design

porous and complex geometries tailored towards specific electronic, material science or biomedical applications.

In this study, towards the development of multifunctional 3D scaffolds for tissue engineering applications, we have fabricated two type of porous all-carbon scaffolds prepared using single- and multi- walled carbon nanotubes (SWCNTs and MWCNTs) employing the aforementioned method and investigate the cell-scaffold interactions. We characterize the cytocompatibility of these scaffolds using MC3T3 cells. Specifically, we examine the cell viability, adhesion, proliferation and infiltration of MC3T3 cells on 3D MWCNT and SWCNT scaffolds. Porous polymeric scaffolds prepared using the FDA approved biodegradable biocompatible polymer poly (lactic acid co-glycolic acid) (PLGA) were used as controls.

3.2 Materials and methods

3.2.1 Fabrication of PLGA, MWCNT and SWCNT scaffolds

MWCNTs (Sigma–Aldrich, NY, USA), SWCNTs (CheapTubes Inc., NY, USA), PLGA (Polysciences Inc., PA, USA), benzoyl peroxide (BP, Sigma–Aldrich, NY, USA) and chloroform ($CHCl_3$, Fisher Scientific, PA, USA) were used as purchased. Porous PLGA scaffolds with ~ 85% porosity were fabricated using a thermal-crosslinking particulate-leaching technique using NaCl as the porogen as described elsewhere [42]. MWCNT and

SWCNT scaffolds were fabricated by mixing nanomaterials with BP at a mass ratio of MWCNT/SWCNT:BP = 1:0.05. $CHCl_3$ was added to the mixture to dissolve BP and the slurry was subjected to bath sonication (Ultrasonicator FS30H, Fischer Scientific, Pittsburgh, PA) for 15 minutes to ensure uniform dispersion. Post sonication, the slurry was poured into custom machined Teflon® molds (cylinder, length = 1.2 mm, diameter = 6 mm) and incubated at 60°C for 24 h. Post incubation, the MWCNT and SWCNT scaffolds were obtained by disassembling the molds. For purification (to remove the excess BP), scaffolds were subjected to series of washing ($CHCl_3$ washes) and heating steps (150°C for 30 minutes).

3.2.2 Scanning electron microscopy (SEM)

To characterize the morphology of scaffolds, SEM imaging was performed using a JOEL 7600F Analytical high resolution SEM at the Center for Functional Nanomaterials, Brookhaven National Laboratory, New York. PLGA, MWCNT and SWCNT scaffolds were placed on double-sided conductive carbon tape and sputter coated with 3 nm of silver (Ag). SEM was operated at 5 kV accelerating voltage and images were captured using a secondary electron imaging (SEI) detector.

3.2.3 Micro-computed tomography (microCT)

MicroCT was used to quantify the micro-porosity of PLGA, MWCNT and SWCNT scaffolds. High resolution microCT scanning was performed using a microCT 40 system (Scanco Medical AG, Bassersdorf, Switzerland) at an energy and intensity level corresponding to 55 kV voltage and 145 μA current with 300 ms integration time for 1000 projections. A Gaussian filter was used to suppress noise. The scaffold was isolated from the background, using a thresholding procedure that was specific to each material. The values to segment scaffold from background were optimized individually by comparing the 2D gray scale image of a single slice of a material with the thresholded image. Three different regions covering a circular area of 1 mm^2 and a depth of 0.5 mm were chosen in the center to minimize the inclusion of edge artifacts. Total volume (TV), scaffold volume (SV) and scaffold volume fraction (SV/TV) were determined for each scaffold. The mean and standard deviations for these three different regions were used for statistical comparisons. Porosity values were determined as:

$$Porosity\ (\%) = \left(1 - \left(\frac{SV}{TV}\right)\right) * 100$$

3.2.4 Image processing

3.2.4.1 Image processing for porosity analysis

Image processing toolbox in MATLAB (MathWorks®, MA, USA) was used to quantify the nano-porosities of MWCNT and SWCNT scaffolds. SEM images were cropped to remove the scale bar and subjected to processing steps such as thresholding, edge detection, filteration, and quantification of region properties. Porosity was calculated for n=5 images using the formula:

$$Porosity\ (\%) = ((\sum Area\ of\ voids)/(area\ of\ image)\ ) * 100$$

3.2.4.2 Image processing for surface roughness

Surface roughness values of MWCNT and SWCNT scaffolds were determined by image processing of a series of SEM images acquired at different depths of focus using ImageJ (Bethesda, MD, USA). Arithmetic (R_a) and mean roughness (R_q) values were determined for n=10 images by a roughness calculation plugin that determines the surface peaks and valleys altitude to calculate roughness values using the following equations:

$$R_a = \frac{1}{n} \int_{i=1}^{n} |Z(x)|\, dx$$

$$R_q = \sqrt{\frac{1}{n} \int_{i=1}^{n} Z^2(x) dx}$$

3.2.5 Cell culture

National Institutes of Health mouse MC3T3 pre-osteoblast cells (MC3T3 cells, ATCC, Manassas, VA, USA) were used for cytocompatibility studies. MC3T3 cells were grown in minimum essential medium alpha (MEM-α, Gibco Life Technologies) media, supplemented with 10 vol. % fetal bovine serum (FBS, Gibco Life Technologies, NY, USA) and 1 vol. % antibiotics (penicillin- streptomycin, Gibco Life Technologies, NY, USA). Media was changed twice a week, and cells were maintained at 37°C in a

humidified environment of 5% CO_2-95% O_2. For cytocompatibility studies, purified MWCNT and SWCNT scaffolds were washed with $CHCl_3$ and placed in an oven at 110°C followed by a series of washes (3X) with $CHCl_3$ (to remove residual BP) and a graded series of ethanol (100%-70%). PLGA scaffolds were only washed with graded series of ethanol, not $CHCl_3$. The scaffolds (PLGA, MWCNT and SWCNT) were then subjected to UV sterilization for 24 hours followed by washes with phosphate buffered saline (PBS) and cell culture media. For pre-wetting, the scaffolds were incubated with blank cell culture media for 24 hours prior to cell seeding. MC3T3 cells were trypsinized, resuspended in MEM-α, and seeded on the scaffolds at a density of 250,000 cells/scaffold in 30 µl media (added in 2 intervals of 15 µl). Cells were allowed to attach on the scaffolds for 2 hours before addition of complete media (1 ml) to each well of the 24-well plate. The cells were cultured for 1, 3 and 5 days on the scaffolds.

3.2.6 Lactate dehydrogenase (LDH) assay

LDH assay is used for the quantification of cell death as a measure of membrane integrity of cells. LDH assay was performed using a commercial LDH kit (TOX-7, Sigma Aldrich, NY, USA) as per manufacturer's instructions. Briefly, after each time point (1, 3 and 5 days), 50 µl media was collected from each well of the 24-well plate (n=6 for each scaffold group) and transferred to a fresh 96-well plate. A total of 100 µl of LDH assay mixture was added to each well and incubated in dark for 45 minutes. To stop the reaction, 1N HCl (10% volume) was added to each well. Absorbance values were recorded using a 96 well plate reader (Molecular Devices, CA, USA) at 490 nm. Positive

control cells (100% dead) were prepared by incubating MC3T3 cells grown on tissue culture polystyrene with lysis buffer for 45 minutes before centrifugation. Cells cultured on PLGA scaffolds served as the baseline control. Total LDH release (% of positive control) was expressed as the percentage of $(OD_{test} - OD_{blank})/(OD_{positive} - OD_{blank})$, where OD_{test} is the optical density of cells cultured on PLGA, MWCNT or SWCNT scaffolds, OD_{blank} is the optical density of 96-well plate without cells, and $OD_{positive}$ is the optical density of positive control (100% dead cells). Absorbance of blank culture media was measured for baseline correction.

3.2.7 Calcein-AM fluorescence imaging

Calcein – AM (calcein acetoxymethyl ester) upon internalization by live cells is converted to calcein (a green fluorescent dye) due to the hydrolytic removal of acetoxymethyl ester group by intracellular esterases. Therefore, calcein selectively stains live cells that can be visualized using a fluorescence microscope. After 1, 3, and 5 days, media was removed and scaffolds were washed with PBS. 1 ml of Calcein-AM dye (4μM) was added to each well and incubated at 37°C in dark for 20 minutes. The scaffolds were transferred to 35 mm glass bottom dishes (Mattek Corporation, Ashland, MA) and imaged by a confocal laser-scanning microscope (Zeiss LSM 510 Meta NLO Two-Photon) using Zeiss LSM Image Browser software (version 4.2, Carl Zeiss Microimaging, Thornwood, NJ).

3.2.8 Immunofluorescence for focal adhesion and cell proliferation

Immunofluorescence was performed as reported previously [40]. Briefly, glutaraldehyde fixed cells on PLGA, MWCNT, and SWCNT scaffolds were washed with PBS and incubated with 2% glycine for 5 minutes for blocking. The scaffolds were placed in 0.5% Triton-X-100 permeabilizing buffer (composition: 10.3 g sucrose, 0.29 g NaCl, 0.4 g Hepes buffer, 0.06 g $MgCl_2$, and 0.5 ml Triton-X-100 in 100 ml of DI water) for 25 minutes. Scaffolds were then washed with immunofluorescence buffer (IFB, 0.1% Triton-X-100 and 0.1% BSA in PBS) and incubated with commercially available monoclonal antibodies. Scaffolds were incubated for 1 hour with either anti-proliferating Ki-67 antibody (2 µl/ml in IFB, Cat. No. MA5-14520, Thermo Scientific, New York, USA) for cell proliferation analysis or monoclonal anti-vinculin antibody (2 µl/ml in IFB, Cat. No. V4139, Sigma Aldrich, NY, USA) for visualization of focal adhesion sites. After 1 hour of incubation with primary antibodies, the scaffolds were washed with IFB (3X) and incubated with secondary antibody (anti-rabbit TRITC, 2 µl/ml in IFB, Cat. No. T6778, Sigma Aldrich, New York, USA) for 1 hour. Scaffolds were then washed with IFB (3X) and the cytoplasm was stained with FITC-conjugated phalloidin (2 µl/ml in PBS) for 1 hour to visualize actin filaments (cytoskeleton). Samples were imaged using a confocal laser-scanning microscope (Zeiss LSM 510 Meta NLO Two-Photon) equipped with Zeiss LSM Image Browser software (version 4.2, Carl Zeiss Microimaging, Thornwood, NJ).

3.2.9 SEM imaging for cellular attachment

To visualize cell attachment on scaffolds, glutaraldehyde fixed cells on PLGA, MWCNT and SWCNT scaffolds were subjected to dehydration steps using graded ethanol washes (70%-100%), air dried, and vacuum dried for 24 hours. Scaffolds were then sputter coated with 3 nm of silver (Ag) and imaged using a JOEL 7600F Analytical high resolution SEM (Center for Functional Nanomaterials, Brookhaven National Laboratory, New York) at an accelerating voltage of 2 kV.

3.2.10 Image processing to assess cellular infiltration

Z-stacks of calcein stained MC3T3 cells on PLGA, MWCNT and SWCNT scaffolds were acquired using a confocal laser-scanning microscope (Zeiss LSM 510 Meta NLO Two-Photon). Individual Z-stacks were then imported to ImageJ (Bethesda, MD, USA) and subjected to spectral coding using a time-lapse color coder plugin to false-color each slice as a function of depth (Z-height, i.e. depth of cellular infiltration). The multiple spectrally color-coded slices of Z-stacks were then compressed to form one composite image and reported.

3.2.11 Statistical analysis

Data is reported as mean ± standard deviation. Statistical analysis was performed for a 95% confidence interval ($p < 0.05$) using students 't' test. To analyze the differences between the groups, one-way anova followed by Tukey Kramer post hoc analysis was performed.

3.3 Results

3.3.1 Fabrication of PLGA, MWCNT and SWCNT scaffolds

PLGA scaffolds with 85% porosity were fabricated using an established procedure of thermal crosslinking particulate-leaching technique using NaCl as the porogen [42]. MWCNT and SWCNT scaffolds were fabricated using radical initiated thermal-

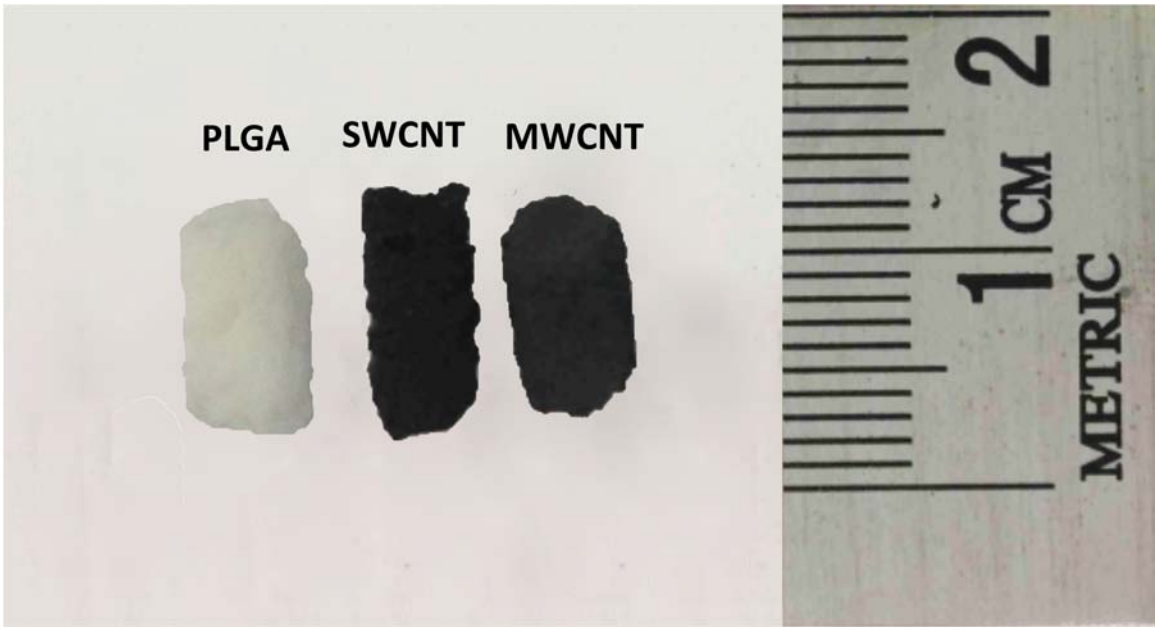

Figure 22: Optical images of representative three-dimensional porous poly(lactic-co-glycolic) acid, single walled carbon nanotube and multi walled carbon nanotube scaffolds prepared as cylinders (5 mm diameter, ~8-10 mm length).

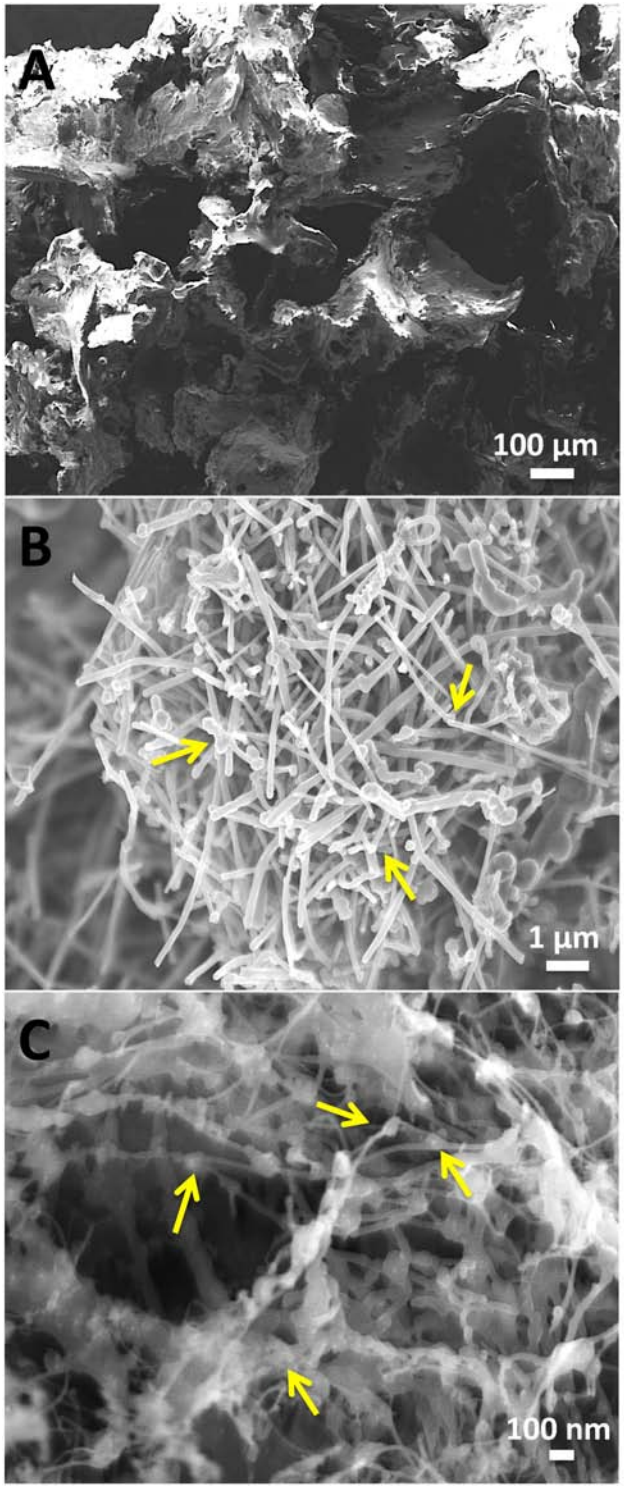

Figure 23: Representative scanning electron microscopy images of (A) poly(lactic-co-glycolic) acid, (B) multi walled carbon nanotube and (C) single walled carbon nanotube scaffolds. Yellow arrows images (B) and (C) correspond to the formation of nanoscale junctions (crosslinks) between CNTs.

crosslinking procedure [41]. Figure 22 displays the digital images of PLGA, MWCNT and SWCNT scaffolds used for cytocompatibility studies. The scaffolds are 3D porous are cylinders with ~ 5-8 mm in height and ~ 4-6 mm diameter. For cytocompatibility studies, the scaffolds were cut into smaller 3D cylinders of ~ 4 mm height to ensure uniformity between all the groups.

3.3.2 Characterization of scaffolds

3.3.2.1 Scanning electron microscopy

SEM was used for the morphological characterization of scaffolds. Figure 23 shows cross-sectional SEM images of PLGA, MWCNT and SWCNT scaffolds. All scaffolds possess porous architecture and pores appear well

interconnected. PLGA scaffolds (Figure 23 A) show characteristic cubic pore architecture of pore sizes between 300-500 µm, corresponding to the size distribution of NaCl crystals. Large openings and interconnected porous architecture are clearly visible. MWCNT and SWCNT scaffolds (Figure 23B and C, respectively) show interconnected MWCNT and SWCNT networks that form the 3D architecture. The MWCNT and SWCNT networks appear highly porous with irregularly shaped interconnected pores, and formations of junctions are also clearly visible (yellow arrows, Figure 23 B and C).

3.3.2.2 Microcomputed tomography (porosity)

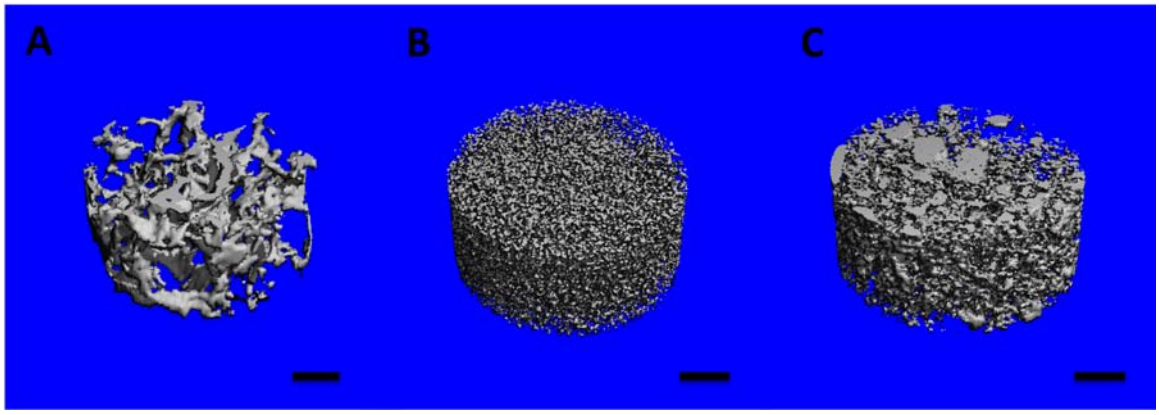

Figure 24: Representative three-dimensional microcomputed tomography reconstructions of (A) poly(lactic-co-glycolic) acid, (B) multi walled carbon nanotube and (C) single walled carbon nanotube scaffolds. The blue color represents void spaces. Scale bars are 200 µm.

MicroCT is a well-established method to determine the porosity of 3D polymeric and carbon nanotube scaffolds [41, 42]. Figures 3 A-C display the reconstructed microCT images of cylindrical sections (1 mm^2 area, 0.5 mm height) of PLGA, MWCNT and SWCNT scaffolds. The analysis of microCT images determined macro-pore sizes

between 300-500 µm for PLGA scaffolds and between 100-400 µm for MWCNT and SWCNT scaffolds. The porosity values of PLGA, MWCNT and SWCNT scaffolds, determined by microCT were 86.61 ± 1.91%, 91.69 ± 1.43% and 83.79 ± 5.75%, respectively (Table 9). It should be noted that the white and grey solid interconnect structures in Figures 3 B and C possess nanoscale pores that cannot be visualized by microCT due to a resolution of 6 µm. These pores are clearly visualized by SEM imaging (Figure 23 B and C).

3.3.2.3 Image processing for porosity analysis

Nanoscale porosity of scaffolds is vital for the transport of nutrients and exchange of waste metabolites, a feature important for scaffold biocompatibility. Therefore, to quantify the nanoscale porosity values in MWCNT and SWCNT scaffolds, a widely accepted technique was used to perform image processing on a series of SEM images. The porosity values calculated using this method correspond to surface porosity and have been used to estimate the porosities of tissue engineering scaffolds [41, 43, 44]. PLGA scaffolds have macroscopic pores (~300-500 µm) and their porosity is accurately determined using microCT since the pore sizes of PLGA scaffolds are greater than the resolution limit of microCT system. Also, PLGA scaffolds lack nano-porosity, therefore, due to these reasons; SEM image processing was not used to assess the porosity of PLGA scaffolds. The porosity values of MWCNT and SWCNT scaffolds were 45.82 ± 3.59% and 38.62 ± 2.91%, respectively (Table 9). The pore sizes determined from this method

were between 45 nm – 850 nm for MWCNT scaffolds and 20 nm – 950 nm for SWCNT scaffolds.

3.3.2.4 Image processing for nanoscale surface roughness analysis

Nanotopography of tissue engineering scaffolds plays a role in regulating cellular function [3, 45]. Therefore, ImageJ was used to characterize the nanoscale surface roughness of MWCNT and SWCNT scaffolds. The arithmetic and mean roughness values are reported in Table 9. These values are based on pixel intensity (not absolute metric units) as the SEM images were 8 bit with a pixel value of 0 a.u. (arbitrary units) represented as black and value of 255 a.u. represented as white. Values in between produce intermediate grey intensities. Therefore, these values can only be used for qualitative comparison between the surface roughness of MWCNT and SWCNT scaffolds. The arithmetic roughness (R_a) values for MWCNT and SWCNT scaffolds are 137.19 ± 12.25 a.u. and 89.31 ± 16.05 a.u., respectively. The mean roughness (R_q) values for MWCNT and SWCNT scaffolds are 146.76 ± 12.29 a.u. and 105.07 ± 13.75 a.u., respectively.

3.3.3 Cytotoxicity and cell proliferation analysis

3.3.3.1 LDH Assay

LDH assay measures the amount of cytosolic enzyme lactate dehydrogenase (LDH) released in the cell culture media by apoptotic or necrotic cells (compromised cell membranes). The released LDH present in the media catalyzes the conversion of lactate to pyruvate simultaneously reducing NAD^+ to NADH, which subsequently catalyzes the conversion of iodonitrotetrazolium (INT) to a water-soluble formazan product. The red colored formazan product is quantified as a measure of cell death. Figure 25 shows the total LDH released (normalized to positive controls) from MC3T3 cells after 1, 3, and 5 days of culture on PLGA, MWCNT and SWCNT scaffolds. Cells on SWCNT scaffolds show a slightly higher LDH release (~ 58%) compared to live cells grown on tissue culture polystyrene (TCPS, ~ 49%) after day 1. However, in comparison to TCPS controls after days 3 and 5, no significant differences were observed between total LDH

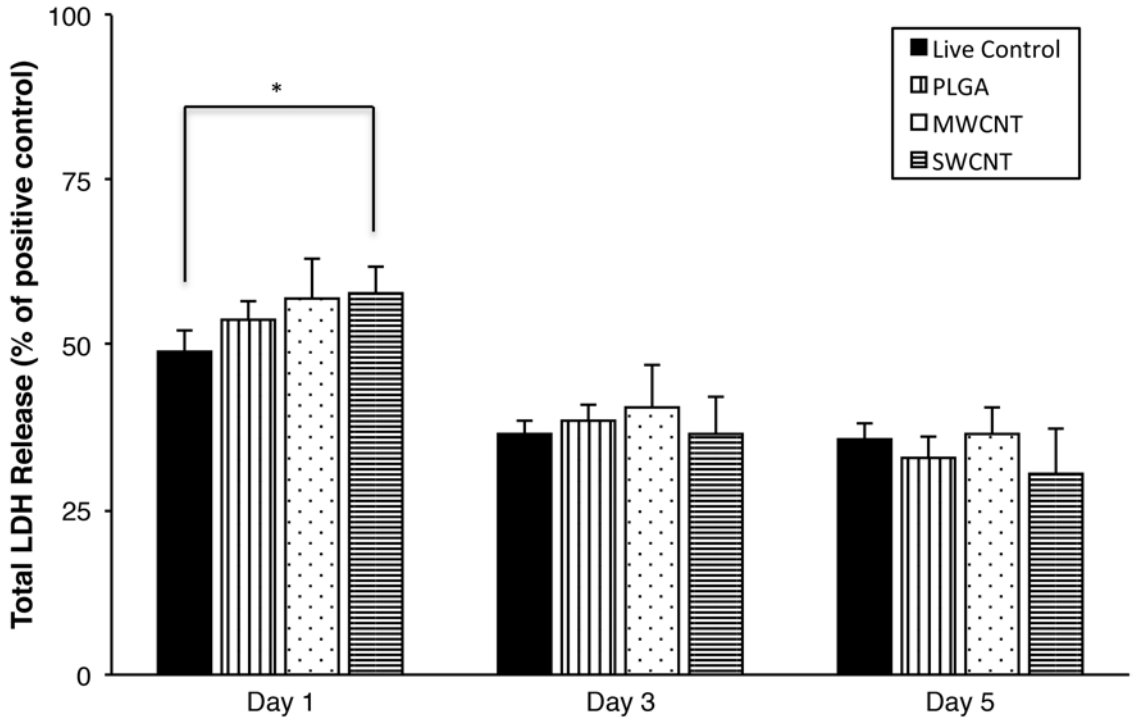

Figure 25: Cytotoxicity evaluation using LDH assay after 1, 3, and 5 days of MC3T3 cell culture on poly(lactic-co-glycolic) acid, multi walled carbon nanotube, and single walled carbon nanotube scaffolds. Chart represents total LDH release (%) normalized to positive controls (100% dead cells). Data is represented as means ± standard deviation. Groups with a significant difference ($p < 0.05$) are marked with "*".

released by MC3T3 cells on PLGA, MWCNT and SWCNT scaffolds (LDH release was between ~ 30-40% for all groups).

3.3.3.2 Calcein-AM staining

Calcein-AM staining is widely used in cell viability assays to selectively stain living eukaryotic cells [14, 21]. Calcein-AM is a non-fluorescent dye, which upon cellular internalization, is converted to green fluorescent calcein due to removal of acetoxymethyl ester group by intracellular esterases, and is retained in the cytoplasm of living cells. Figure 26 shows representative calcein-AM stained images of MC3T3 cells cultured on PLGA (Figure 26 A-C), MWCNT (Figure 26 D-F) and SWCNT (Figure 26 G-I) scaffolds after 1, 3, and 5 days. After 24 hours of incubation, presence of live MC3T3 cells on PLGA, MWCNT and SWCNT scaffolds was be observed, as shown in Figure 26 A, D, and G, respectively. Differences in cellular morphology were also observed between groups. Cells on PLGA and MWCNT scaffolds showed elongated spindle shaped morphology whereas cells on SWCNT scaffolds showed circular morphology (day 3, Figure 26 H) that begin spreading and retain their characteristic spindle shaped morphology by day 5. However, as clearly noticeable by comparing Figures 26 F and I, cells on MWCNT scaffolds appear more elongated than cells on SWCNT scaffolds, Furthermore, for each scaffold group, an increase in the number of green-fluorescent cell number was observed at day 5 compared to day 1.

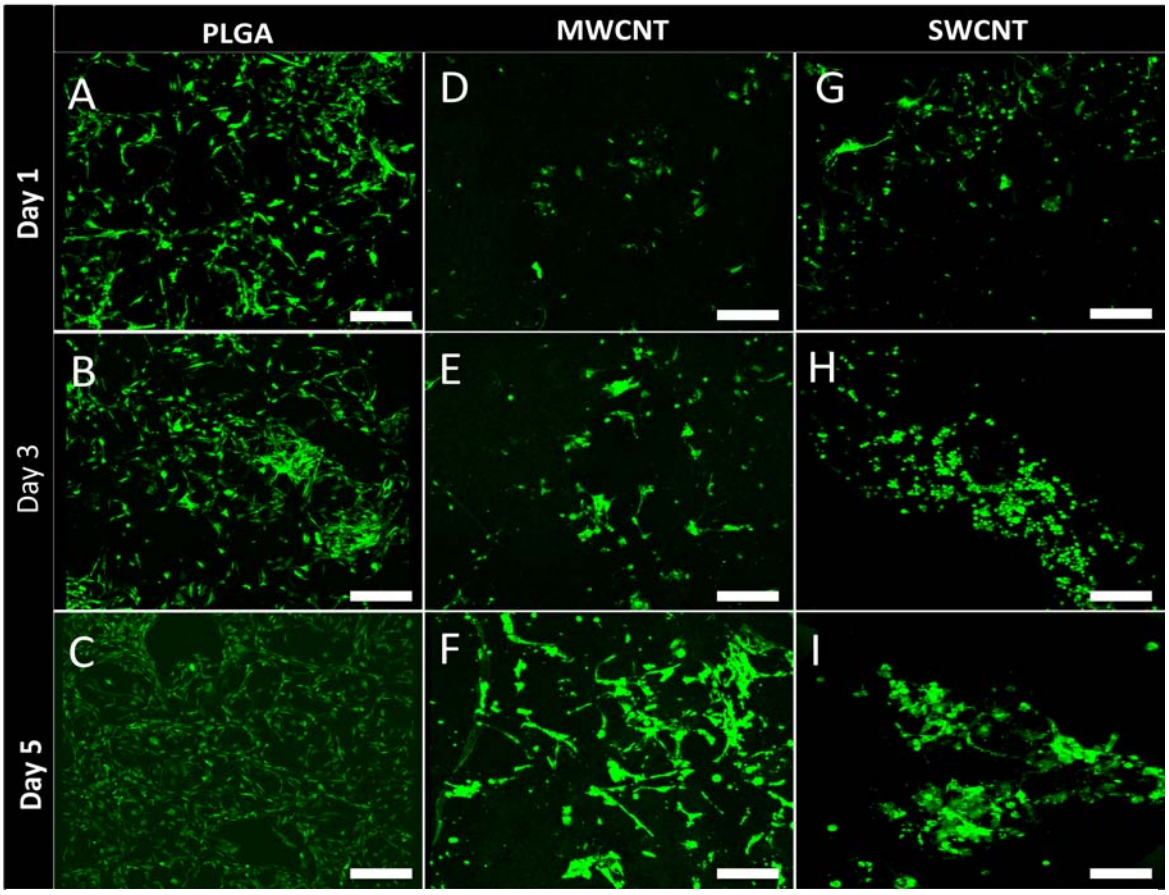

Figure 26: Representative calcein-AM stained green fluorescence images of MC3T3 cells on (A-C) poly(lactic-co-glycolic) acid, (D-F) multi walled carbon nanotube and (G-I) single walled carbon nanotube scaffolds after 1, 3, and 5 days of culture. Presence of live cells (green fluorescence) on all scaffold groups can be observed. Scale bars are 200 µm.

3.3.4 Immunofluorescence analysis

3.3.4.1 Cell attachment (vinculin - focal adhesion)

Vinculin is a membrane cytoskeletal protein important for the formation of focal adhesion assembly, and has been widely used as a marker to characterize cell-matrix adhesion [46]. Figure 27 shows representative confocal microscopy images of immunofluorescence staining for vinculin protein expressed by MC3T3 cells cultured on PLGA (Figure 27 A-C), MWCNT (Figure 27 D-F) and SWCNT (Figure 27 G-I)

scaffolds after 5 days. MC3T3 cells were stained with FITC-conjugated phalloidin for green fluorescence corresponding to actin cytoskeleton (green fluorescence, Figure 27, Panel A) and fluorescently labeled antibodies for vinculin expression (red fluorescence, Figure 27, Panel B). To ascertain co-localization of actin filaments and vinculin protein expression, merged images of panel A and panel B are presented in Figure 27, Panel C. Figure 27 A, D, G confirm the expression of vinculin by MC3T3 cells cultured on PLGA,

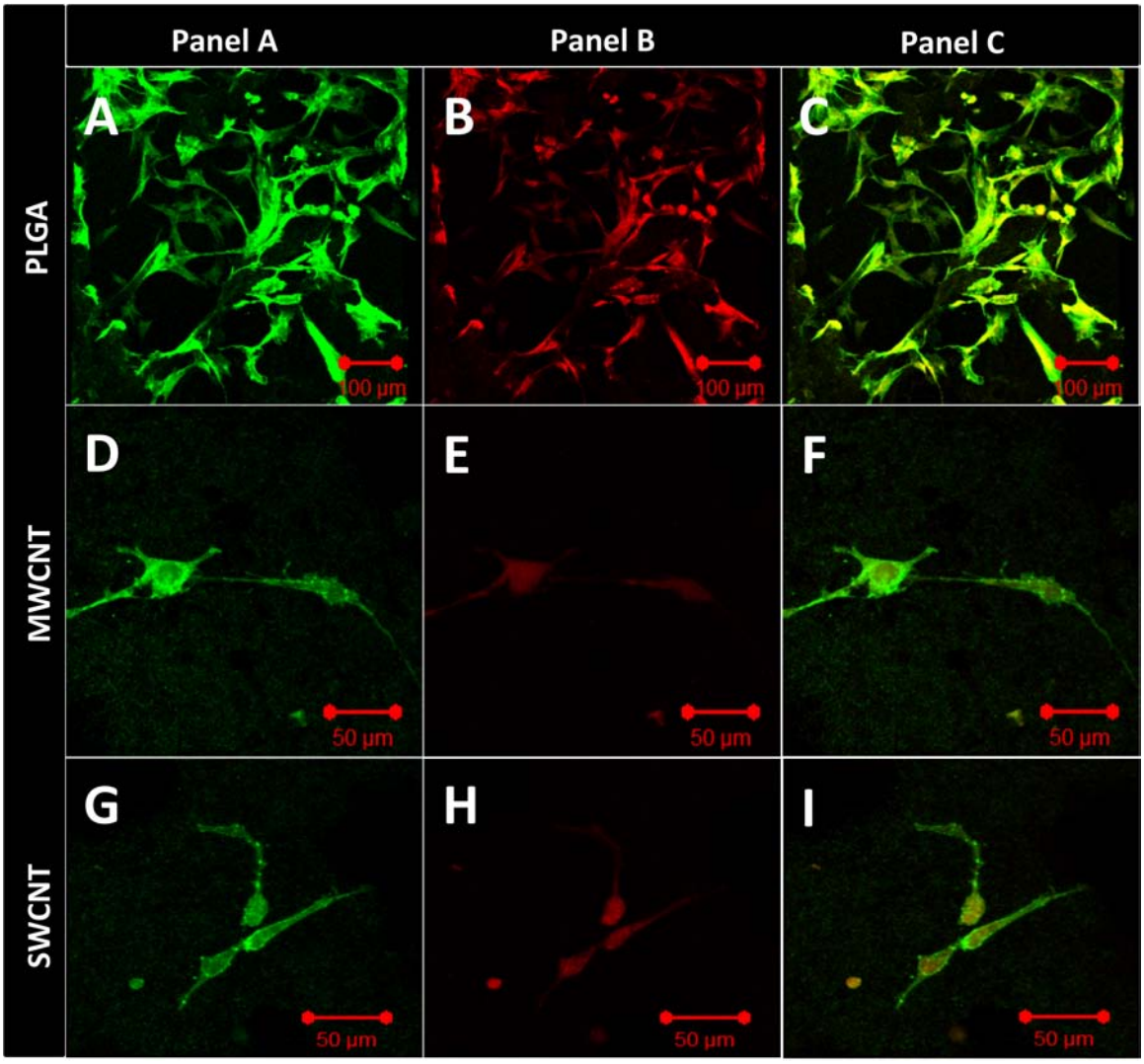

Figure 27: Representative immunofluorescence images of MC3T3 cells cultured on (A-C) poly(lactic-co-glycolic) acid, (D-F) multi walled carbon nanotube and (G-I) single walled carbon nanotube scaffolds after 5 days stained green for actin cytoskeleton (Panel A) and red for focal adhesions, i.e. vinculin protein (Panel B). Panel C shows superimposed images of panels A and B showing the co-localization of actin filaments and vinculin protein.

MWCNT and SWCNT scaffolds, respectively. The vinculin protein appears to be co-localized with actin filaments and evenly distributed throughout the cytoplasm (Figure 27 C, F, I).

3.3.4.2 Cell proliferation (Ki-67 - cell proliferation marker)

Ki-67 is an antigen expressed during the active phases of cell cycle (G1, S, G2 and mitosis) and absent during the G0 phase, therefore, it has been widely used as a marker of cell proliferation. Figure 28 shows representative confocal microscopy images of immunofluorescence staining for Ki-67 expression by MC3T3 cells cultured on PLGA (Figure 28 A-C), MWCNT (Figure 28 D-F) and SWCNT (Figure 28 G-I) scaffolds after 5 days. MC3T3 cells were stained with FITC-conjugated phalloidin for actin cytoskeleton (green fluorescence, Figure 28, Panel A) and fluorescently labeled antibodies for Ki-67 expression (red fluorescence, Figure 28, Panel B). Panel C in Figure 28 shows merged images for actin cytoskeleton and Ki-67 protein. Ki-67 expression can be observed throughout the cytoplasm and nucleus for cells seeded on PLGA (Figure 28 C and D), MWCNT (Figure 28 E and F) and SWCNT (Figure 28 H and I) scaffolds implying that MC3T3 cells on all scaffold groups were metabolically active and proliferating.

3.3.5 Cell attachment and morphology (SEM)

SEM was used for the characterization of cellular adhesion and morphology. Figure 29 shows representative SEM images of MC3T3 cells on PLGA (Figure 29 A, D), MWCNT (Figure 29 B, E) and SWCNT (Figure 29 C, F) scaffolds after 5 days. The cells appear horizontally spread out on PLGA and MWCNT scaffolds, and rounded on SWCNT scaffolds (black arrows, Figure 29 D, E, and F, respectively). Cells on all the scaffolds show morphology that suggest formation of cytoplasmic extensions and membrane

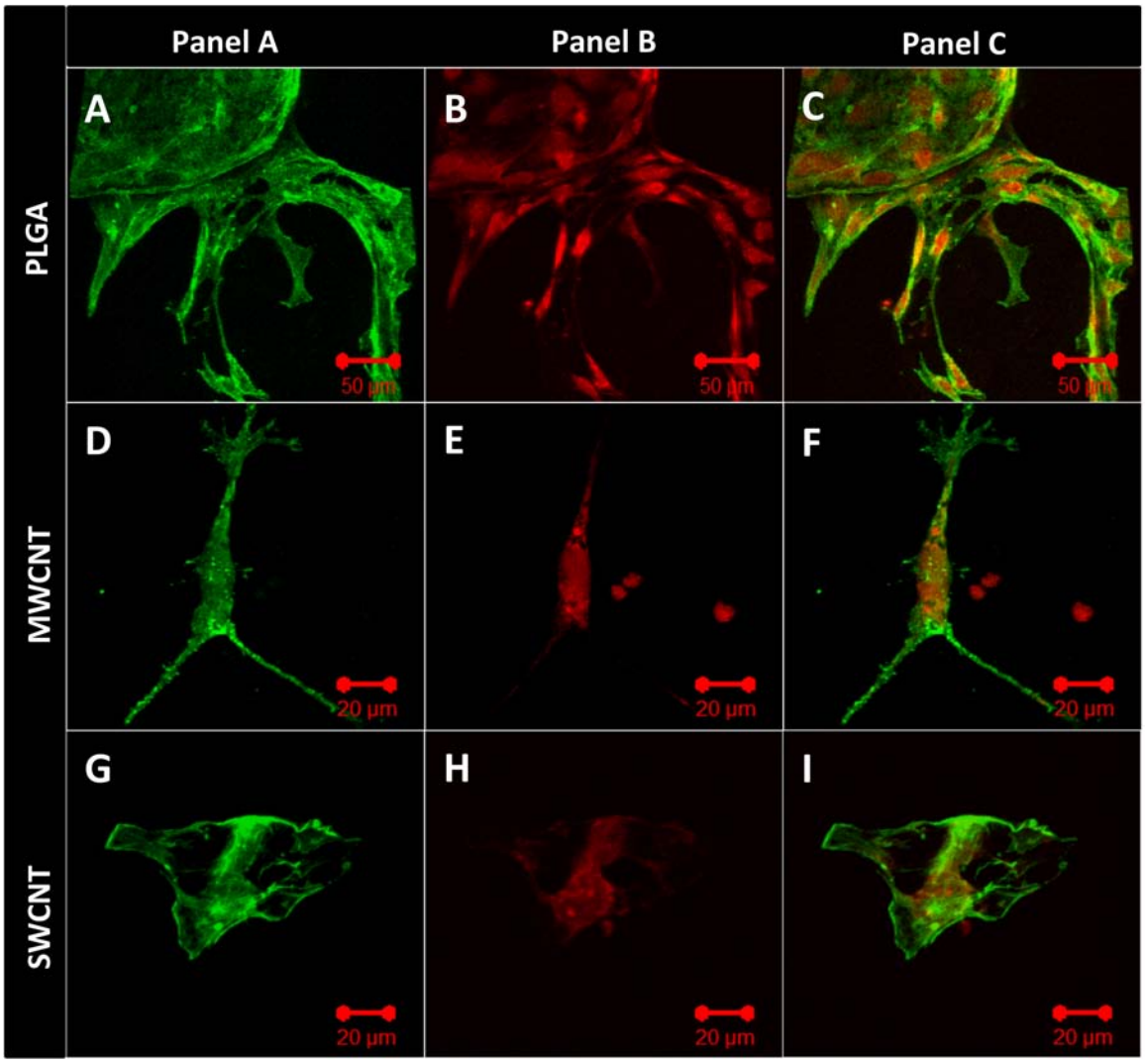

Figure 28: Representative immunofluorescence images of MC3T3 cells cultured on (A-C) poly(lactic-co-glycolic) acid, (D-F) multi walled carbon nanotube and (G-I) single walled carbon nanotube scaffolds after 5 days stained green for actin cytoskeleton (Panel A) and red for cell proliferation marker, i.e. Ki-67 protein (Panel B). Panel C shows superimposed images of panels A and B showing the co-localization of actin filaments and Ki-67 protein.

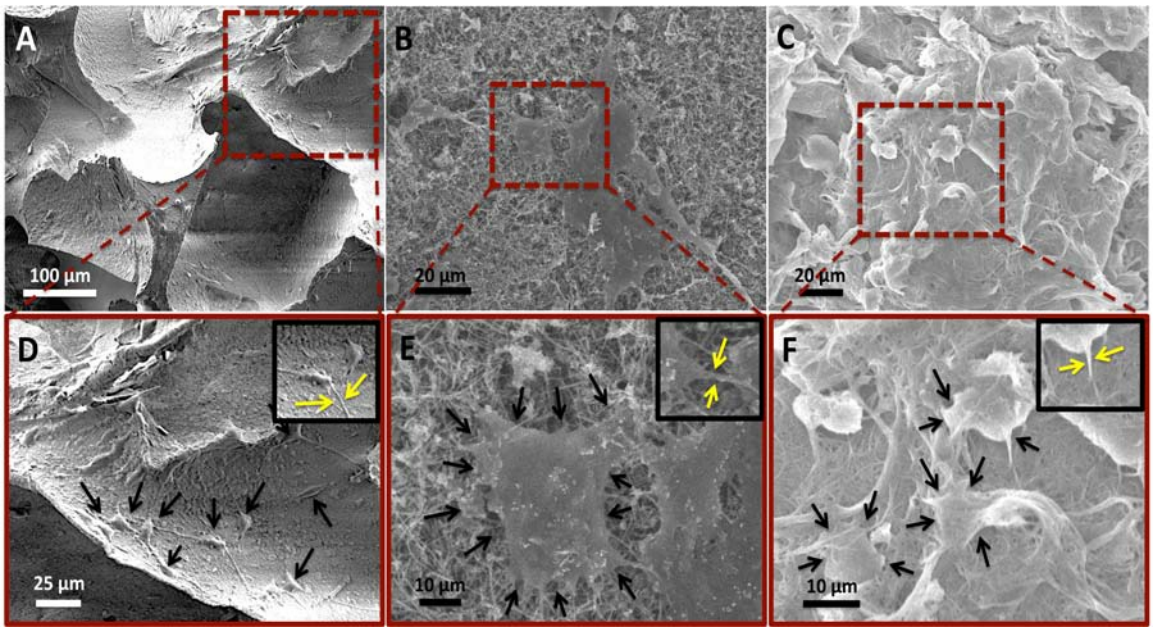

Figure 29: Representative SEM images showing adhesion of MC3T3 cells on (A and D) poly(lactic-co-glycolic) acid, (B and E) multi walled carbon nanotube, and (C and F) single walled carbon nanotube scaffolds. Formation of cytoplasmic extensions (filopodia and pseudopodia) can be observed for each scaffold group (inset in images D, E and F).

projections with no preferential direction (yellow arrows, inset, Figure 29 D, E, and F). Cells appear more elongated on MWCNT scaffolds and rounded on SWCNT scaffolds (Figure 29 E and F). Additionally, several nanoscale junctions between cell protrusions and underlying MWCNT and SWCNT networks can be observed (black arrows, Figure 29 E and F). The cytoplasmic protrusions appear to be wrapped over and under the MWCNT and SWCNTs bundles (Figure 29 G and H).

3.3.6 Image processing to assess cellular infiltration

Cellular infiltration inside PLGA, MWCNT and SWCNT scaffolds was assessed by image processing of Z-stacks of calcein-AM stained MC3T3 cells. Each individual stack was subjected to spectral-color coding steps to false color-code the cells as a function of

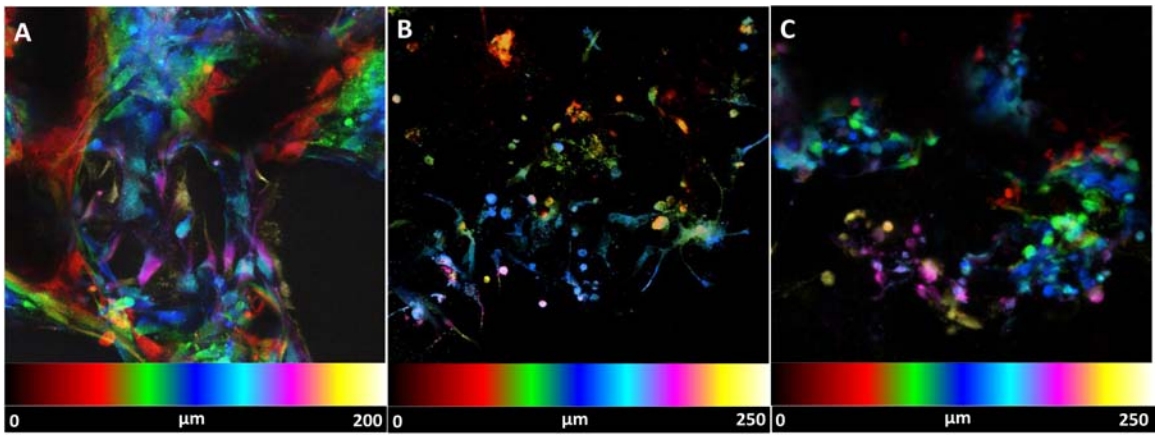

Figure 30: Representative spectrally color coded images of calcein-AM stained MC3T3 cells a function of confocal Z-depth (i.e. cellular infiltration) after 5 days of culture on (A) poly(lactic-co-glycolic) acid, (B) multi walled carbon nanotube and (C) single walled carbon nanotube scaffolds. Presence of cells can be detected upto a depth of ~200-300 µm for each scaffold group.

Z-depth i.e. cellular infiltration. Figure 30 A, B, and C show infiltration of cells on PLGA, MWCNT and SWCNT scaffolds, respectively. Presence of cells can be detected upto a depth of ~200-300 µm for each scaffold group. Image acquisition beyond that depth was not possible due to limitations with laser penetration inside 3D scaffolds.

3.4 Discussions

The goal of this study was to fabricate and assess the cytocompatibility of 3D, macro-sized, porous all-carbon scaffolds fabricated using MWCNTs and SWCNTs as building blocks. The porous cylindrical architecture of PLGA, MWCNT and SWCNT scaffolds is shown in Figure 22. MWCNT and SWCNT were assembled into 3D scaffolds using a radical initiated thermal crosslinking method as reported previously [41]. MWCNTs and SWCNTs were mixed with BP (nanomaterial:BP = 1:0.5) and a few drops of $CHCl_3$ and subjected to bath sonication for 15 minutes, poured into custom machined Teflon® molds, and incubated at 60°C for 24 hours. BP is a widely used radical initiator for free-

radical polymerization reactions and has been used for sidewall functionalization of carbon nanotubes [47]. Our previous study postulates the decomposition of BP to yield benzoyl and benzoyloxyl free radical species that attack the C=C double bonds on carbon nanotubes forming reactive sites [41]. These reactive sites serve as inter-nanotube crosslinking centers, resulting in the nanoscale crosslinking of carbon nanotubes, forming a 3D macroscopic architecture [41]. The unreacted BP and other volatile compounds get removed during the purification step (repeated washing steps with $CHCl_3$ and thermal annealing at 150°C for 30 minutes) [41]. The nanomaterial:BP ratio of 1:0.5 was used to fabricate scaffolds with >80% porosity. PLGA scaffolds with ~85% porosity were fabricated using a thermal crosslinking particulate leaching and were used as positive controls.

Chemical characterization of CNT scaffolds using Raman spectroscopy and X-ray photoelectron spectroscopy (XPS) has been reported in our previous study [41]. Those results determined the chemical composition of CNT scaffolds to comprise of carbon and oxygen as the primary elements (94.1% and 5.54% respectively). Further, it was also confirmed that the radical initiated crosslinking of CNTs is due to the disruption of sp^2 bonded C=C bonds, and also indicated presence of carbonyl, phenyl, and benzoyloxyl functional groups formed during the crosslinking reaction, the π–π interactions between aromatic groups of CNT and phenyl and benzoyloxyl adducts, and the presence of termination by-products of the radical initiated crosslinking reaction. Additionally, those results indicated that during thermal annealing steps, the functional groups, excess BP,

and radical by-products are removed resulting in the partial restoration of sp^2 (C=C) bonds.

The radical initiated thermal crosslinking method introduces the formation of nanoscale crosslinks between individual and bundled carbon nanotubes (analyzed by high-resolution SEM and TEM) [41]. SEM was performed on PLGA, MWCNT and SWCNT scaffolds (Figure 23) to characterize the morphology and pore architecture of scaffolds and re-confirm the presence of crosslinks between individual MWCNTs and SWCNTs (yellow arrows, Figures 23 B and C). Furthermore, the irregularly shaped macro-, micro-, and nano- scale pores of MWCNT and SWCNT scaffolds can be clearly noticeable (Figure 23 A and B). The pores of PLGA scaffolds are formed due to salt leaching and resemble the characteristic cubic shape of NaCl crystals (Figure 23 C).

MicroCT was used to characterize the porosity and pore sizes of PLGA, MWCNT and SWCNT scaffolds, whereas SEM image processing was used only for MWCNT and SWCNT scaffolds. MicroCT is a well-established method to characterize the porosity of polymeric and 3D all-carbon scaffolds [41, 48]. Figure 24 A-C shows the 3D reconstruction of cylindrical sections (1 mm^2 area, 0.5 mm height) of PLGA, MWCNT and SWCNT scaffolds, respectively. These images clearly confirm the presence of interconnected pores (blue colored voids) in all the scaffolds. The analysis of microCT sections confirms the presence of irregularly shaped interconnected pores, consistently distributed throughout the scaffold. It should be noted that the white and grey solid

interconnect structures in Figures 24 B and C possess nanoscale pores that cannot be visualized by microCT due to a resolution of 6 μm. These pores are clearly visualized by SEM imaging (Figure 23 B and C). To further characterize the nano- and micro-scale porosity of MWCNT and SWCNT scaffolds, SEM image processing was used. The porosity values determined using this method correspond to surface porosities and have been used to estimate porosities of tissue engineering scaffolds [43, 44]. SEM image analysis confirms the macroporous architecture of MWCNT and SWCNT scaffolds and the presence of nano- and micro- scaled interconnected pores. The presence of interconnected macroporous architecture is critical for efficient mass transport (diffusion of nutrients and removal of waste metabolites) and formation of neo-vasculature in the scaffolds upon implantation *in vivo*. MicroCT and SEM image processing results suggest that 3D, macroporous, MWCNT and SWCNT scaffolds may permit efficient mass transfer and neovascularization due to presence of interconnected nano-, micro-, and macro-scaled porosity.

Comprehensive *in vivo* cytotoxicity studies are the necessary first step towards more elaborate and costly *in vivo* studies that focus on assessing the biocompatibility of 3D MWCNT and SWCNT scaffolds for potential biomedical applications. Since the 3D macroporous MWCNT and SWCNT scaffolds could be utilized as implants for bone tissue engineering applications, they will primarily interact with precursor osteoblasts cells *in vivo*. Thus, MC3T3 cells, a widely accepted cell line for *in vitro* bone studies were utilized as model cell lines to evaluate the *in vitro* cytocompatibility of MWCNT and SWCNT scaffolds [49].

To quantitatively assess the cytotoxicity of MWCNT and SWCNT scaffolds, we performed LDH assay to assess cell death of MC3T3 cells after 1, 3, and 5 days of culture. Porous PLGA scaffolds were used as live controls. LDH assay is a widely recommended method to analyze the cytotoxicity of carbon nanomaterials [50]. It is well known that several cytotoxicity assays (such as MTT, XTT) produce erroneous results due to strong binding of formazan crystals on the nanotube surface [50]. Conversely, LDH assay measures the amount of cytosolic enzyme lactate dehydrogenase released in the media by apoptotic and necrotic cells therefore no interference is observed. We had previously validated the suitability of LDH assay of cytotoxicity studies involving carbon nanoparticles including nanotubes [14, 19, 51]. No significant difference in the total LDH release was observed between PLGA, MWCNT and SWCNT scaffold groups at days 3 and 5, suggesting a good cytocompatibility of MWCNT and SWCNT scaffolds, comparable to the FDA approved PLGA. To further analyze cell viability and corroborate LDH results, we performed calcein-AM staining of MC3T3 cells cultured on PLGA, MWCNT and SWCNT scaffolds after day 5. The bright green fluorescence observed in Figure 26 A-I confirms the presence of live MC3T3 cells on all scaffold groups at each time point. Furthermore, an increase in cell number can be observed between 1-5 days for all scaffolds suggesting that MC3T3 cells can proliferate on MWCNT and SWCNT scaffolds. It should be noted that Figure 26 A-I shows representative images; similar cell proliferation was observed for at least 3 individual experiments.

Immunofluorescence staining of MC3T3 cells was performed for vinculin (focal adhesion assembly) and Ki-67 (cell proliferation marker) expression to qualitatively confirm cell attachment and proliferation. Cell attachment is critical for adequate functioning of several cellular processes such as cell signaling, migration, maturation, apoptosis etc. [52]. Cells attach to the underlying extracellular matrix (ECM) by the formation of large macromolecular assemblies such as focal adhesion that connect ECM to actin filaments and hemidesmosomes that connect ECM to intermediate filaments. In mammalian cells, vinculin is a membrane cytoskeletal protein in focal adhesion complexes that link integrin molecules to actin cytoskeleton [46, 52]. Figure 27 confirms the expression of vinculin (red fluorescence), evenly distributed throughout the cytoplasm (green fluorescence), suggesting that MC3T3 cells form focal adhesion complexes with the underlying MWCNT and SWCNT networks. Ki-67 is a cell proliferation marker, expressed during all active phases of cell division (G1, S, G2 and M) and absent during the resting phase (G0) [53]. Therefore, Ki-67 has been extensively used as a marker of cell proliferation. MC3T3 cells on MWCNT and SWCNT scaffolds express Ki-67 protein (red fluorescence, Figure 28) suggesting proliferation of cells on MWCNT and SWCNT scaffolds. The expression of Ki-67 also provided further evidence that MC3T3 cells on these scaffolds are metabolically active.

Cellular infiltration into 3D scaffolds is important for tissue regeneration. Mierke et. al. have shown that expression of vinculin is critical for cellular infiltration into 3D scaffolds [54]. In our study, expression of vinculin by MC3T3 cells on MWCNT and SWCNT scaffolds suggests that these scaffolds are capable of supporting cellular infiltration into

3D architecture. It is well known that cell infiltration in 3D scaffolds and cell migration on 2D substrates is governed by different mechanisms[46, 54], and variable spatial expression of vinculin is observed for cells cultured on 2D vs. 3D substrates [46]. For example, vinculin and focal adhesion assemblies of cells on 2D planar substrates are aggregated towards the periphery of the cytoplasm. However, Fraley et. al. and others suggest that contrary to cells on 2D substrates, focal adhesion complexes of cells in 3D scaffolds are diffusely distributed throughout the cytoplasm [46, 55]. For cells embedded in a 3D matrix, cytoplasmic extensions and filopodia have a central role in driving cell motility; organized focal adhesions are short lived and small, compared to the lifetime and length of pseudopodia or amplitude and time scale of matrix deformation [46]. SEM analysis (Figure 29) of cells on PLGA, MWCNT and SWCNT scaffolds show the presence of numerous cytoplasmic extensions and filopodia (yellow arrows, inset, Figure 29 D, E and F). Migrating cells have also been reported to express cytoplasmic distribution of vinculin [55]. MC3T3 cells on MWCNT and SWCNT scaffolds show numerous filopodia and pseudopodia and a cytoplasmic distribution of vinculin suggesting that 3D MWCNT and SWCNT scaffolds permit cellular infiltration, critical for tissue regeneration. The spectrally color coded images of MC3T3 cells on MWCNT and SWCNT scaffolds (Figure 30) confirm cellular infiltration upto a depth of ~300 μm. However, cells maybe present at greater depths inside MWCNT and SWCNT scaffolds. Image acquisition at greater depths inside the 3D architecture of scaffolds was not possible due to limitations associated with the depth of penetration of the laser.

The elongated, spindle like morphology of MC3T3 cells on MWCNT scaffolds (Figure 26 F, 8 B) and circular rounded morphology on SWCNT scaffolds (Figure 26 I, 8 C) may be attributed to the differences in surface roughness, wherein, MWCNT scaffolds with higher surface roughness and greater nanotube diameter may result in the formation of largely spaced protein-adsorbed MWCNT islands/bundles. These results suggest that nanotopography of MWCNT and SWCNT scaffolds may control/alter cellular behavior. It is well known that nanotopography plays an important role in regulating cellular functions such as cell attachment, proliferation, migration and differentiation, thereby directly influencing metastasis, wound repair and embryogenesis [3, 34, 45]. Tutak et.al. observed increased adhesion of MC3T3 cells on hydrophilic carbon nanotube films with 100 nm surface roughness compared to films with ~60 nm surface roughness [32]. Oh et. al. demonstrated accelerated differentiation of human mesenchymal stem cells (hMSCs) on TiO_2 nanotubes with increasing nanotube diameter [56]. Dulgar-Tulloch et. al. cultured hMSCs on ceramics with varying grain sizes (24-1500 nm) and showed that 200 nm grain size was most favorable for hMSC proliferation [57]. In another study, Dalby et. al. showed enhanced bone cell differentiation on randomly ordered poly(methyl methacrylate) nanopits [58]. Nayak et. al. showed enhanced proliferation and differentiation of hMSCs on rough, graphene coated SiO_2 substrates and glass slide, compared to their non-graphene deposited counterparts [36]. Although the intricate details of how nanotopography affects cell fate is unknown, these reports suggest that increased nanotopography and surface roughness may result in increased protein adsorption, which in turn can govern cell fate. Based on our results and other reports, we hypothesize that, in order to bind to succeeding MWCNT bundles, cells will stretch and

elongate to a greater extent compared to cells binding to closely spaced SWCNT bundles due to small diameter of SWCNTs resulting in a significantly higher cytoplasmic elongation of cells cultured on rough MWCNT scaffolds compared to cells cultured on smooth SWCNT scaffolds. These results coupled with the ability to fine tune surface roughness of 3D carbon nanotube scaffolds by using nanotubes of varying diameters suggest that 3D all-carbon scaffolds may be exploited to control/govern cell fate purely based on nanotopographic cues. In addition, nanostructured scaffolds offer several advantages over conventional polymeric scaffolds such as (1) a single cell can contact millions of nanofibers (for example MWCNTs and SWCNTs), thereby resulting in the effective transmission of subtle topographic cues from the underlying scaffold substrate to the cell and (2) nanotopography and surface roughness of MWCNT and SWCNT scaffolds may result in a better host-implant integration reducing the risk of failure of biomedical implants [59].

To the best of our knowledge, this is the first study on the comprehensive assessment of cytocompatibility (cell viability, adhesion, proliferation and infiltration) of 3D macro-sized (>1mm in all three dimensions) all-carbon scaffolds with macro-, micro- and nano-porosity fabricated by radical initiated thermal crosslinking using MWCNT and SWCNT as building blocks. The results of this study suggest that 3D, all-carbon; MWCNT and SWCNT scaffolds are cytocompatible and opens avenues for further *in vivo* investigation of these scaffolds for biomedical applications. The assembly of carbon nanomaterials into various 3D, macroscopic, porous architectures is necessary to harness the unique physiochemical properties for the fabrication of next-generation of biomedical devices

and implants. Apart from the 2D films and 3D foams fabricated using the methods (vacuum filtration, CVD and sacrificial template-transfer) described in the introduction, over the last decade, microscopic 3-D carbon nanotube architectures of either aligned or entangled carbon nanotubes have been fabricated [60-62]. Macroscopic scale (>1mm in two or all three dimensions) structures of vertically aligned or entangled networks of pristine CNTs or graphene have also been fabricated using sol-gel reactions and powder-compression approaches [28, 63]. However, the ability of these methods to control the porosity of the 3-D CNT structures or to form covalent bonds between CNTs, an important feature for many biomedical applications, still needs to be determined. Furthermore, the use of toxic surfactants may adversely affect the cytocompatibility of these 3D structures, and the absence of macroporosity (pore size range: 10-200 μm, critical for cellular infiltration and exchange of metabolites), could restrict the suitability of these structures as scaffolds for biomedical applications. Typically, carbon nanomaterial dispersed polymeric scaffolds have been investigated for biomedical applications [9, 48, 64-66], however, compared to these composite architectures, 3D all-carbon scaffolds may possess additional multifunctional attributes. The chemical, physical and electrical properties of these 3D CNT scaffolds could be exploited to develop stimulus responsive scaffolds to deliver drugs[19, 20], electroceuticals applications[67], non-invasively image the scaffolds to track tissue regeneration[68] and control the fate of progenitor cells [17, 18]. Therefore, in a true-sense, 3D macroporous all-carbon scaffolds may be exploited as multifunctional scaffolds for the next generation of tissue engineering and regenerative medicine applications.

3.5 Conclusions

3D macroporous all-carbon scaffolds were fabricated using single- and multi-walled carbon nanotubes as building blocks. The 3D SWCNT and MWCNT scaffolds are macroporous architectures containing nano-, micro- and macro-scaled interconnected pores. The scaffolds show good cell viability, attachment, proliferation and cell infiltration. Differences in cell morphology were observed; cells on MWCNT scaffolds were elongated whereas on SWCNT scaffolds were rounded suggesting that scaffold nanotopography may be modulated to control cell morphology. These results taken together suggest that 3D macroporous all-carbon scaffolds fabricated using SWCNT and MWCNTs are cytocompatible and opens avenues for further *in vivo* investigation of these structures as multifunctional scaffolds for tissue engineering and regenerative medicine applications.

3.6 Tables

Table 9: Porosity, pore sizes and surface roughness of PLGA, MWCNT and SWCNT scaffolds

Scaffolds	Porosity		Pore sizes		Surface Roughness	
	MicroCT (%)	SEM Image Processing (%)	MicroCT (μm)	SEM Image Processing (nm)	Arithmetic (R_a, a.u.)	Mean (R_q, a.u.)
PLGA	86.61 ± 1.91	-	300-500	-	-	-
MWCNT	91.69 ± 1.43	45.82 ± 3.59%	100-400	45-850	137.19 ± 12.25	146.76 ± 12.29
SWCNT	83.79 ± 5.75	38.62 ± 2.91%	100-400	20-950	89.31 ± 16.05	105.07 ± 13.75

3.7 Acknowledgements

This work was supported by the National Institutes of Health (grant no. 1DP2OD007394-01). Research was carried out in part at the Center for Functional Nanomaterials, Brookhaven National Laboratory, New York, which is supported by the U.S. Department of Energy, Office of Basic Energy Sciences, under Contract No. DE-AC02-98CH10886.

3.8 References

[1] Discher DE, Mooney DJ, Zandstra PW. Growth factors, matrices, and forces combine and control stem cells. Science. 2009;324:1673-7.

[2] Engler AJ, Sen S, Sweeney HL, Discher DE. Matrix elasticity directs stem cell lineage specification. Cell. 2006;126:677-89.

[3] Dalby MJ, Gadegaard N, Oreffo RO. Harnessing nanotopography and integrin-matrix interactions to influence stem cell fate. Nature materials. 2014;13:558-69.

[4] Hui EE, Bhatia SN. Micromechanical control of cell-cell interactions. Proceedings of the National Academy of Sciences of the United States of America. 2007;104:5722-6.

[5] Peltola SM, Melchels FP, Grijpma DW, Kellomaki M. A review of rapid prototyping techniques for tissue engineering purposes. Annals of medicine. 2008;40:268-80.

[6] Nair LS, Bhattacharyya S, Laurencin CT. Development of novel tissue engineering scaffolds via electrospinning. Expert opinion on biological therapy. 2004;4:659-68.

[7] Deville S, Saiz E, Tomsia AP. Freeze casting of hydroxyapatite scaffolds for bone tissue engineering. Biomaterials. 2006;27:5480-9.

[8] Lu T, Li Y, Chen T. Techniques for fabrication and construction of three-dimensional scaffolds for tissue engineering. International journal of nanomedicine. 2013;8:337-50.

[9] Farshid B, Lalwani G, Sitharaman B. In Vitro Cytocompatibility of One- and Two-Dimensional Nanostructure-Reinforced Biodegradable Polymeric Nanocomposites. Journal of Biomedical Materials Research Part A. 2014:00A:000–000.

[10] Harris LD, Kim BS, Mooney DJ. Open pore biodegradable matrices formed with gas foaming. Journal of biomedical materials research. 1998;42:396-402.

[11] Gunatillake PA, Adhikari R. Biodegradable synthetic polymers for tissue engineering. Eur Cell Mater. 2003;5:1-16.

[12] Langer R, Vacanti JP. Tissue engineering. Science. 1993;260:920-6.

[13] Barnes CP, Sell SA, Boland ED, Simpson DG, Bowlin GL. Nanofiber technology: designing the next generation of tissue engineering scaffolds. Advanced drug delivery reviews. 2007;59:1413-33.

[14] Lalwani G, Sundararaj JL, Schaefer K, Button T, Sitharaman B. Synthesis, characterization, in vitro phantom imaging, and cytotoxicity of a novel graphene-based

multimodal magnetic resonance imaging-X-ray computed tomography contrast agent. Journal of Materials Chemistry B. 2014;2:3519-30.

[15] Kanakia S, Toussaint JD, Chowdhury SM, Lalwani G, Tembulkar T, Button T, et al. Physicochemical characterization of a novel graphene-based magnetic resonance imaging contrast agent. International journal of nanomedicine. 2013;8:2821-33.

[16] Lalwani G, Cai X, Nie L, Wang LV, Sitharaman B. Graphene-based contrast agents for photoacoustic and thermoacoustic tomography. Photoacoustics. 2013;1:62-7.

[17] Sitharaman B, Avti PK, Schaefer K, Talukdar Y, Longtin JP. A novel nanoparticle-enhanced photoacoustic stimulus for bone tissue engineering. Tissue engineering Part A. 2011;17:1851-8.

[18] Green DE, Longtin JP, Sitharaman B. The effect of nanoparticle-enhanced photoacoustic stimulation on multipotent marrow stromal cells. ACS nano. 2009;3:2065-72.

[19] Mullick Chowdhury S, Lalwani G, Zhang K, Yang JY, Neville K, Sitharaman B. Cell specific cytotoxicity and uptake of graphene nanoribbons. Biomaterials. 2013;34:283-93.

[20] Sun X, Liu Z, Welsher K, Robinson JT, Goodwin A, Zaric S, et al. Nano-Graphene Oxide for Cellular Imaging and Drug Delivery. Nano research. 2008;1:203-12.

[21] Lalwani G, Sitharaman B. Multifunctional Fullerene- and Metallofullerene-Based Nanobiomaterials. Nano LIFE. 2013;03:1342003.

[22] Tian B, Wang C, Zhang S, Feng L, Liu Z. Photothermally enhanced photodynamic therapy delivered by nano-graphene oxide. ACS nano. 2011;5:7000-9.

[23] Lalwani G, Henslee AM, Farshid B, Lin L, Kasper FK, Qin YX, et al. Two-dimensional nanostructure-reinforced biodegradable polymeric nanocomposites for bone tissue engineering. Biomacromolecules. 2013;14:900-9.

[24] Lalwani G, Henslee AM, Farshid B, Parmar P, Lin L, Qin YX, et al. Tungsten disulfide nanotubes reinforced biodegradable polymers for bone tissue engineering. Acta biomaterialia. 2013;9:8365-73.

[25] Talukdar Y, Avti P, Sun J, Sitharaman B. Multimodal ultrasound-photoacoustic imaging of tissue engineering scaffolds and blood oxygen saturation in and around the scaffolds. Tissue engineering Part C, Methods. 2014;20:440-9.

[26] Li N, Zhang Q, Gao S, Song Q, Huang R, Wang L, et al. Three-dimensional graphene foam as a biocompatible and conductive scaffold for neural stem cells. Scientific reports. 2013;3:1604.

[27] Crowder SW, Prasai D, Rath R, Balikov DA, Bae H, Bolotin KI, et al. Three-dimensional graphene foams promote osteogenic differentiation of human mesenchymal stem cells. Nanoscale. 2013;5:4171-6.

[28] Li X, Liu H, Niu X, Yu B, Fan Y, Feng Q, et al. The use of carbon nanotubes to induce osteogenic differentiation of human adipose-derived MSCs in vitro and ectopic bone formation in vivo. Biomaterials. 2012;33:4818-27.

[29] Mooney E, Mackle JN, Blond DJ, O'Cearbhaill E, Shaw G, Blau WJ, et al. The electrical stimulation of carbon nanotubes to provide a cardiomimetic cue to MSCs. Biomaterials. 2012;33:6132-9.

[30] Nayak TR, Jian L, Phua LC, Ho HK, Ren Y, Pastorin G. Thin films of functionalized multiwalled carbon nanotubes as suitable scaffold materials for stem cells proliferation and bone formation. ACS nano. 2010;4:7717-25.

[31] Jan E, Kotov NA. Successful differentiation of mouse neural stem cells on layer-by-layer assembled single-walled carbon nanotube composite. Nano letters. 2007;7:1123-8.

[32] Tutak W, Chhowalla M, Sesti F. The chemical and physical characteristics of single-walled carbon nanotube film impact on osteoblastic cell response. Nanotechnology. 2010;21:315102.

[33] Nardecchia S, Serrano MC, Gutiérrez MC, Ferrer ML, del Monte F. Modulating the cytocompatibility of tridimensional carbon nanotube-based scaffolds. Journal of Materials Chemistry B. 2013;1:3064-72.

[34] Brunner EW, Jurewicz I, Heister E, Fahimi A, Bo C, Sear RP, et al. Growth and proliferation of human embryonic stem cells on fully synthetic scaffolds based on carbon nanotubes. ACS applied materials & interfaces. 2014;6:2598-603.

[35] Park SY, Park J, Sim SH, Sung MG, Kim KS, Hong BH, et al. Enhanced differentiation of human neural stem cells into neurons on graphene. Advanced materials. 2011;23:H263-7.

[36] Nayak TR, Andersen H, Makam VS, Khaw C, Bae S, Xu X, et al. Graphene for controlled and accelerated osteogenic differentiation of human mesenchymal stem cells. ACS nano. 2011;5:4670-8.

[37] Tang M, Song Q, Li N, Jiang Z, Huang R, Cheng G. Enhancement of electrical signaling in neural networks on graphene films. Biomaterials. 2013;34:6402-11.

[38] Martinelli V, Cellot G, Fabbro A, Bosi S, Mestroni L, Ballerini L. Improving cardiac myocytes performance by carbon nanotubes platforms. Frontiers in physiology. 2013;4:239.

[39] Reina A, Jia X, Ho J, Nezich D, Son H, Bulovic V, et al. Large area, few-layer graphene films on arbitrary substrates by chemical vapor deposition. Nano letters. 2008;9:30-5.

[40] Patel SC, Lalwani G, Sitharaman B. Fabrication and Cytocompatibility of in situ crosslinked carbon nanomaterial films. ACS Appl Mater Interfaces - In Review. 2014.

[41] Lalwani G, Kwaczala AT, Kanakia S, Patel SC, Judex S, Sitharaman B. Fabrication and Characterization of Three-Dimensional Macroscopic All-Carbon Scaffolds. Carbon. 2013;53:90-100.

[42] Cai X, Paratala BS, Hu S, Sitharaman B, Wang LV. Multiscale photoacoustic microscopy of single-walled carbon nanotube-incorporated tissue engineering scaffolds. Tissue engineering Part C, Methods. 2012;18:310-7.

[43] Guarino V, Guaccio A, Netti PA, Ambrosio L. Image processing and fractal box counting: user-assisted method for multi-scale porous scaffold characterization. Journal of materials science Materials in medicine. 2010;21:3109-18.

[44] McCullen SD, Stevens DR, Roberts WA, Clarke LI, Bernacki SH, Gorga RE, et al. Characterization of electrospun nanocomposite scaffolds and biocompatibility with adipose-derived human mesenchymal stem cells. International journal of nanomedicine. 2007;2:253-63.

[45] Kim DH, Provenzano PP, Smith CL, Levchenko A. Matrix nanotopography as a regulator of cell function. The Journal of cell biology. 2012;197:351-60.

[46] Fraley SI, Feng Y, Krishnamurthy R, Kim DH, Celedon A, Longmore GD, et al. A distinctive role for focal adhesion proteins in three-dimensional cell motility. Nature cell biology. 2010;12:598-604.

[47] Peng H, Reverdy P, Khabashesku VN, Margrave JL. Sidewall functionalization of single-walled carbon nanotubes with organic peroxides. Chemical communications. 2003:362-3.

[48] Shi X, Sitharaman B, Pham QP, Liang F, Wu K, Edward Billups W, et al. Fabrication of porous ultra-short single-walled carbon nanotube nanocomposite scaffolds for bone tissue engineering. Biomaterials. 2007;28:4078-90.

[49] Wang K, Cai L, Jesse S, Wang S. Poly (ε-caprolactone)-Banded Spherulites and Interaction with MC3T3-E1 Cells. Langmuir. 2012;28:4382-95.

[50] Worle-Knirsch JM, Pulskamp K, Krug HF. Oops they did it again! Carbon nanotubes hoax scientists in viability assays. Nano letters. 2006;6:1261-8.

[51] Avti PK, Caparelli ED, Sitharaman B. Cytotoxicity, cytocompatibility, cell-labeling efficiency, and in vitro cellular magnetic resonance imaging of gadolinium-catalyzed single-walled carbon nanotubes. Journal of biomedical materials research Part A. 2013;101:3580-91.

[52] Demali KA. Vinculin--a dynamic regulator of cell adhesion. Trends in biochemical sciences. 2004;29:565-7.

[53] Scholzen T, Gerdes J. The Ki-67 protein: from the known and the unknown. Journal of cellular physiology. 2000;182:311-22.

[54] Mierke CT, Kollmannsberger P, Zitterbart DP, Diez G, Koch TM, Marg S, et al. Vinculin facilitates cell invasion into three-dimensional collagen matrices. The Journal of biological chemistry. 2010;285:13121-30.

[55] Van Tam JK, Uto K, Ebara M, Pagliari S, Forte G, Aoyagi T. Mesenchymal stem cell adhesion but not plasticity is affected by high substrate stiffness. Science and Technology of Advanced Materials. 2012;13:064205.

[56] Oh S, Brammer KS, Li YS, Teng D, Engler AJ, Chien S, et al. Stem cell fate dictated solely by altered nanotube dimension. Proceedings of the National Academy of Sciences of the United States of America. 2009;106:2130-5.

[57] Dulgar-Tulloch AJ, Bizios R, Siegel RW. Human mesenchymal stem cell adhesion and proliferation in response to ceramic chemistry and nanoscale topography. Journal of biomedical materials research Part A. 2009;90:586-94.

[58] Dalby MJ, Gadegaard N, Tare R, Andar A, Riehle MO, Herzyk P, et al. The control of human mesenchymal cell differentiation using nanoscale symmetry and disorder. Nature materials. 2007;6:997-1003.

[59] Tonelli FM, Santos AK, Gomes KN, Lorencon E, Guatimosim S, Ladeira LO, et al. Carbon nanotube interaction with extracellular matrix proteins producing scaffolds for tissue engineering. International journal of nanomedicine. 2012;7:4511-29.

[60] De Volder M, Tawfick SH, Park SJ, Copic D, Zhao Z, Lu W, et al. Diverse 3D microarchitectures made by capillary forming of carbon nanotubes. Advanced materials. 2010;22:4384-9.

[61] Chakrapani N, Wei B, Carrillo A, Ajayan PM, Kane RS. Capillarity-driven assembly of two-dimensional cellular carbon nanotube foams. Proceedings of the National Academy of Sciences of the United States of America. 2004;101:4009-12.

[62] Gui X, Wei J, Wang K, Cao A, Zhu H, Jia Y, et al. Carbon Nanotube Sponges. Advanced materials. 2010;22:617-21.

[63] Bryning MB, Milkie DE, Islam MF, Hough LA, Kikkawa JM, Yodh AG. Carbon Nanotube Aerogels. Advanced materials. 2007;19:661-4.

[64] Abarrategi A, Gutierrez MC, Moreno-Vicente C, Hortiguela MJ, Ramos V, Lopez-Lacomba JL, et al. Multiwall carbon nanotube scaffolds for tissue engineering purposes. Biomaterials. 2008;29:94-102.

[65] Nardecchia S, Serrano MC, Gutierrez MC, Ferrer ML, Monte Fd. Modulating the cytocompatibility of tridimensional carbon nanotube-based scaffolds. Journal of Materials Chemistry B. 2013;1:3064-72.

[66] Sitharaman B, Shi X, Walboomers XF, Liao H, Cuijpers V, Wilson LJ, et al. In vivo biocompatibility of ultra-short single-walled carbon nanotube/biodegradable polymer nanocomposites for bone tissue engineering. Bone. 2008;43:362-70.

[67] Famm K, Litt B, Tracey KJ, Boyden ES, Slaoui M. Drug discovery: A jump-start for electroceuticals. Nature. 2013;496:159-61.

[68] Pramanik M, Swierczewska M, Wang LV, Green D, Sitharaman B. Single-walled carbon nanotubes as a multimodal-thermoacoustic and photoacoustic-contrast agent. Journal of biomedical optics. 2009;14:034018--8.

Chapter 4

THREE DIMENSIONAL MACROSCOPIC ALL-CARBON SCAFFOLDS FOR STEM CELL MAINTENANCE AND EXPANSION

4.1 Introduction

Mesenchymal stem cells (MSCs) are multipotent non-hematopoietic stem cells present in the connective tissues of the body. MSCs are capable of direct multi-lineage differentiation into mesodermal cell lineages such as osteoblasts, adipocytes, chondrocytes, and connective stromal cells and trans-differentiation into ectodermal and endodermal cell types such as neurons and muscle cells (Figure 31).[1] MSCs show promise for several therapeutic applications including regenerative medicine, drug discovery, cellular therapy and disease modeling. Expansion of stem cells and maintenance of their self-renewal capacity *in vitro* requires specialized robust cell culture systems. Conventional approaches consisting of animal derived or artificial matrices and a cocktail of growth factors have several limitations such as consistency, scalability, and pathogenicity (risk of infection) [2]. The expansion of MSCs using 2D *in vitro* culture systems is associated with several phenotypic changes such as diminished proliferation and self-renewal capacity due to contact inhibition. Furthermore, to achieve high cell densities for practical therapeutic applications, 3D culture systems have been recommended over conventional 2D substrates [3-5]. To overcome the above limitations, multifunctional 3D porous scaffold, fabricated using synthetic materials that permit stem cell expansion and maintenance *in vitro* would constitute a significant advancement.

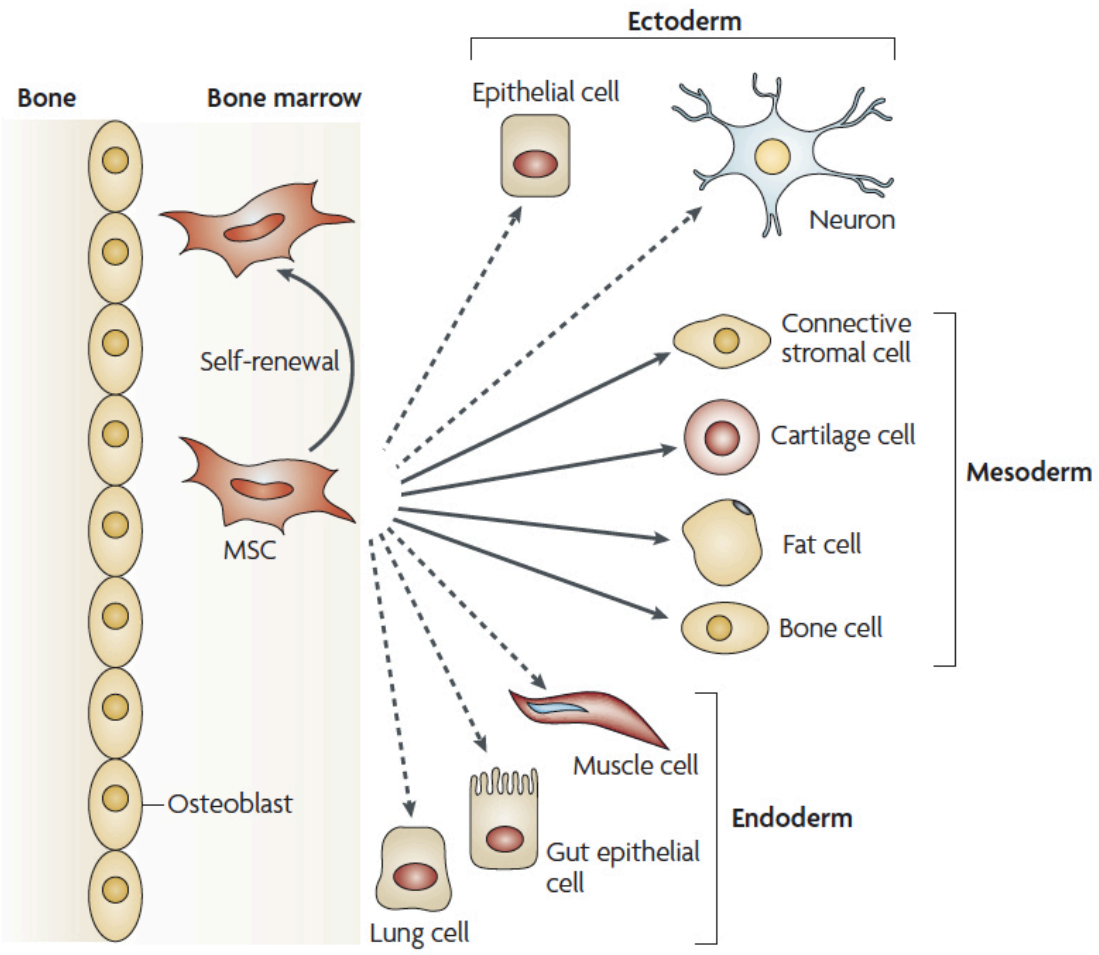

Figure 31:Schematic depicting the multipotency of mesenchymal stem cells. (MSCs). MSCs can self renew (curved arrow), undergo straight differentiation (solid arrows) towards mesodermal lineage or trans-differentiate towards ectodermal or endodermal cell types. Adapted from Reference 1 with permission. Copyright © Macmillan publishers limited, 2008.

Carbon nanomaterials such as carbon nanotubes (CNTs) and graphene have been assembled into 2D films (using vacuum filtration and chemical vapor deposition (CVD) methods) and 3D foams (using CVD and sacrificial template-transfer methods) and reported as cytocompatible substrates for proliferation and differentiation of stem cells for applications in bone, neuron and cardiac tissue engineering [2-5]. These methods of CNT assembly and scaffold fabrication have limitations such as substrate specificity, mechanical integrity and control over scaffold porosities. We have recently reported a

novel, economical and easy method to fabricate macroscopic, 3D, free standing, all-carbon scaffolds (macroporous architectures) by radical initiated thermal crosslinking and annealing of CNTs [1]. This method can fabricate macroporous (20 nm – 300 μm pore sizes) all-carbon structures with high porosities (~80-85%). Furthermore, porosity of scaffolds can be controlled by the amount of radical initiator used in the crosslinking process, thereby allowing the fabrication of porous all-carbon scaffolds tailored towards specific applications.

In this study, we investigated (1) the cell viability, attachment and proliferation of human ADSCs on single- and multi-walled carbon nanotube (SWCNT and MWCNT) scaffolds and (2) the plasticity or "stemness" of ADSCs after long-term culture on 3D SWCNT and MWCNT scaffolds according to the International Society for Cellular Therapy (ISCT) guidelines [6]. ADSCs after expansion on 3D SWCNT or MWCNT scaffolds were harvested and examined *in vitro* for (a) adherence to plastic (TCPS), (b) MSC surface antigen expression [CD14(-), CD19(-), CD34(-), CD45(-), CD73(+), CD90(+), CD105(+)] and (c) osteogenic, adipogenic and chondrogenic differentiation potential. Porous polymeric scaffolds prepared using the FDA approved biodegradable biocompatible polymer poly(lactic-co-glycolic acid) (PLGA) were used as controls.

4.2 Materials and methods

4.2.1 Fabrication and characterization of MWCNT, SWCNT and PLGA scaffolds

MWCNTs (Sigma–Aldrich, NY, USA), SWCNTs (CheapTubes Inc., NY, USA), PLGA (Polysciences Inc., PA, USA), benzoyl peroxide (BP, Sigma–Aldrich, NY, USA) and chloroform ($CHCl_3$, Fisher Scientific, PA, USA) were used as purchased. Porous PLGA scaffolds with ~ 85% porosity were fabricated using a thermal-crosslinking particulate leaching technique using NaCl as the porogen as described elsewhere [42]. MWCNT and SWCNT scaffolds were fabricated by mixing nanomaterials with BP at a mass ratio of MWCNT/SWCNT:BP = 1:0.05 as described previously (section 3.2.1). Characterization of MWCNT, SWCNT and PLGA scaffold morphology by SEM and porosities and pore architecture using microCT has been reported previously (see section 3.2.2 for SEM and 3.2.3 for microCT).

4.2.2 ADSC cell culture

Human adipose derive stem cells (ADSCs) were purchased from Lonza Walkersville Corp. (MD, USA). ADSCs were grown in Lonza's ADSC human Adipose Derived Stem Cell Growth BulletKit™ Medium containing 10 vol. % fetal bovine serum (FBS, Gibco Life Technologies, NY, USA) and 1 vol. % antibiotics (penicillin- streptomycin, Gibco Life Technologies, NY, USA). Media was changed twice a week, and cells were maintained at 37°C in a humidified environment of 5% CO_2-95% O_2. For

cytocompatibility studies, purified MWCNT and SWCNT scaffolds were prepared as described previously (section 3.2.5). Briefly, MWCNT and SWCNT scaffolds were washed with CHCl3 and placed in an oven at 110°C followed by a series of washes (3X) with CHCl3 (to remove residual BP) and a graded series of ethanol (100%-70%). PLGA scaffolds were only washed with graded series of ethanol, not CHCl3. The scaffolds (PLGA, MWCNT and SWCNT) were then subjected to UV sterilization for 24 hours followed by washes with phosphate buffered saline (PBS) and ADSC basal media. For pre-wetting, the scaffolds were incubated with blank cell culture media for 24 hours prior to cell seeding. ADSCs were trypsinized, resuspended in basal media, and seeded on the scaffolds at a density of 500,000 cells/scaffold in 30 µl media (added in 2 intervals of 15µl). Cells were allowed to attach on the scaffolds for 2 hours before addition of complete media (1 ml) to each well of the 24-well plate. The cells were cultured for 1, 3, 5, 15 and 30 days on the scaffolds.

4.2.3 Lactate dehydrogenase (LDH) assay

LDH assay was performed as described previously (section 3.2.6).[7] Briefly, after each time point (1, 3 and 5 days), 50 µl media was collected from each well of the 24-well plate (n=6 for each scaffold group) and transferred to a fresh 96-well plate. A total of 100 µl of LDH assay mixture was added to each well and incubated in dark for 45 minutes. To stop the reaction, 1N HCl (10% volume) was added to each well. Absorbance values were recorded using a 96 well plate reader (Molecular Devices, CA, USA) at 490 nm. Positive control cells (100% dead) were prepared by incubating ADSCs grown on tissue

culture polystyrene with lysis buffer for 45 minutes before centrifugation. Cells cultured on PLGA scaffolds served as the baseline control. Total LDH release (% of positive control) was expressed as the percentage of $(OD_{test} - OD_{blank})/(OD_{positive} - OD_{blank})$, where OD_{test} is the optical density of cells cultured on PLGA, MWCNT or SWCNT scaffolds, OD_{blank} is the optical density of 96-well plate without cells, and $OD_{positive}$ is the optical density of positive control (100% dead cells). Absorbance of blank culture media was measured for baseline correction.

4.2.4 Calcein-AM fluorescence imaging

Calcein-AM fluorescence imaging was performed as described previously (section 3.2.7). Briefly, after 1, 3, 5, 15, and 30 days, media was removed and scaffolds were washed with PBS. 1 ml of Calcein-AM dye (4μM) was added to each well and incubated at 37°C in dark for 20 minutes. The scaffolds were transferred to 35 mm glass bottom dishes (Mattek Corporation, Ashland, MA) and imaged by a confocal laser-scanning microscope (Zeiss LSM 510 Meta NLO Two-Photon) using Zeiss LSM Image Browser software (version 4.2, Carl Zeiss Microimaging, Thornwood, NJ).

4.2.5 Immunofluorescence for focal adhesion and cell proliferation

Immunofluorescence was performed as reported previously in section 3.2.8. Briefly, glutaraldehyde fixed cells on PLGA, MWCNT, and SWCNT scaffolds were washed with

PBS and incubated with 2% glycine for 5 minutes for blocking. The scaffolds were placed in 0.5% Triton-X-100 permeabilizing buffer (composition: 10.3 g sucrose, 0.29 g NaCl, 0.4 g Hepes buffer, 0.06 g $MgCl_2$, and 0.5 ml Triton-X-100 in 100 ml of DI water) for 25 minutes. Scaffolds were then washed with immunofluorescence buffer (IFB, 0.1% Triton-X-100 and 0.1% BSA in PBS) and incubated with commercially available monoclonal antibodies. Scaffolds were incubated for 1 hour with either anti-proliferating Ki-67 antibody ((2 µl/ml in IFB, Cat. No. P8825, Sigma Aldrich, New York, USA) for cell proliferation analysis or monoclonal anti-vinculin antibody (2 µl/ml in IFB, Cat. No. V4139, Sigma Aldrich, NY, USA) for visualization of focal adhesion sites. After 1 hour of incubation with primary antibodies, the scaffolds were washed with IFB (3X) and incubated with secondary antibody (anti-rabbit TRITC, 2 µl/ml in IFB, Cat. No. T6778, Sigma Aldrich, New York, USA) for 1 hour. Scaffolds were then washed with IFB (3X) and the cytoplasm was stained with FITC-conjugated phalloidin (2 µl/ml in PBS) for 1 hour to visualize actin filaments (cytoskeleton). Samples were imaged using a confocal laser-scanning microscope (Zeiss LSM 510 Meta NLO Two-Photon) equipped with Zeiss LSM Image Browser software (version 4.2, Carl Zeiss Microimaging, Thornwood, NJ).

4.2.6 SEM imaging for cell attachment

SEM imaging was performed as described previously in section 3.2.9. To visualize cell attachment on scaffolds, glutaraldehyde fixed cells on PLGA, MWCNT and SWCNT scaffolds were subjected to dehydration steps using graded ethanol washes (70%-100%), air dried, and vacuum dried for 24 hours. Scaffolds were then sputter coated with 3 nm of

silver (Ag) and imaged using a JOEL 7600F Analytical high resolution SEM (Center for Functional Nanomaterials, Brookhaven National Laboratory, New York) at an accelerating voltage of 2 kV.

4.2.7 Image processing to assess cellular infiltration

Z-stacks of calcein stained ADSCs on PLGA, MWCNT and SWCNT scaffolds were acquired using a confocal laser-scanning microscope (Zeiss LSM 510 Meta NLO Two-Photon). Individual Z-stacks were then imported to ImageJ (Bethesda, MD, USA) and subjected to spectral coding using a time-lapse color coder plugin to false-color each slice as a function of depth (Z height, i.e. depth of cellular infiltration). The multiple spectrally color-coded slices of Z-stacks were then compressed to form one composite image and reported.

4.2.8 Immunofluorescence for MSC phenotype analysis

MSC either express specific surface antigens that can be used as markers for identification of stem cell phenotype in a heterogenous population of cells. According to ISCT guidelines, MSCs are CD14(-), CD19(-), CD34(-), CD45(-), CD73(+), CD90(+) and CD105(+). Immunofluorescence was performed on ADSCs attached to PLGA, MWCNT or SWCNT scaffolds after 15 days of culture using a previously described protocol (section 4.2.5) with a few modifications. We used FITC conjugated monoclonal

antibodies specific to each surface antigen to assess the expression of MSC markers on ADSC cultured on PLGA, MWCNT and SWCNT scaffolds after 15 days. The cytoplasm was stained using Rhodamine phalloidin to visualize actin filaments (red fluorescence, Life Technologies, USA).

4.2.9 Adherence of harvested ADSCs to TCPS

According to ISCT guidelines, stem cells must be adherent to plastic when maintained in standard tissue culture conditions. After 30 days of culture on PLGA, MWCNT and SWCNT scaffolds, ADSCs were trypsinized from the scaffolds and expanded *in vitro* on 150 mm TCPS plates. The cells were cultured in ADSC basal growth media using standard tissue culture protocols as described in section 4.2.2.

4.2.10 Osteogenic differentiation

ADSCs harvested from PLGA, SWCNT and MWCNT scaffolds after 30 days of culture were used for differentiation studies. Additionally ADSCs grown on TCPS (not PLGA, SWCNT or MWCNT scaffolds) were used as controls. Osteogenic differentiation was performed using a standard procedure recommended by Lonza Corporation (MD, USA). Osteogenic induction media was prepared by mixing hMSC differentiation basal medium – osteogenic and SingleQuots™ factors (Dexamethasone, L-Glutamine, Ascorbate, Pen/Strep and MCGS) as supplied in the hMSC Osteogenic BulletKit (Catalog # PT-

3002, Lonza Corp., MD, USA). Initially, ADSCs were plated at a density of 10,000 cells per well in a 24 well plate and incubated in ADSC basal growth media for 24 hours at 37°C, 5% CO_2 and 90% humidity. After 24 hours, growth media was removed and 1 ml of osteogenic induction media was added to each well and replenished every 3-4 days. ADSCs were maintained in osteogenic induction media for 3 weeks. Alkaline phosphatase expression and alizarin red staining were used as markers for osteogenic differentiation.

4.2.10.1 Alkaline phosphatase (ALP) expression

The ALP activity of ADSCs after osteogenic differentiation was measured using a well-established protocol utilizing the conversion of substrate p-nitrophenylphosphate (pNPP) to p-nitrophenolate due to hydrolysis by ALP [8]. ADSCs were washed with PBS and lysed by sonication for 30 minutes. After sonication, 100 µl of pNPP were added to the cell lysate and incubated at 37 °C for 1 hour. The assay was run in triplicates in a 96 well plate. After incubation, 100 µl of NaOH was added to each well to stop the reaction and absorbance was measured at 405 nm using a plate reader (Molecular Devices, CA, USA). Data is presented as ALP activity in mmol per minute per cell.

4.2.10.2 Alizarin red staining

Alizarin red staining was performed to analyze osteodifferentiation of ADSCs using a well-established protocol as reported previously [9]. Alizarin Red S solution (40 mM) was prepared in DI water and the pH was adjusted to 4.1 using 1 N ammonium hydroxide solution. After incubation with osteogenic induction media for 3 weeks, ADSCs were washed with PBS (3x) and fixed using 4% paraformaldehyde solution for 15 min. ADSCs were then rinsed with DI water and incubated with 1 ml of Alizarin Red S solution for 20 minutes under gentle shaking. After 20 minutes of incubation, ADSCs were rinsed with DI water (4x) and imaged using a BX-51 Olympus microscope (Hamburg, Germany).

4.2.11 Adipogenic differentiation

Adipogenic differentiation was performed using a well-established procedure reported previously [10]. Briefly, mixing hMSC adipogenic induction medium (PT-3102B) and the following SingleQuots™ prepared adipogenic induction medium: h-insulin (recombinant), L-glutamine, MCGS, dexamethasone, indomethacin, IBMX (3-isobuty-l-methyl-xanthine) and GA-1000. Adipogenic maintenance medium was prepared by mixing hMSC adipogenic maintenance medium (PT-3102A) and the following SingleQuots™: h-insulin (recombinant), L-glutamine, MCGS and GA-1000. All components were purchased as hMSC Adipogenic BulletKit (Catalog number PT-3004, Lonza Corporation, MD, USA). ADSCs were plated at a cell density of 20,000 cells per ml in 24 well plates and incubated in ADSC basal growth media for 24 hours at 37°C, 5% CO_2 and 90% humidity. After incubation, ADSCs were subjected to three cycles of adipogenic induction/maintenance wherein each cycle consisted of culturing ADSCs in

adipogenic induction media for 3 days and adipogenic maintenance media for 3 days. After 3 cycles, ADSCs were maintained in adipogenic maintenance media for an additional 7 days. The cells were rinsed with PBS (3x), fixed using 4% paraformaldehyde for 20 minutes, and stained using Oil red O dye for characterization of triglycerides and esters as a marker for adipogenic differentiation.

4.2.11.1 Oil red O staining

Oil Red O stain was used for the staining of triglycerides and esters after adipogenic differentiation of ADSCs using a well-established protocol [11]. Paraformaldehyde fixed ADSCs were washed with 60% isopropanol solution and wells were left for drying at room temperature. 0.5 ml Oil Red O working solution - made with two parts Oil Red O stock solution (0.35% solution in isopropanol) and three parts isopropanol – was added to each well and incubated for 10 minutes. To remove excess Oil Red O dye, ADSCs were incubated with 1 ml of 100% isopropanol solution for 10 minutes and rinsed with DI water (4x). The cells were then imaged using a BX-51 Olympus microscope (Hamburg, Germany). ADSC harvested from PLGA, MWCNT and SWCNT scaffolds served as the experimental groups and ADSCs cultured on standard TCPS served as the control group.

4.2.12 Chondrogenic differentiation

Chondrogenic differentiation was performed according to the manufacturers protocol. Briefly, incomplete chondrogenic induction medium was prepared by mixing hMSC differentiation basal medium – chondrogenic and the following SingleQuots™: dexamethasone, ascorbate, ITS + supplement, GA-1000, sodium pyruvate, proline and L-glutamine. Complete chondrogenic media was prepared by adding TGF-β to incomplete chondrogenic media to achieve a final concentration of 10 ng/ml. ADSC were trypsinized and centrifuged (5000 rpm, 5 minutes) to obtain a cell pellet. The cell pellet was washed with incomplete chondrogenic media, centrifuged and resuspended in complete chondrogenic media. An aliquot of 2.5 x 10^5 cells were added to a 15 ml sterile poly(propylene) culture tubes with 1 ml complete chondrogenic media and centrifuged at 5000 rpm for 5 minutes to obtain a cell pellet. Caution was maintained not to disrupt the pellet throughout the differentiation study. The caps of the tubes were loosened by one half turn to facilitate gas exchange and the tubes were incubated at 37°C, 5% CO_2 and 90% humidity for 28 days with regular media changes every 2-3 days. After 28 days, the pellets were harvested, fixed with formalin and embedded in paraffin for histological sectioning.

4.2.12.2 Alcian blue staining

Paraffin embedded sections were baked at 60°C and deparaffinized using xylene (3 washes, 2 minutes each wash). The sections were rehydrated by washes with 100% ethanol (2x), 70% ethanol (2x) and tap water (~ 20 dips) and stained with Alcian blue solution for 15 minutes. Section were washed with running tap water for 5 minutes,

rinsed in DI water and counterstained with neutral red stain for 1 minute. The sections were then dehydrated in ethanol and mounted for imaging.

4.2.13 Statistical analysis

Data is reported as mean ± standard deviation. Statistical analysis was performed for a 95% confidence interval ($p < 0.05$) using students 't' test. To analyze the differences between the groups, one-way anova followed by Tukey Kramer post hoc analysis was performed.

4.3 Results

4.3.1 Fabrication and characterization of PLGA, MWCNT and SWCNT scaffolds

PLGA scaffolds were fabricated using a thermal crosslinking particulate leaching method as described previously [12]. 3D MWCNT and SWCNT scaffolds were fabricated using a radical initiated thermal crosslinking method using MWCNT and SWCNT as building blocks using a previously reported method [13]. Detailed characterization of scaffold morphology, architecture, porosity, pore sizes and surface roughness have been reported previously (see section 3.3.2). In this study, PLGA, MWCNT and SWCNT scaffolds of cylindrical morphology (~4 mm in height and 3-4 mm in diameter) with ~80-85%

porosity were used. The pore sizes of PLGA scaffolds were between 300-500 µm whereas MWCNT and SWCNT scaffolds had pore sizes between 20 nm - 400 µm.

4.3.2 Lactate dehydrogenase (LDH) assay

Lactate dehydrogenase is a cytosolic enzyme release in the culture media by apoptotic or necrotic cells. LDH assay quantified the amount of LDH released as a measure of cell death. The LDH present in the media catalyzes the conversion of lactate to pyruvate, in turn reducing NAD+ to NADH, which catalyzes the conversion of iodonitrotetrazolium present in the assay reagent (INT) to a water-soluble formazan product that can be quantified using an absorbance plate reader. Figure 32 shows the total LDH released (normalized to positive controls) from ADSCs after 1, 3, and 5 days of culture on PLGA, MWCNT and SWCNT scaffolds. Although ADSCs on SWCNT scaffolds show a slightly higher LDH release (~ 45%) compared to cells grown on TCPS (~ 33%) after day 1, no significant differences were observed between total LDH released by ADSCs cells on PLGA, MWCNT and SWCNT scaffolds at all time points (LDH release was between ~ 30-45% for all groups).

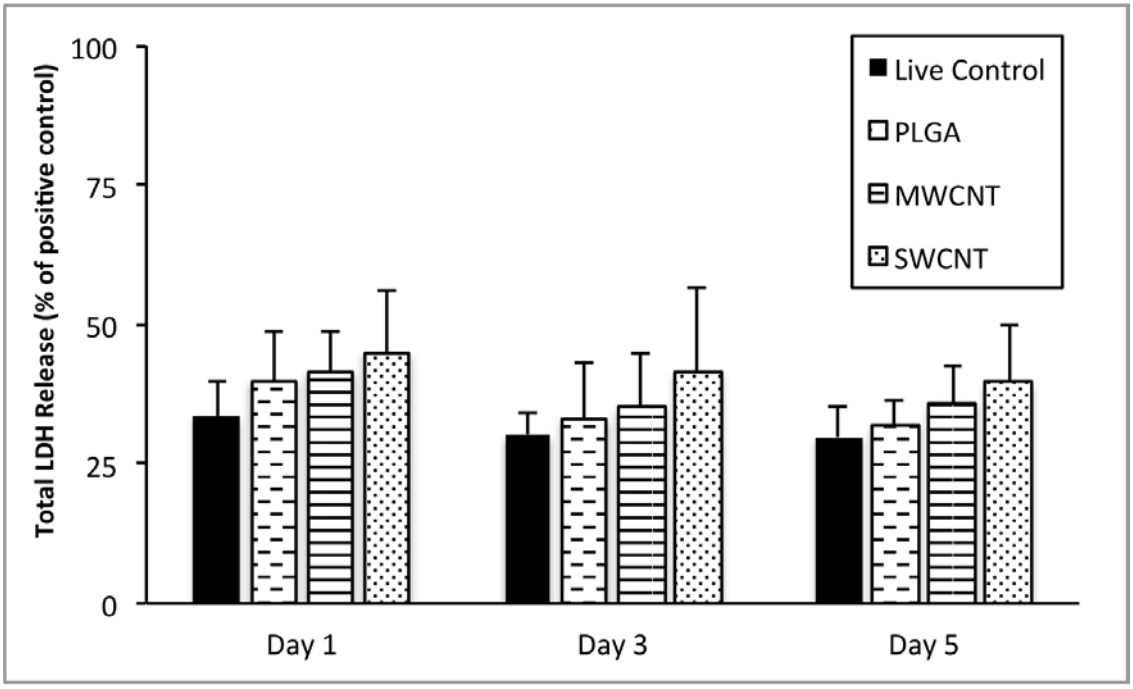

Figure 32: Cytotoxicity evaluation using lactate dehydrogenase assay after 1,3, and 5 days of ADSC culture on poly(lactic-co-glycolic) acid, multi walled carbon nanotube, and single walled carbon nanotube scaffolds. Chart represents total LDH release (%) normalized to positive controls (100% dead cells). Data is represented as means ± standard deviation.

4.3.3 Calcein-AM fluorescence imaging

Calcein-AM is a non-fluorescent dye, which upon cellular internalization, is converted to green fluorescent calcein due to removal of acetoxymethyl ester group by intracellular esterases, and is retained in the cytoplasm of living cells. Therefore, it is widely used to stain living eukaryotic cells [14, 15]. Figure 33 shows representative calcein-AM stained images of ADSCs cultured on PLGA (Figure 33 A-E), MWCNT (Figure 33 F-J) and SWCNT (Figure 33 K-O) scaffolds after 1, 3, 5, 15 and 30 days. Presence of live ADSCs was observed after 24 hours of culture on PLGA, MWCNT and SWCNT scaffolds as observed in Figure 33 A, F and K, respectively. For each scaffold group, an increase in

the number of green-fluorescent cells was observed from D1 to D30. ADSCs on all scaffold groups on D30 appear to be confluent and uniformly distributed.

4.3.4 Immunofluorescence for focal adhesion and cell proliferation

4.3.4.1 Cell attachment – focal adhesion (vinculin)

Vinculin is a membrane cytoskeletal protein important for the formation of focal adhesion assembly and has been widely used as a marker to characterize cell-matrix adhesion [16]. Figure 34 shows representative images of ADSCs cultured on PLGA (Figure 34 A-C), MWCNT (Figure 34 D-F) and SWCNT (Figure 34 G-I) scaffolds. ADSCs are stained green using FITC-phalloidin for cytoskeleton (green fluorescence) and fluorescently labeled antibodies for vinculin expression (red fluorescence). To ascertain co-localization of red and green fluorescence and corroborate the absence of non-specific signal, merged images are also presented. Figure 34 B, E, and H confirm the expression of vinculin by ADSCs cultured on PLGA, MWCNT and SWCNT scaffolds, respectively. The vinculin protein appears to be co-localized with actin filaments (Figure 34 A, D and G) and evenly distributed throughout the cytoplasm (Figure 34 C, F, I).

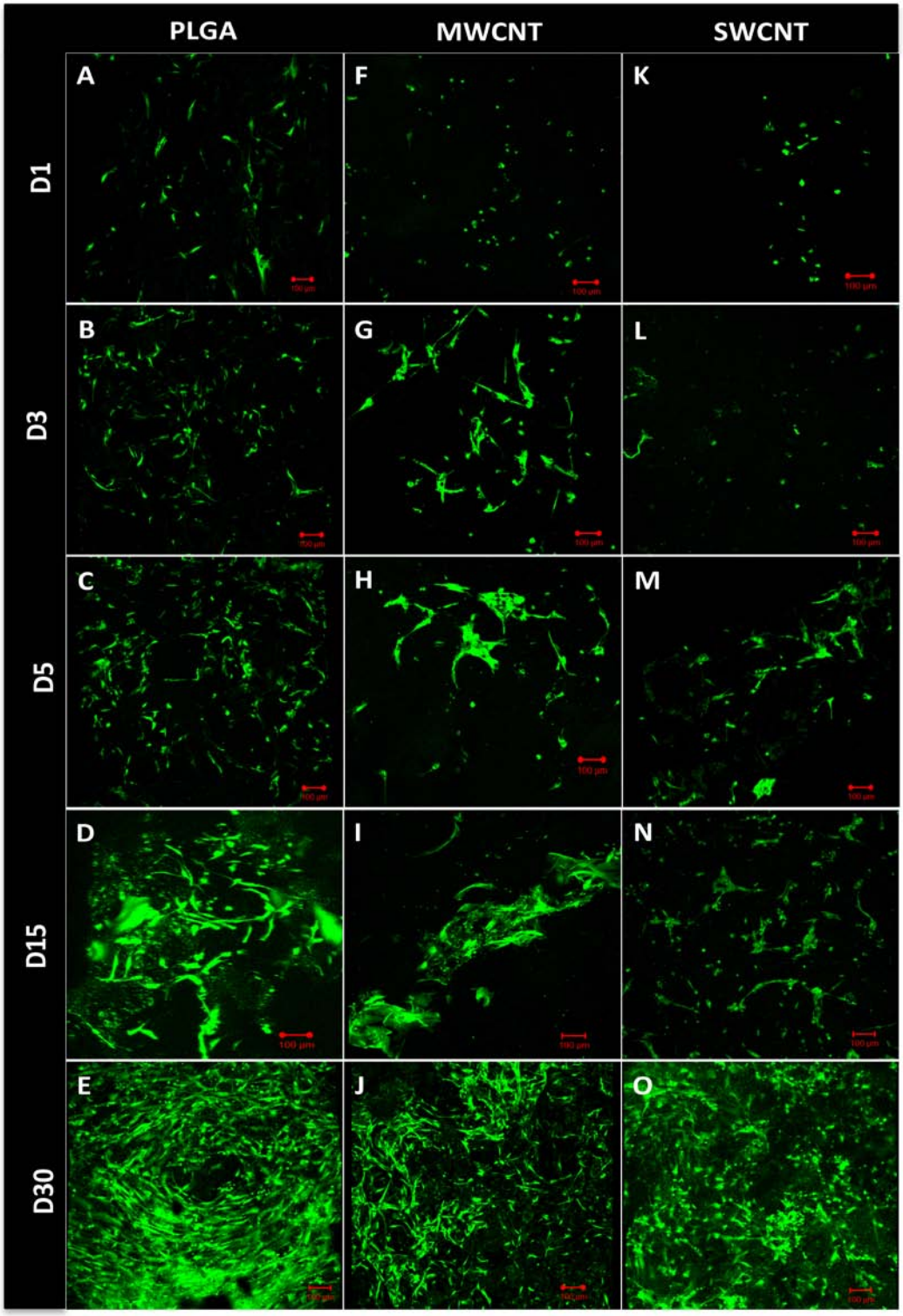

Figure 33: Representative calcein-AM stained green fluorescence images of ADSCs on poly(lactic-co-glycolic) scaffolds (A-E), multi walled carbon nanotube scaffolds (F-J), and single walled carbon nanotube scaffolds (K-O) after 1, 3, 5, 15, and 30 days of culture. Presence of live ADSCs on the scaffolds can be observed. Scale bars are 100 µm.

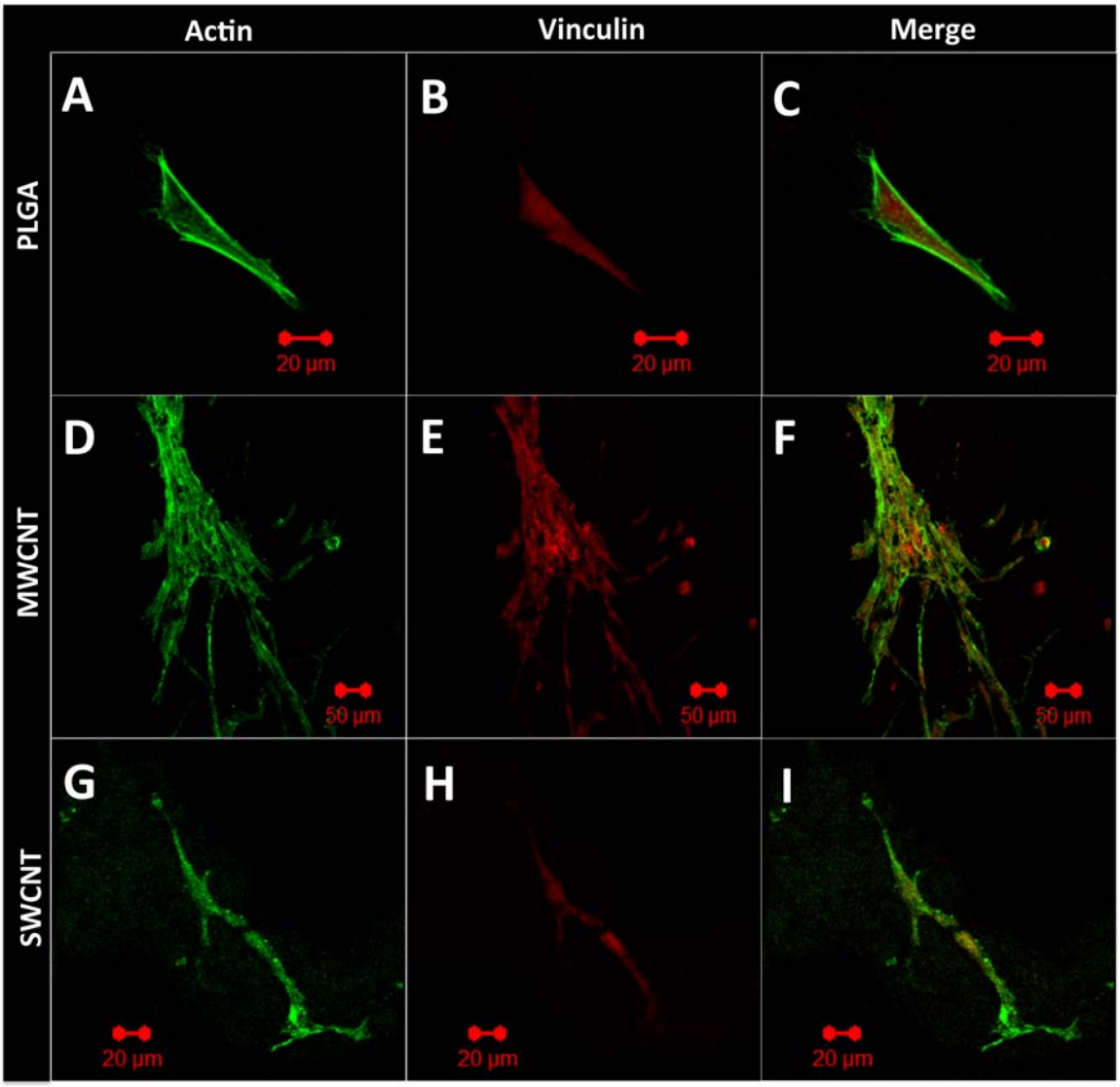

Figure 34: Representative immunofluorescence images of ADSCs cultured on (A-C) poly(lactic-co-glycolic) acid, (D-F) multi walled carbon nanotube and (G-I) single walled carbon nanotube scaffolds after 5 days stained green for actin cytoskeleton and red for focal adhesions, i.e. vinculin protein. Merged images are also shown to depict co-localization of actin filaments and vinculin protein.

4.3.4.2 Cell proliferation (Ki-67)

Ki-67 is an antigen expressed during the active phases of cell cycle (G1, S, G2 and mitosis). The expression of Ki-67 is absent during the G0 phase; therefore, it has been widely used as a marker of cell proliferation. Figure 35 shows representative confocal microscopy images of immunofluorescence staining for Ki-67 expression by ADSCs

cultured on PLGA (Figure 35 A-C), MWCNT (Figure 35 D-F) and SWCNT (Figure 35 G-I) scaffolds after 5 days. ADSCs cells were stained with FITC conjugated phalloidin for actin cytoskeleton (green fluorescence, Figure 35 A, D and G) and fluorescently labeled antibodies for Ki-67 expression (red fluorescence, Figure 35 B, E and H). Figure 35 C, F and I are merged images for actin cytoskeleton and Ki-67 protein. Ki-67 expression can be observed throughout the cytoplasm and nucleus for cells seeded on PLGA (Figure 35 B and C), MWCNT (Figure 35 E and F) and SWCNT (Figure 35 H and I) scaffolds suggesting that ADSCs on all scaffold groups were metabolically active and proliferating.

4.3.5 SEM imaging for cell attachment

SEM was used for the characterization of cellular adhesion and morphology. Figure 36 shows representative SEM images of ADSCs on PLGA (Figure 36 A), MWCNT (Figure 36 B) and SWCNT (Figure 36 C) scaffolds after 5 days. The cells appear horizontally spread out on all scaffold groups (white arrows, Figure 36). ADSCs on all the scaffolds show formation of cytoplasmic extensions and membrane projections with no preferential direction. Figure 36 D and E are representative high magnification SEM images of ADSCs on MWCNT scaffolds. Formation of filopodia that attach and wrap around the underlying nanotube network can be clearly visualized (yellow arrows, Figure 36 D and E).

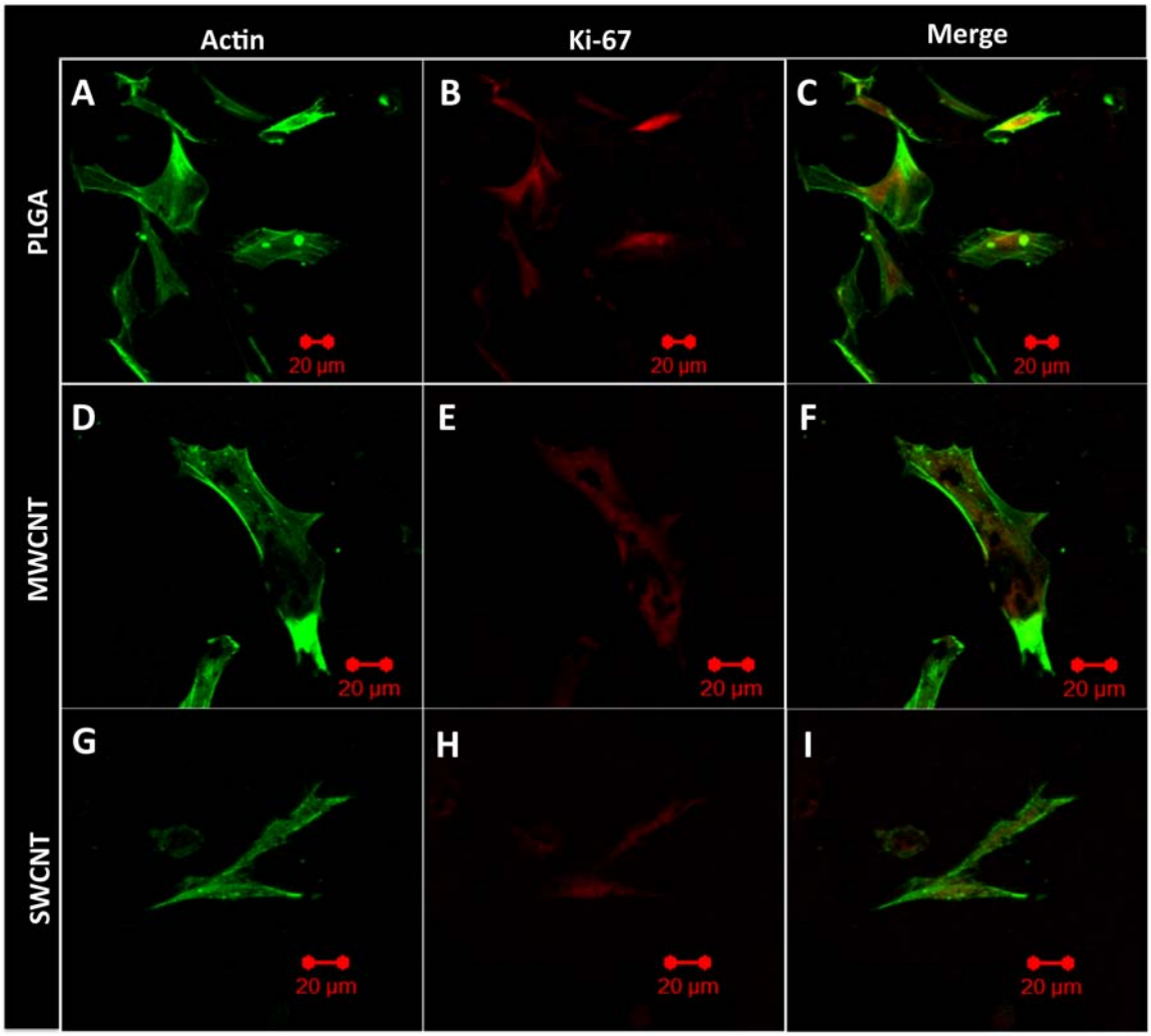

Figure 35 Representative immunofluorescence images of ADSCs cultured on (A-C) poly(lactic-co-glycolic) acid, (D-F) multi walled carbon nanotube and (G-I) single walled carbon nanotube scaffolds after 5 days stained green for actin cytoskeleton and red for cell proliferation marker, i.e. Ki-67 protein. Merged images are also shown to depict co-localization of actin filaments and Ki-67 protein.

4.3.6 Image processing to assess cellular infiltration

Cellular infiltration inside PLGA, MWCNT and SWCNT scaffolds was assessed by image processing of Z-stacks of calcein-AM stained ADSCs. Each individual stack was subjected to spectral-color coding steps to false color-code the cells as a function of Z-

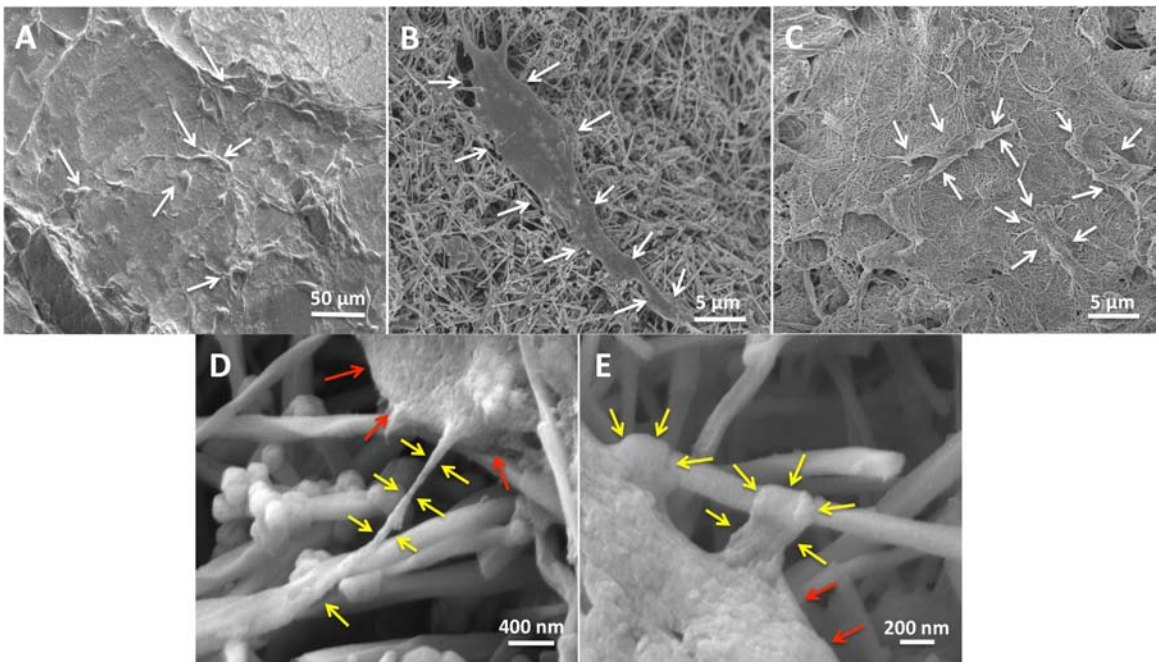

Figure 36: Representative SEM images showing adhesion of ADSCs on (A) poly(lactic-co-glycolic) acid, (B) multi walled carbon nanotube, and (C) single walled carbon nanotube scaffolds. Formation of cytoplasmic extensions (filopodia and pseudopodia) can be observed for all scaffold groups. Images D and E are high magnification images of ADSCs on MWCNT scaffolds. Formation of filopodia and cytoplasmic extensions are (yellow arrows) visible. Red arrows correspond to cytoplasm.

depth i.e. cellular infiltration. Figure 37 A, B, and C show infiltration of cells on PLGA, MWCNT and SWCNT scaffolds, respectively. Presence of cells can be detected upto a depth of ~200-450 µm for each scaffold group. Image acquisition beyond that depth was not possible due to limitations with laser penetration inside 3D scaffolds.

4.3.7 Immunofluorescence for MSC phenotype analysis

Surface antigens have been extensively used for the identification of specific cell populations. According to ISCT guidelines, MSCs should express CD73, CD90 and CD105 whereas lack the expression of hematopoietic cell markers such as CD14, CD19,

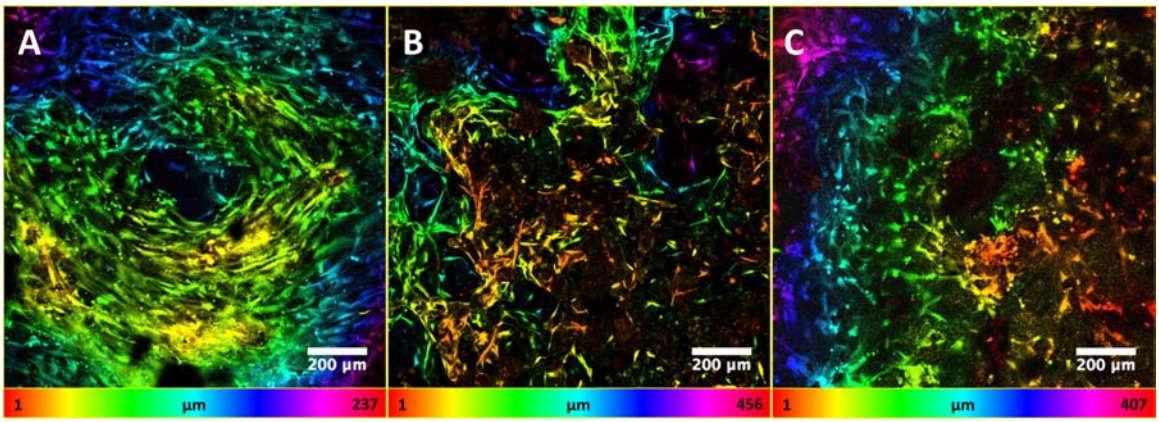

Figure 37: Representative spectrally color coded images of calcein-AM stained ADSCs as a function of confocal Z-depth (i.e. cellular infiltration) after 5 days of culture on (A) poly(lactic-co-glycolic) acid, (B) multi walled carbon nanotube and (C) single walled carbon nanotube scaffolds. Presence of cells can be detected upto a depth of ~200-450 µm for MWCNT and SWCNT scaffolds and ~240 µm for PLGA scaffolds. Although ADSCs in all the scaffold groups exist beyond the represented depths, limitations associated with laser penetration restricted their imaging.

CD34 and CD45 [6]. Figure 38 shows representative immunofluorescence images of ADSCs stained for various stem cell markers after 15 days of culture on PLGA (Figure 38 (a)), MWCNT (Figure 38 (b)) and SWCNT (Figure 38 (c)) scaffolds. Cells were stained with rhodamine phalloidin (red fluorescence) for actin cytoskeleton and FITC conjugated monoclonal antibodies (green fluorescence) for MSC surface antigens. ADSCs on all scaffold groups express CD73, CD90 and CD105 whereas lack the expression of CD14, CD19, CD34 and CD45, thereby satisfying the criteria for MSC phenotype.

4.3.8 Osteogenic differentiation

4.3.8.1 Alkaline phosphatase (ALP) activity

Alkaline phosphatase is an early-stage osteogenic marker [17]. Figure 39 shows ALP activity of ADSCs trypsinized and expanded *in vitro* after 30 days of culture on PLGA, MWCNT and SWCNT scaffolds. ALP activity between the groups ranged from ~1.8-3 μM/ng dsDNA with ADSCs isolated from SWCNT scaffolds showing a significant decrease in ALP expression compared to control ADSCs cultured on TCPS. ADSCs isolated from PLGA and MWCNT scaffolds showed a similar level of ALP activity as control ADSCs.

4.3.8.2 Alizarin red staining

Alizarin red binds to calcium deposits in the extracellular matrix (ECM) and has been widely used to detect the presence of calcium in ECM of osteogenic cells [10]. ADSCs isolated from PLGA (Figure 40 B), MWCNT (Figure 40 C) and SWCNT (Figure 40 D) scaffolds after 30 days of culture show good deposition of calcium in the ECM (red staining, black arrows), comparable to control ADSCs (Figure 40 A). There was no difference in distribution of the staining pattern between various scaffold groups compared to control ADSCs.

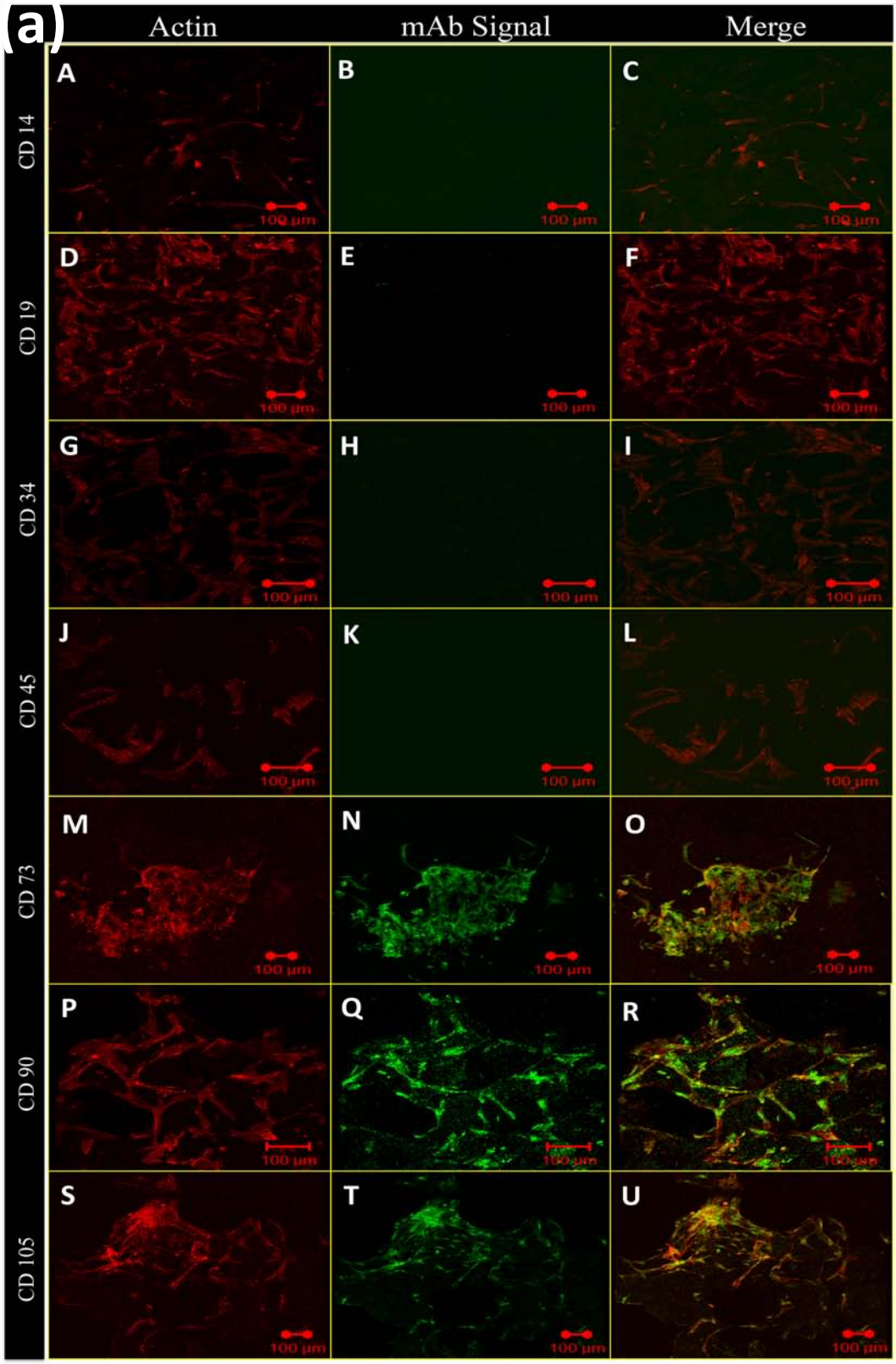

Figure 37: representative immunofluorescence images of ADSCs stained for MSC surface antigens (CD14, CD19, CD34, CD45, CD73, CD90 and CD105) after 15 days of culture on (a) poly(lactic-co-glycolic) acid scaffolds, (b) multi walled carbon nanotube scaffolds and (c) single walled carbon nanotube scaffolds. The red fluorescence represents rhodamine phalloidin stained cytoplasm whereas green fluorescence represents the expression of the surface antigen.

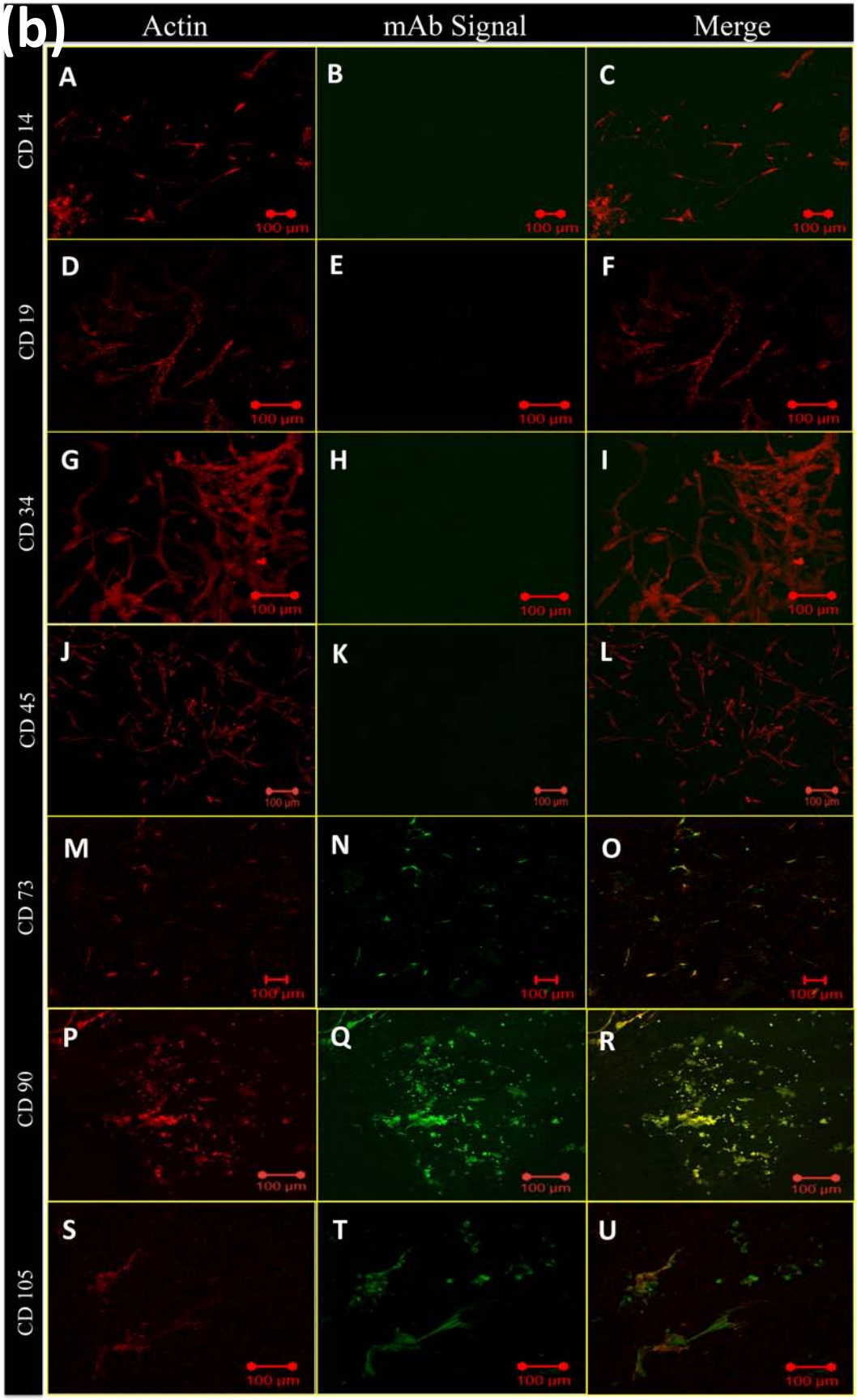
(b)
Actin
mAb Signal
Merge
CD 14
CD 19
CD 34
CD 45
CD 73
CD 90
CD 105
A
B
C
D
E
F
G
H
I
J
K
L
M
N
O
P
Q
R
S
T
U
100 µm

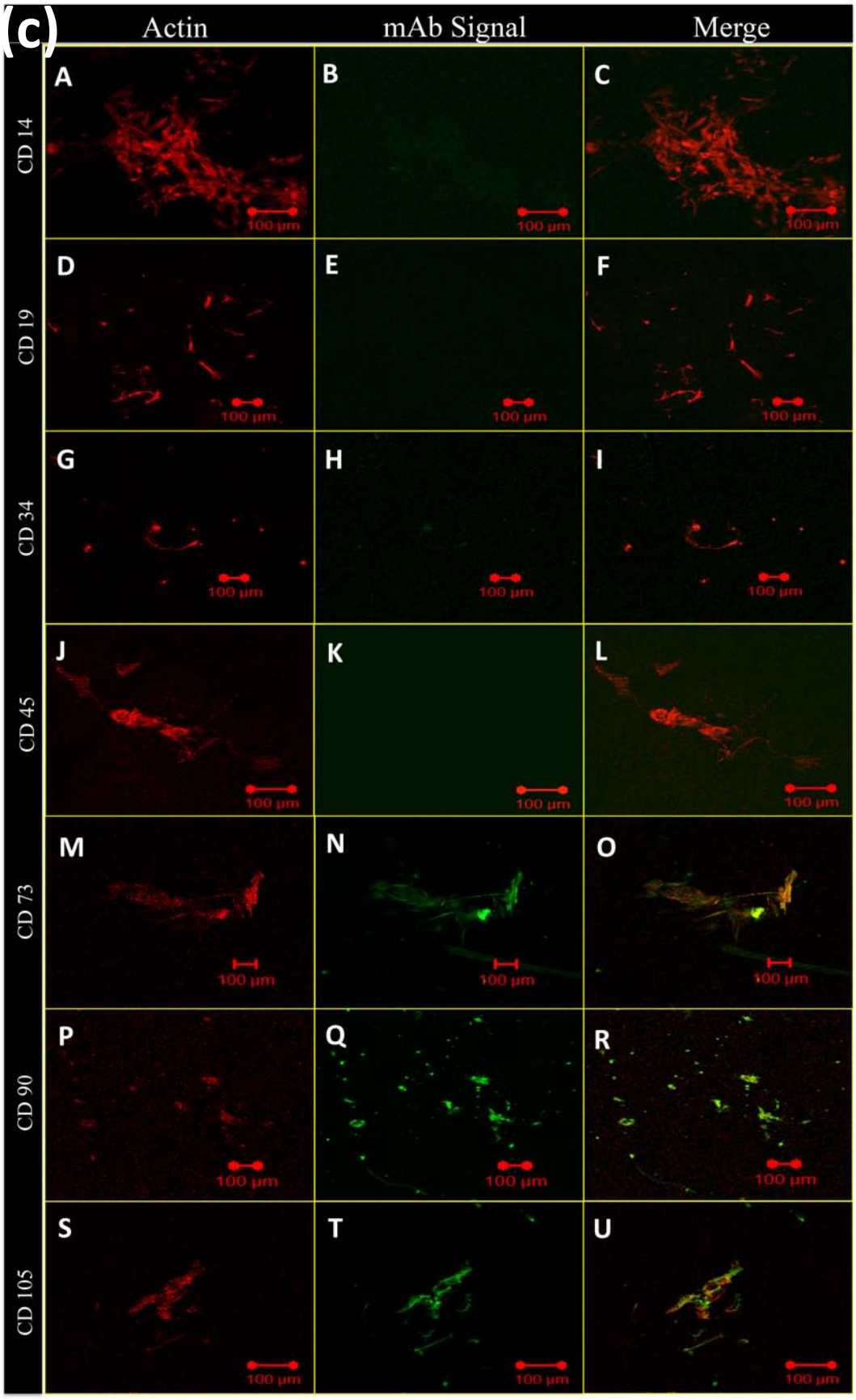
(c)
Actin
mAb Signal
Merge
CD 14
CD 19
CD 34
CD 45
CD 73
CD 90
CD 105
A
B
C
D
E
F
G
H
I
J
K
L
M
N
O
P
Q
R
S
T
U
100 µm

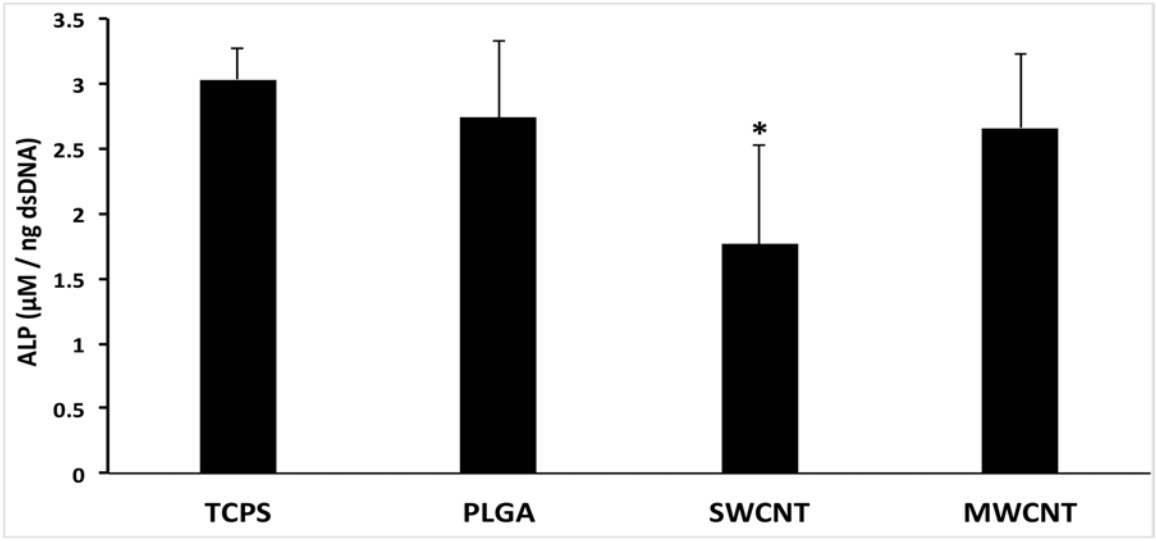

Figure 39: Alkaline phosphatase activity of ADSCs maintained on (control group) and ADSCs harvested after 30 days of culture from poly(lactic-co-glycolic) acid (PLGA), (C) multi walled carbon nanotubes (MWCNT), and (C) single walled carbon nanotube (SWCNT) scaffolds and subsequently subjected osteogenic differentiation *in vitro*. Data is represented as means ± standard deviation. Groups with a significant difference ($p < 0.05$) are marked with "*".

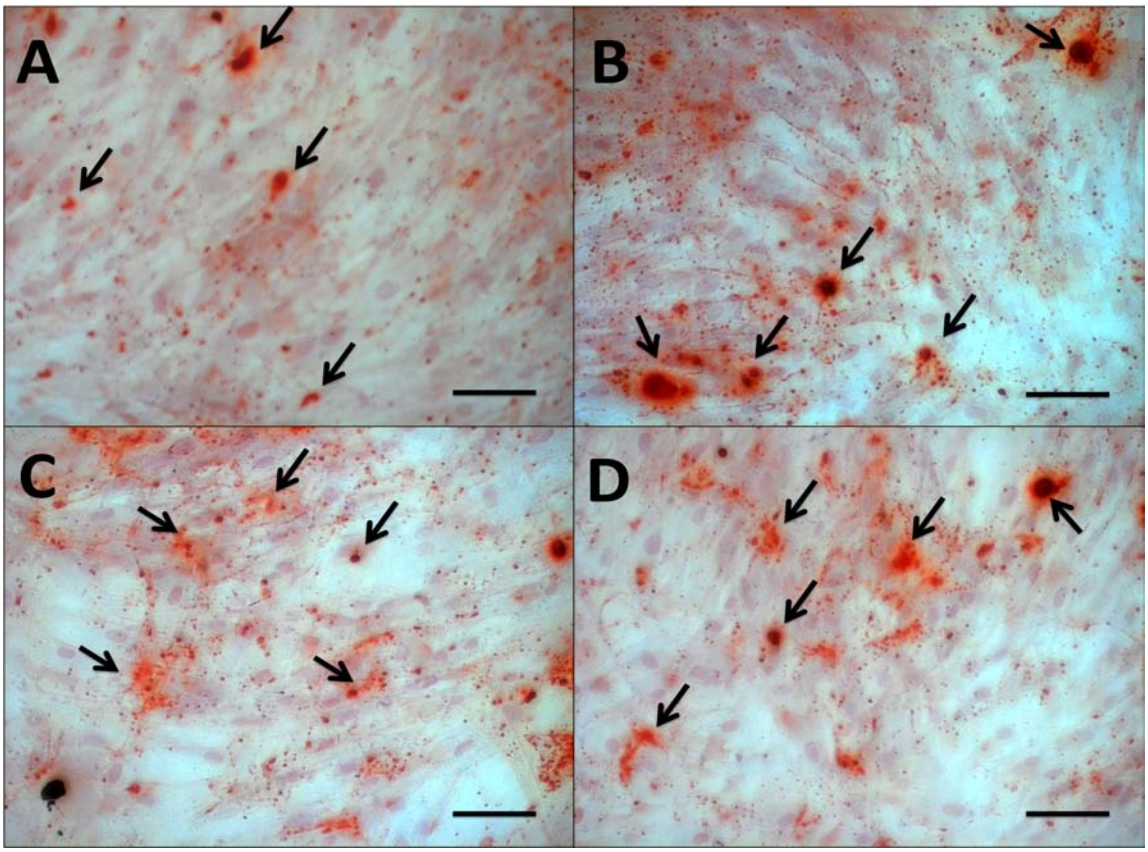

Figure 38: Representative alizarin red stained images of (A) ADSCs maintained on TCPS subjected to osteogenic differentiation. ADSCs harvested after 30 days of culture from (B) poly(lactic-co-glycolic) acid, (C) multi walled carbon nanotubes, and (C) single walled carbon nanotube scaffolds and subsequently subjected osteogenic differentiation *in vitro*. Depositions of calcium in the extracellular matrix are stained red (black arrows). Scale bars are 100 µm.

4.3.9 Adipogenic differentiation

4.3.9.1 Oil red O staining

Oil red O is a fat-soluble dye that specifically stains triglycerides, cholesteryl esters and neutral lipids without staining biological membranes [18]. ADSCs isolated from PLGA, MWCNT and SWCNT scaffolds (Figure 41 B, C and D) show presence of intracellular fat vacuoles (red stain, black arrows) similar to ADSCs cultured on TCPS controls. The

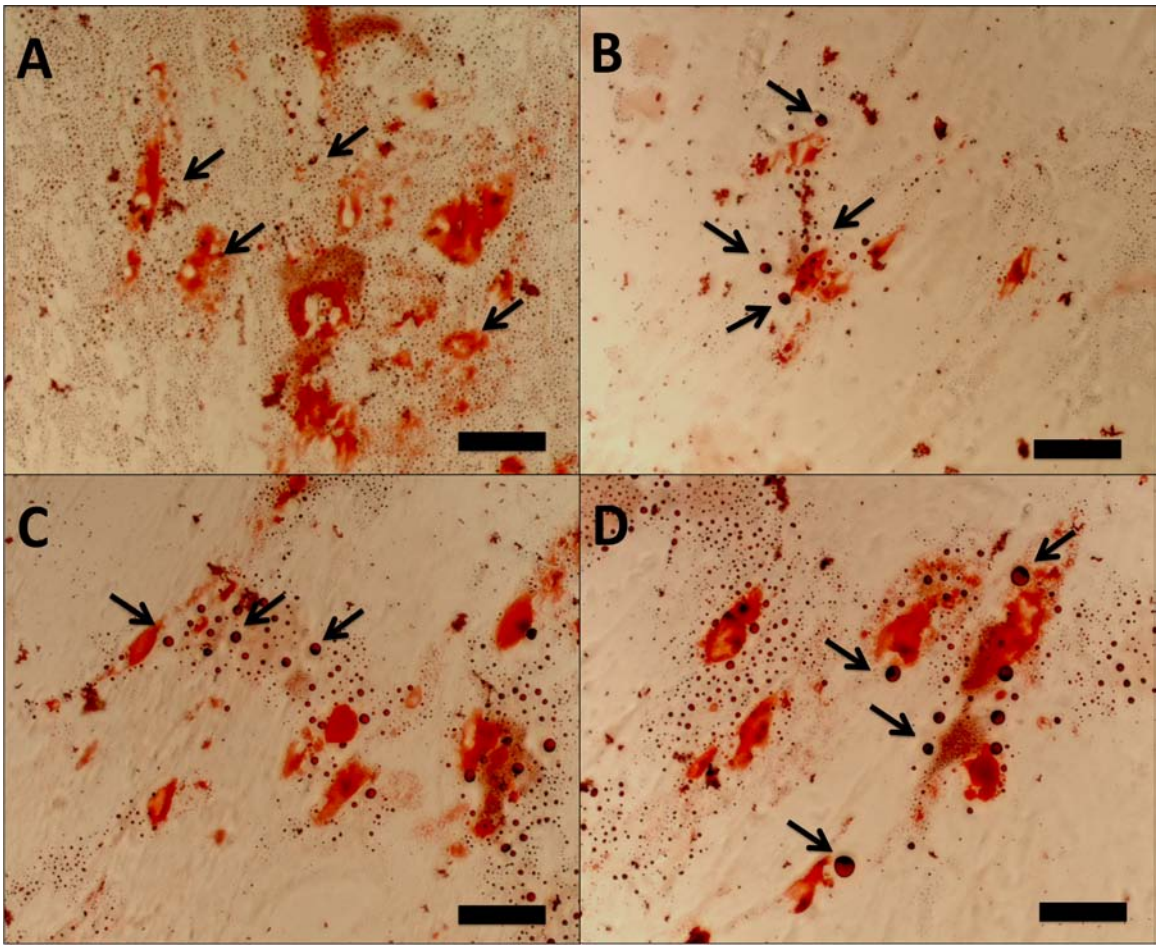

Figure 40: Representative Oil-red O stained images of (A) ADSCs maintained on TCPS subjected to adipogenic differentiation. ADSCs harvested after 30 days of culture from (B) poly(lactic-co-glycolic) acid, (C) multi walled carbon nanotubes, and (C) single walled carbon nanotube scaffolds and subsequently subjected adipogenic differentiation *in vitro*. Fat vacuoles are stained red (black arrows). Scale bars are 50 µm.

fat vacuoles appear to be distributed throughout the cytoplasm.

4.3.10 Chondrogenic differentiation

4.3.10.1 Alcian blue staining

Alcian blue is widely used to stain acidic polysaccharides such as glycosaminoglycans (GAGs) present in the extracellular matrix of chondrocytes. Figure 42 (A-D) show

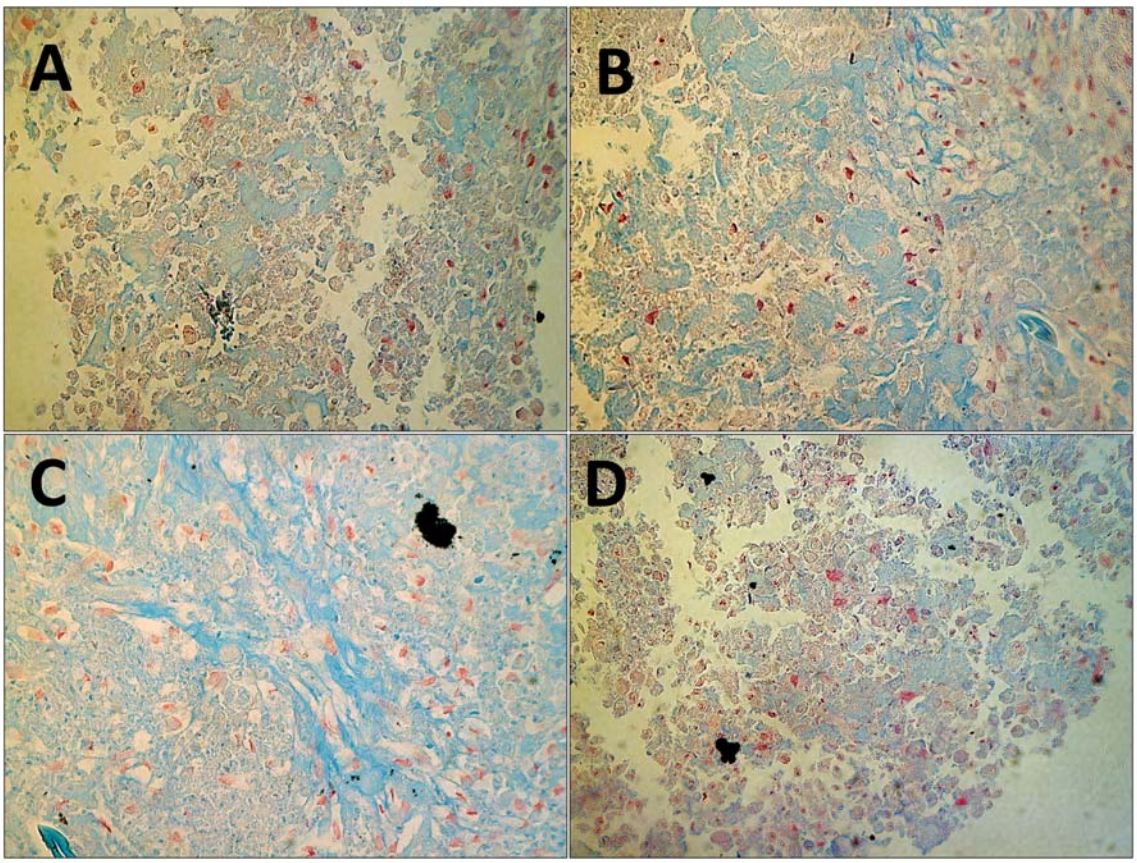

Figure 41: Representative Alcian blue stained images of (A) ADSCs maintained on TCPS subjected to chondrogenic differentiation. ADSCs harvested after 30 days of culture from (B) poly(lactic-co-glycolic) acid, (C) multi walled carbon nanotube and (D) single walled carbon nanotube scaffolds and subsequently subjected to chondrogenic differentiation *in vitro.* Cartilaginous extracellular matrix containing deposits of sulfated glycosaminoglycans are stained blue.

representative Alcian blue stained images of normal TCPS ADSCs, ADSCs isolated from PLGA, MWCNT and SWCNT scaffolds, respectively, after chondrogenic differentiation. The blue color shows the deposition of GAGs in the ECM. No significant differences were observed between PLGA, MWCNT and SWCNT scaffold groups.

4.4 Discussions

The goal of this study was to investigate the interactions between 3D porous all-carbon scaffolds fabricated using CNTs as building blocks and human adipose derived stem cells (ADSCs) and explore the potential use of 3D CNT scaffolds as matrices for stem cell expansion and maintenance. The radical initiated thermal crosslinking method used to fabricate 3D MWCNT and SWCNT scaffolds and their physiochemical properties (scaffold morphology and topography, mechanical properties, chemical properties, electrical conductivity, porosity, pore architecture and surface roughness) have been reported in chapters 2 and 3 [13]. In this study, 3D MWCNT and SWCNT scaffolds of dimensions ~4 mm in height and 3-4 mm in diameter with 80-85% porosity were fabricated. Porous PLGA scaffolds of similar porosity and dimensions were used as controls since PLGA is a biocompatible FDA approved polymer for biomedical applications.

LDH assay was performed to quantitatively assess the cytotoxicity of MWCNT and SWCNT scaffolds against ADSCs after 1, 3, and 5 days of culture. Porous PLGA

scaffolds were used as live controls. LDH assay is a widely recommended method to analyze the cytotoxicity of carbon nanomaterials [19]. It has been extensively reported that several assays (such as MTT, XTT) produce erroneous results due to non-specific binding of formazan crystals on nanotube surface. LDH assay measures cell death by quantifying the amount of cytosolic enzyme lactate dehydrogenase released in the media by apoptotic and necrotic cells [19]. Therefore, no formazan-nanotube interference is observed. LDH assay has been widely used for the cytotoxicity analysis of carbon nanomaterials [7, 14, 19, 20]. We observed no significant differences in the total LDH released by ADSCs cultured on PLGA, MWCNT and SWCNT scaffolds at all time points (Figure 32). These results suggest that MWCNT and SWCNT scaffolds are cytocompatible, comparable to FDA approved PLGA polymer. To further corroborate the results of LDH assay, ADSCs after 1, 3, 5, 15, and 30 days of culture on PLGA, MWCNT and SWCNT scaffolds were stained with calcein-AM, a fluorescent marker of metabolically active living cells [21]. Green fluorescence observed in Figure 33 A-O confirms the presence of live ADSCs on all scaffold groups at all time points. Furthermore, an increase in cell number can be observed between 1-30 days for all scaffold groups suggesting that ADSCs on MWCNT and SWCNT scaffolds show good cell proliferation.

In mammalian cells, vinculin protein is responsible for the formation of macromolecular assemblies such as focal adhesions that link integrin proteins to the actin cytoskeleton of the cell, thereby facilitating cell attachment to the underlying ECM [16, 22]. Focal adhesion complexes govern several cellular functions and modulate the expression

(up/down-regulation) of genes associated with cell proliferation, migration and apoptosis [23]. Immunofluorescence imaging of ADSCs confirm the presence of vinculin protein (red fluorescence, Figure 34) distributed throughout the cytoplasm (green fluorescence, Figure 34). These results suggest that ADSCs can form focal adhesion complexes on MWCNT and SWCNT scaffolds. Ki-67 is a cell proliferation marker, which is expressed only during the active phases of the cell cycle (G1, S, G2 and M) and absent during the resting phase (G0) and has been extensively used as a marker for cell proliferation [24-26]. ADSC cultured on MWCNT and SWCNT scaffolds express Ki-67 gene (red fluorescence, Figure 35). These results suggest that ADSCs are metabolically active and can proliferate on MWCNT and SWCNT scaffolds.

Cellular infiltration into 3D scaffolds is critical for tissue healing and regeneration. It is well known that cell infiltration into 3D scaffolds is governed by the turnover of vinculin (focal adhesion assemblies) [16]. Furthermore, the expression of vinculin is diffusely distributed in cells growing on 3D substrates [27]. ADSCs on MWCNT and SWCNT scaffolds express a cytoplasmic distribution of vinculin thereby suggesting that ADSCs are capable of infiltration inside the 3D scaffolds. For cells embedded in a 3D matrix, filopodia or cytoplasmic extensions are responsible for governing cellular infiltration [16]. SEM analysis (Figure 36) of ADSCs on PLGA, MWCNT and SWCNT scaffolds show the attachment of ADSCs and the presence of numerous cytoplasmic extensions or filopodia (Figure 36 D and E, yellow arrows). The spectrally color coded images of ADSCs on MWCNT and SWCNT scaffolds (Figure 37) confirm cellular infiltration upto depths of ~400-450 μm in MWCNT and SWCNT scaffolds. Image acquisition beyond

this depth was not possible due to limitations associated with the depth of penetration of the laser.

The Mesenchymal and Tissue Stem Cell Committee of ISCT have released guidelines that define human MSCs for laboratory research and preclinical investigations. First, MSCs must be plastic adherent when cultured *in vitro* on TCPS. Second, >95% of MSCs should express CD73 (a.k.a. ecto 5' nucleotidase), CD90 (a.k.a. Thy-1) and CD105 (a.k.a. endoglin), and lack the expression of CD14 (marker of monocytes and macrophages), CD19 (B cell marker), CD34 (hematopoietic progenitor marker) and CD45 (pan-leukocyte marker). Third, the cells must be able to demonstrate multi-lineage differentiation potential by differentiating into osteoblasts, adipocytes and chondrocytes demonstrated by alizarin red, oil red O and Alcian blue staining, respectively. Surface antigens have been extensively used for the characterization of various cell types. Figure 38 shows representative immunofluorescence images of various surface markers of ADSCs after 15 days of culture on PLGA (Figure 38 A), MWCNT (Figure 38 B) and SWCNT (Figure 38 C) scaffolds. ADSCs on all scaffold groups satisfy the criteria for MSC surface antigen profile.

ADSCs from PLGA, MWCNT and SWCNT scaffolds were harvested by trypsinization and expanded *in vitro* thereby demonstrating their adherence to TCPS. The ADSCs were then subjected to multi-lineage differentiation. Figure 39 shows ALP activity of ADSCs after 30 days of culture on various scaffold groups. ALP is an early stage marker of

osteogenesis. No significant differences were observed in the ALP activity of ADSCs cultured on PLGA and MWCNT scaffolds, compared to normal TCPS ADSCs (control group). Although, ADSCs cultured on SWCNT scaffolds showed a lower ALP activity, the deposition of calcium in the ECM of ADSCs of all scaffold groups observed by alizarin red staining (Figure 40) confirms their successful osteogenic differentiation. Oil red O staining shows the presence of lipid vacuoles (Figure 41, black arrows) in ADSCs of all scaffold groups thereby confirming their adipogenic differentiation. Alcian blue staining (Figure 41) shows the presence of cartilaginous ECM (deposition of sulfated GAGs) by ADSCs of all scaffold groups thereby confirming their differentiation into chondrocytes. These results taken together suggest that ADSCS cultured on 3D MWCNT and SWCNT scaffolds satisfy all the criteria that define human MSCs as recommended by ISCT. Therefore, 3D MWCNT and SWCNT scaffolds can be used as novel synthetic matrices for stem cell expansion and maintenance.

Several studies have reported the use of 2D substrates coated with carbon nanomaterials for stem cell maintenance and differentiation. Holy et. al. have reported enhanced cell adhesion and maintenance of pluripotent stem cells in an undifferentiated state on MWCNT coated glass substrates [28]. Brunner et. al. have reported that altering the surface roughness of MWCNT films can influence adhesion, proliferation and colony morphology of human embryonic stem cells and envision the development of MWCNT coated films as tunable surfaces for the control of stem cell behavior [29]. Mooney et. al. have reported the differentiation of MSCs into osteoblasts, adipocytes and chondrocytes on COOH-functionalized MWCNT substrates [30]. Recently, Pryzhkova et. al. showed

differentiation of human pluripotent stem cells into all three embryonic germ layers that can be controlled by the nanotopography and surface roughness of CNT arrays [31]. Graphene coated substrates have been reported to accelerate the differentiation of MSCs into osteoblasts [32-34] and neuronal stem cells towards astrocytes and neurons [35, 36]. However, for tissue engineering applications across various length scales and to achieve high MSC numbers for cellular therapy, 3D substrates have been recommended since MSCs exhibit increase proliferation on 3D substrates [37]. Recently, 3D substrates of CNTs and graphene fabricated using chemical vapor deposition (CVD) and sacrificial template transfer methods have been reported as cytocompatible substrates for tissue engineering applications [34, 35, 38]. However, the ability of these methods to control the porosity of 3D CNT scaffolds or form covalent bonds between CNTs (important for mechanical stability of scaffolds for *in vivo* biomedical applications) still needs to be demonstrated.

Bone marrow (BM) aspirates are the most commonly used source for the isolation of MSCs (BMSCs). However, the prevalence of adult MSCs in BM aspirates is very low (approximately 0.0001-0.01%) [39]. Furthermore, the number of MSCs drastically reduces from BM aspirates of elderly due to aging [40]. A convenient alternative is to isolate MSCs from adipose tissue, which can be obtained by a simple liposuction procedure in clinic. The number of MSCs isolated from adipose tissue is nearly 500-folds greater compared to an equivalent amount of BM aspirate [41, 42]. It has been shown that ADSCs and BMSCs exhibit similar multi-lineage differentiation potential and immunosuppressive properties with minor differences in transcriptome and proteome.

Human ADSCs are genetically stable in long-term cell culture, show a higher proliferation capacity and rate (doubling time for ADSCs is 28 hours vs. 39 hours for BMSCs), and retain multi-lineage differentiation potential for longer time periods compared to BMSCs [40, 43-45]. Due to these advantages, stem cells derived from adipose tissue are an attractive alternative to bone marrow derived stem cells for clinical tissue engineering and regenerative medicine applications.

Stem cell therapy for conditions such as bone and cartilage defects, graft vs. host disease, myocardial infarction and autoimmune diseases requires ~4-5 million cells per kg body weight [5, 46, 47]. It is difficult to isolate MSCs in clinically relevant number from diseased patients or elderly donors who typically are the patients in need of therapy. Currently, the large-scale expansion of MSCs for therapy is an unmet clinical need since the cells undergo significant changes in phenotype such as diminished proliferation potential, senescence or loss of "stemness" (onset of lineage specific phenotypic characteristics) during prolonged culture on TCPS substrates. Consequently, to achieve high cell densities and maintain a greater pool of stem cells, 3D culture systems have been recommended for MSC expansion over conventional 2D substrates [3-5]. In addition to the above-mentioned benefits, 3D culture systems provide a better understanding of cellular mechanisms that guide stem cell behavior [37]. As a result, several approaches utilizing 3D culture systems for stem cell expansion *in vitro* have been developed. For example, stem cells have been cultured in alginate microcapsules [48], as cell aggregates [49, 50], in the presence of microcarriers [51, 52], on synthetic polymeric [37] and ceramic scaffolds [53, 54], hydrogels [55] and on decellularized

matrices as natural ECM-based scaffolds [5, 56]. Compared to these culture systems, 3D CNT scaffolds may possess additional multifunctional attributes: (1) The nanotopography, substrate stiffness, and electrical conductivity of CNT scaffolds can be exploited as a biophysical cue to control the spatiotemporal differentiation of stem cells inside a 3D scaffold thereby allowing potential multiphasic tissue regeneration. (2) CNTs have been reported as contrast agents for several bioimaging modalities such as magnetic resonance imaging and X-ray computed tomography. 3D CNT scaffolds may be used for non-invasive longitudinal monitoring of stem cell based therapy for tissue engineering applications. Therefore, in a true sense, 3D CNT scaffolds may be exploited as multifunctional substrates for stem cell expansion and maintenance and/or to control/guide in-situ multi-lineage differentiation of stem cells.

4.5 Conclusions

3D macroporous scaffolds fabricated using single- and multi- walled carbon nanotubes are cytocompatible substrates that show good cell viability, adhesion, proliferation and infiltration of human ADSCs. ADSCs after long-term expansion on MWCNT and SWCNT scaffolds retain their stem cell phenotype (express MSC surface antigens), can be harvested from 3D MWCNT and SWCNT scaffolds, and show robust multi-lineage differentiation into osteoblasts, adipocytes and chondrocytes. These results suggest that 3D macroporous MWCNT and SWCNT scaffolds can be used as synthetic 3D matrices for *ex-vivo* expansion and maintenance of MSCs for clinical therapeutic applications.

4.6 Acknowledgements

This work was supported by the National Institutes of Health (grants No. 1DP2OD007394-01).

4.7 References

1. Uccelli, A., L. Moretta, and V. Pistoia, *Mesenchymal stem cells in health and disease.* Nat Rev Immunol, 2008. **8**(9): p. 726-36.

2. Madrigal, M., K.S. Rao, and N.H. Riordan, *A review of therapeutic effects of mesenchymal stem cell secretions and induction of secretory modification by different culture methods.* J Transl Med, 2014. **12**(1): p. 260.

3. Chase, L.G., et al., *A novel serum-free medium for the expansion of human mesenchymal stem cells.* Stem cell research & therapy, 2010. **1**(1): p. 8.

4. Jung, S., et al., *Ex vivo expansion of human mesenchymal stem cells in defined serum-free media.* Stem cells international, 2012. **2012**.

5. Ng, C.P., et al., *Enhanced ex vivo expansion of adult mesenchymal stem cells by fetal mesenchymal stem cell ECM.* Biomaterials, 2014. **35**(13): p. 4046-57.

6. Dominici, M., et al., *Minimal criteria for defining multipotent mesenchymal stromal cells. The International Society for Cellular Therapy position statement.* Cytotherapy, 2006. **8**(4): p. 315-317.

7. Mullick Chowdhury, S., et al., *Cell specific cytotoxicity and uptake of graphene nanoribbons.* Biomaterials, 2013. **34**(1): p. 283-93.

8. Boufker, H.I., et al., *The Src inhibitor dasatinib accelerates the differentiation of human bone marrow-derived mesenchymal stromal cells into osteoblasts.* BMC cancer, 2010. **10**(1): p. 298.

9. Majors, A.K., et al., *Characterization of human bone marrow stromal cells with respect to osteoblastic differentiation.* Journal of Orthopaedic Research, 1997. **15**(4): p. 546-557.

10. Talukdar, Y., et al., *The effects of graphene nanostructures on mesenchymal stem cells.* Biomaterials, 2014. **35**(18): p. 4863-77.

11. Hong, L., et al., *Adipose tissue engineering by human adipose-derived stromal cells.* Cells Tissues Organs, 2006. **183**(3): p. 133-40.

12. Cai, X., et al., *Multiscale photoacoustic microscopy of single-walled carbon nanotube-incorporated tissue engineering scaffolds.* Tissue Eng Part C Methods, 2012. **18**(4): p. 310-7.

13. Lalwani, G., et al., *Fabrication and Characterization of Three-Dimensional Macroscopic All-Carbon Scaffolds.* Carbon N Y, 2013. **53**: p. 90-100.

14. Lalwani, G., et al., *Synthesis, Characterization, Phantom Imaging, and Cytotoxicity of A Novel Graphene-Based Multimodal Magnetic Resonance Imaging - X-Ray Computed Tomography Contrast Agent.* J Mater Chem B Mater Biol Med, 2014. **2**(22): p. 3519-3530.

15. Lalwani, G. and B. Sitharaman, *Multifunctional Fullerene-and Metallofullerene-Based Nanobiomaterials.* Nano LIFE, 2013. **3**(3): p. 1342003-1-22.

16. Fraley, S.I., et al., *A distinctive role for focal adhesion proteins in three-dimensional cell motility.* Nat Cell Biol, 2010. **12**(6): p. 598-604.

17. Graneli, C., et al., *Novel markers of osteogenic and adipogenic differentiation of human bone marrow stromal cells identified using a quantitative proteomics approach.* Stem Cell Res, 2014. **12**(1): p. 153-65.

18. Mehlem, A., et al., *Imaging of neutral lipids by oil red O for analyzing the metabolic status in health and disease.* Nat Protoc, 2013. **8**(6): p. 1149-54.

19. Worle-Knirsch, J.M., K. Pulskamp, and H.F. Krug, *Oops they did it again! Carbon nanotubes hoax scientists in viability assays.* Nano Lett, 2006. **6**(6): p. 1261-8.

20. Avti, P.K., E.D. Caparelli, and B. Sitharaman, *Cytotoxicity, cytocompatibility, cell-labeling efficiency, and in vitro cellular magnetic resonance imaging of gadolinium-catalyzed single-walled carbon nanotubes.* J Biomed Mater Res A, 2013. **101**(12): p. 3580-91.

21. Farshid, B., G. Lalwani, and B. Sitharaman, *In vitro cytocompatibility of one-dimensional and two-dimensional nanostructure-reinforced biodegradable polymeric nanocomposites.* J Biomed Mater Res A, 2014.

22. Demali, K.A., *Vinculin--a dynamic regulator of cell adhesion.* Trends Biochem Sci, 2004. **29**(11): p. 565-7.

23. Livshits, G., A. Kobielak, and E. Fuchs, *Governing epidermal homeostasis by coupling cell-cell adhesion to integrin and growth factor signaling, proliferation, and apoptosis.* Proc Natl Acad Sci U S A, 2012. **109**(13): p. 4886-91.

24. Schluter, C., et al., *The cell proliferation-associated antigen of antibody Ki-67: a very large, ubiquitous nuclear protein with numerous repeated elements, representing a new kind of cell cycle-maintaining proteins.* J Cell Biol, 1993. **123**(3): p. 513-22.

25. Gerdes, J., et al., *Immunobiochemical and molecular biologic characterization of the cell proliferation-associated nuclear antigen that is defined by monoclonal antibody Ki-67.* Am J Pathol, 1991. **138**(4): p. 867-73.

26. Scholzen, T. and J. Gerdes, *The Ki-67 protein: from the known and the unknown.* J Cell Physiol, 2000. **182**(3): p. 311-22.

27. Mierke, C.T., et al., *Vinculin facilitates cell invasion into three-dimensional collagen matrices.* J Biol Chem, 2010. **285**(17): p. 13121-30.

28. Holy, J., E. Perkins, and X. Yu, *Differentiation of pluripotent stem cells on multiwalled carbon nanotubes.* Conf Proc IEEE Eng Med Biol Soc, 2009. **2009**: p. 6022-5.

29. Brunner, E.W., et al., *Growth and proliferation of human embryonic stem cells on fully synthetic scaffolds based on carbon nanotubes.* ACS Appl Mater Interfaces, 2014. **6**(4): p. 2598-603.

30. Mooney, E., et al., *Carbon Nanotubes and Mesenchymal Stem Cells: Biocompatibility, Proliferation and Differentiation.* Nano Letters, 2008. **8**(8): p. 2137-2143.

31. Pryzhkova, M.V., et al., *Carbon nanotube-based substrates for modulation of human pluripotent stem cell fate.* Biomaterials, 2014. **35**(19): p. 5098-109.

32. Nayak, T.R., et al., *Graphene for controlled and accelerated osteogenic differentiation of human mesenchymal stem cells.* ACS Nano, 2011. **5**(6): p. 4670-8.

33. Lee, W.C., et al., *Origin of enhanced stem cell growth and differentiation on graphene and graphene oxide.* ACS Nano, 2011. **5**(9): p. 7334-41.

34. Crowder, S.W., et al., *Three-dimensional graphene foams promote osteogenic differentiation of human mesenchymal stem cells.* Nanoscale, 2013. **5**(10): p. 4171-6.

35. Li, N., et al., *Three-dimensional graphene foam as a biocompatible and conductive scaffold for neural stem cells.* Sci Rep, 2013. **3**: p. 1604.

36. Park, S.Y., et al., *Enhanced differentiation of human neural stem cells into neurons on graphene.* Advanced Materials, 2011. **23**(36): p. H263-H267.

37. Meng, X., et al., *Stem cells in a three-dimensional scaffold environment.* Springerplus, 2014. **3**: p. 80.

38. Nardecchia, S., et al., *Modulating the cytocompatibility of tridimensional carbon nanotube-based scaffolds.* Journal of Materials Chemistry B, 2013. **1**(24): p. 3064-3072.

39. ESTER BERNARDO, M., F. LOCATELLI, and W.E. FIBBE, *Mesenchymal stromal cells: a novel treatment modality for tissue repair.* Annals of the New York Academy of Sciences, 2009. **1176**: p. 101-117.

40. Puissant, B., et al., *Immunomodulatory effect of human adipose tissue-derived adult stem cells: comparison with bone marrow mesenchymal stem cells.* Br J Haematol, 2005. **129**(1): p. 118-29.

41. Hass, R., et al., *Different populations and sources of human mesenchymal stem cells (MSC): A comparison of adult and neonatal tissue-derived MSC.* Cell Commun Signal, 2011. **9**: p. 12.

42. Fraser, J.K., et al., *Fat tissue: an underappreciated source of stem cells for biotechnology.* Trends Biotechnol, 2006. **24**(4): p. 150-4.

43. Yoo, K.H., et al., *Comparison of immunomodulatory properties of mesenchymal stem cells derived from adult human tissues.* Cell Immunol, 2009. **259**(2): p. 150-6.

44. Zhu, X., J. Du, and G. Liu, *The comparison of multilineage differentiation of bone marrow and adipose-derived mesenchymal stem cells.* Clin Lab, 2012. **58**(9-10): p. 897-903.

45. Strioga, M., et al., *Same or not the same? Comparison of adipose tissue-derived versus bone marrow-derived mesenchymal stem and stromal cells.* Stem Cells Dev, 2012. **21**(14): p. 2724-52.

46. Binato, R., et al., *Stability of human mesenchymal stem cells during in vitro culture: considerations for cell therapy.* Cell Prolif, 2013. **46**(1): p. 10-22.

47. Jung, S., et al., *Ex vivo expansion of human mesenchymal stem cells in defined serum-free media.* Stem Cells Int, 2012. **2012**: p. 123030.

48. Jing, D., A. Parikh, and E.S. Tzanakakis, *Cardiac cell generation from encapsulated embryonic stem cells in static and scalable culture systems.* Cell Transplant, 2010. **19**(11): p. 1397-412.

49. Singh, H., et al., *Up-scaling single cell-inoculated suspension culture of human embryonic stem cells.* Stem Cell Res, 2010. **4**(3): p. 165-79.

50. Amit, M., et al., *Dynamic suspension culture for scalable expansion of undifferentiated human pluripotent stem cells.* Nat Protoc, 2011. **6**(5): p. 572-9.

51. Storm, M.P., et al., *Three-dimensional culture systems for the expansion of pluripotent embryonic stem cells.* Biotechnol Bioeng, 2010. **107**(4): p. 683-95.

52. Serra, M., et al., *Microencapsulation technology: a powerful tool for integrating expansion and cryopreservation of human embryonic stem cells.* PLoS One, 2011. **6**(8): p. e23212.

53. Braccini, A., et al., *Three-dimensional perfusion culture of human bone marrow cells and generation of osteoinductive grafts.* Stem Cells, 2005. **23**(8): p. 1066-72.

54. Papadimitropoulos, A., et al., *Expansion of human mesenchymal stromal cells from fresh bone marrow in a 3D scaffold-based system under direct perfusion.* PLoS One, 2014. **9**(7): p. e102359.

55. Lei, Y. and D.V. Schaffer, *A fully defined and scalable 3D culture system for human pluripotent stem cell expansion and differentiation.* Proc Natl Acad Sci U S A, 2013. **110**(52): p. E5039-48.

56. Chen, X.D., et al., *Extracellular matrix made by bone marrow cells facilitates expansion of marrow-derived mesenchymal progenitor cells and prevents their differentiation into osteoblasts.* J Bone Miner Res, **2007**. **22**(12): p. 1943-56.

Chapter 5

CONCLUSIONS AND FUTURE WORK

5.1 Conclusions

A novel, facile and economical method of fabricating 3D macroscopic (>1 mm in all three directions) macroporous all carbon scaffolds using MWCNTs has been reported. The scaffolds prepared by radical initiated thermal crosslinking and annealing of MWCNTs possess macroscale interconnected pores, robust structural integrity, stability, and conductivity. Varying the amount of radical initiator can control the porosity of the three-dimensional structure. This method allows fabrication of 3-D scaffolds using other carbon nanomaterials such as single-walled carbon nanotubes, fullerenes, and graphene indicating that it could be used as a versatile method for 3-D assembly of carbon nanostructures with pi bond networks. Additionally, the fabrication process of the scaffolds is rapid, economical, and scalable, and can be adapted to fabricate scaffolds with various geometries (e.g. cylinders, disks) thereby opening avenues for structure function studies towards the development of macroscopic all-carbon devices. The 3D SWCNT and MWCNT scaffolds containing nano-, micro- and macro-scaled interconnected pores show good cell viability, attachment, proliferation and cell infiltration of MC3T3 pre-osteoblasts and human ADSCs. Differences in cell morphology were observed; MC3T3 cells on MWCNT scaffolds were elongated whereas

on SWCNT scaffolds were rounded suggesting that scaffold nanotopography may be modulated to control cell morphology. ADSCs after long-term expansion on MWCNT and SWCNT scaffolds retain their stem cell phenotype (express MSC surface antigens), can be harvested from 3D MWCNT and SWCNT scaffolds, and show robust multi-lineage differentiation into osteoblasts, adipocytes and chondrocytes. These results taken together suggest that 3D macroporous all-carbon scaffolds fabricated using SWCNT and MWCNTs are cytocompatible and opens avenues for further *in vivo* investigation of these structures as multifunctional scaffolds for tissue engineering and regenerative medicine applications. These results also suggest that 3D macroporous MWCNT and SWCNT scaffolds can be used as synthetic 3D matrices for *ex-vivo* expansion and maintenance of MSCs for clinical therapeutic applications.

5.2 Future work

(1) The assessment of *in vivo* biocompatibility using small and large animals is critical to demonstrate the safety and efficacy of every new biomaterial before eventual use for humans in clinic. Therefore, the next logical step would be to assess the biocompatibility of 3D MWCNT and SWCNT scaffolds first in small animals (mice and rats) and subsequently in a larger animal model of interest. Studies should characterize the inflammatory responses, biodistribution and i*n vivo* enzymatic biodegradation of CNTs by macrophages and natural killer cells.

Studies focusing on the hematological toxicity of 3D CNT scaffolds should also be performed.

(2) CNTs have been used as contrast agents for several bioimaging modalities such as magnetic resonance imaging (MRI), Raman spectroscopy, photoacoustic and thermoacoustic imaging. To further develop 3D CNT scaffolds for the next generation theragnostic tissue engineering applications, studies should focus on non-invasive *in vivo* longitudinal monitoring of tissue healing using 3D CNT scaffolds as delivery vehicles/carriers for cells and therapeutics such as drugs and proteins by multimodality imaging such as MRI-photoacoustic-Raman imaging.

(3) In addition to matrix stiffness, nanotopography and cellular morphology play an important role in augmenting cellular behavior. Our results in chapter 3 show that the morphology of MC3T3 cells can be governed by the surface roughness of CNT scaffolds wherein MC3T3 cells were elongated on scaffolds with high surface roughness (MWCNTs) and rounded on scaffolds with low surface roughness (SWCNTs). Future studies should focus on fabricating 3D CNT scaffolds with varying surface roughness using CNTs of various diameters and investigate in detail the effects nanotopography of 3D CNT scaffolds on the genotype and phenotype of cells.

(4) CNTs have been used as nanofibers mats for applications in neural tissue engineering wherein electrical stimulus has been used as a biophysical cue to

guide axonal regeneration and improve neuronal activity (vesicle transport and fusion) by electrical shortening. Since 3D CNTs scaffolds are electrically conductive, they may be used for the development of three-dimensional neuronal interfaces instead of 2D neural patches, which can be controlled by an external electrical stimulus. Once can envision the development of CNT scaffolds as 3D electrodes for deep brain stimulation for diseases such as Parkinson's and Alzheimer's.

(5) Our results show that 3D MWCNT and SWCNT scaffolds can be used as synthetic matrices for *ex vivo* expansion and maintenance of human adipose derived mesenchymal stem cells. Future studies should focus on the use of MSCs expanded on 3D CNT scaffolds for *in vivo* tissue regeneration applications.

(6) Due to cell proliferation on MWCNT and SWCNT scaffolds, ECM will be deposited on these nanomaterials. These ECM coated MWCNTs and SWCNTs can be harvested after de-cellularization and the ECM proteins may be isolated. One may envision the use of these ECM coated nanomaterials as novel materials for ECM protein isolation. The ECM coated CNTs maybe less cytotoxic to cells compared to pristine CNTs, therefore, in vitro and in vivo cyto- and biocompatibility studies should be performed to assess their toxicity.